論文 / 著書情報
Article / Book Information

題目(和文)	
Title(English)	Thermal Transport Properties of Silicon Nanocrystals and Polystyrene Nanocomposite Thin Film
著者(和文)	ジャンサ フィルマン バグジャ
Author(English)	Firman Bagja Juangsa
出典(和文)	学位:博士(工学), 学位授与機関:東京工業大学, 報告番号:甲第11304号, 授与年月日:2019年9月20日, 学位の種別:課程博士, 審査員:野﨑 智洋,森川 淳子,平田 敦,末包 哲也,大河 誠司
Citation(English)	Degree:Doctor (Engineering), Conferring organization: Tokyo Institute of Technology, Report number:甲第11304号, Conferred date:2019/9/20, Degree Type:Course doctor, Examiner:,,,,
学位種別(和文)	博士論文
Type(English)	Doctoral Thesis

Thermal Transport Properties of Silicon Nanocrystals and Polystyrene Nanocomposite Thin Film

A DISSERTATION
SUBMITTED TO THE FACULTY OF SCHOOL OF ENGINEERING,
GRADUATE MAJOR OF ENERGY SCIENCE AND ENGINEERING
OF TOKYO INSTITUTE OF TECHNOLOGY
BY

Firman Bagja Juangsa

IN PARTIAL FULFILLMENT OF THE REQUIREMENTS
FOR THE DEGREE OF
DOCTOR OF ENGINEERING

Supervisor:
Professor Tomohiro Nozaki

June 2019

Acknowledgment

First and Foremost praise is to Allah SWT, the Almighty, the greatest of all, on whom ultimately we depend for sustenance and guidance. I would like to thank Almighty Allah for giving me the opportunity, determination, and strength to do my research. There are many people whom I have to acknowledge for their support, help, and encouragement during the preparation of this thesis. So, I will attempt to give them their due here, and I sincerely apologize for any omissions.

First, I would like to record my gratitude to my supervisor Prof. Tomohiro Nozaki, for his supervision, advice, and guidance from the early stage of this research. Also, I would like to thank Prof. Junko Morikawa for her support and permission for me using the equipment in Morikawa lab, and Ryu for his kind support and assistance.

My sincere gratitude goes to the Indonesia Endowment Fund for Education (LPDP) for their full supports during my master and doctoral study.

My fellow Nozaki lab members have proved to be invaluable during my last 5 years in Japan. Special thanks for their supports and plenty of discussion regarding research and daily life in Japan.

I greatly appreciate my thesis examination committee: Prof. Tomohiro Nozaki, Prof. Junko Morikawa, Prof. Atsushi Hirata, Prof. Seiji Okawa and Prof. Tetsuya Suekane for reading this long document.

I wish to express my thanks and gratitude to my parents, the ones who can never ever be thanked enough, for the overwhelming pray, love, and care they bestow upon me. My little family, especially my beloved wife Armelia, with her understanding, support, commitment and looking after my children during my study all stand behind my success, and two little princess Ayumi and Kiyomi with their innocent smiles have made any task bearable.

June 2019

Firman Bagja Juangsa

Tokyo Tech

Table of Contents

List of Figures

Chapter 1: Introduction

1.1. Overview

Silicon is the second most abundant element in the earth's crust, providing enormous potential to be utilized as a base material for various application in human life. Its nontoxic and semiconductor properties have made silicon as the main material for most of the electronic devices since it is produced in pure form at 19th centuries [1]. Silicon rarely exists in the pure state, mostly as a form of silicon dioxide or silicates. In the periodic table of elements, silicon has an atomic number of 14 classified as the IVA group along the bold line that separates metals from non-metals (Figure 1-1). It has an electron configuration of 2-8-4 and four valence electrons, which can be shared to form chemical bonds.

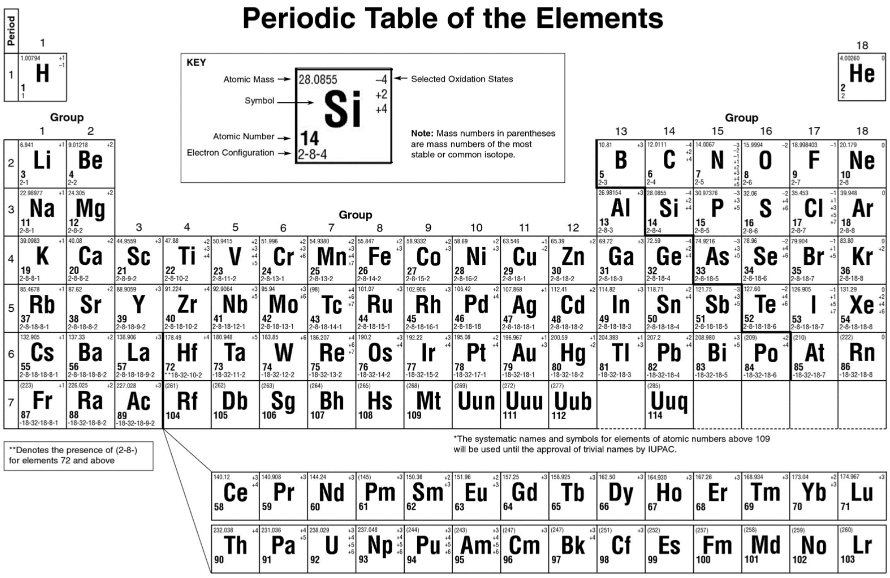

Figure 1-1 Periodic table of elements showing properties of silicon (Si) [2]

The present name of silicon was introduced by Thomas Thomson, who believed that silicon was a nonmetal similar to boron and carbon [3]. It is mostly used as the raw material for glass, cement, ceramics and synthetic polymers as silicones. Silicon plays an essential role in modern technology as a semiconductor material for electronics devices such as microelectronic, photovoltaic, and MEMS technology [4]. Silicon has an indirect band gap of 1.12 eV at room temperature and high photosensitivity, which allows the light energy conversion into electrical energy. Silicon-based solar cell/photovoltaic showed promising development with gradually efficiency improvement up to about 25% in 50 years of development, and currently being the commercially available solar cell model [5].

The development of the electronic device has been focusing on miniaturization in order to significantly reduce the size of the device. On the other hand, modern technology urges a significant improvement in device performance and efficiency. These demands of size reduction and performance improvement give a challenge for technology development of silicon as the main semiconductor material. The further research and development of silicon are by reducing its size down to the nanoscale, which brings new properties for the various promising application. Silicon nanocrystals (SiNCs) or nano-size silicon crystals is fully compatible with the well-established silicon technology so that it gained much more research interest than other kinds of nanoparticles. Knowing the chemical and physical properties of SiNCs, including its synthesize process and application, would be a great impact on science and technology development [4].

1.2. Silicon Nanocrystals and Synthesis Methods

Nano size materials have been studied due to their unique properties that are different from their bulk counterparts. Numerous studies on optical, electrical, and thermal properties of nanomaterials have been reported with an interesting result, yet challenging fabrication method of functional macroscale device. In particular, nano size silicon particle (silicon nanoparticles; SiNPs) have attracted much attention of studies and analysis due to its non-toxic feature and abundance in the earth crust.

Nano size silicon was firstly reported by Cullis and Canham, where photoluminescent (PL) was observed in the visible range at room temperature from porous crystalline silicon [6]. Since then, the interest in nanostructured silicon proliferated with various device application for its optical properties, such as solar cells and light emitting devices [7], [8]. Bulk silicon is an indirect bandgap semiconductor with a low probability of electron-hole pair recombination, resulting in weak photoluminescence. However, strong photoluminescence was observed from nano-size silicon, indicating a high probability of electron-hole pair recombination and direct or quasi-direct bandgap behavior. The significant difference of optical properties between bulk and nano-size silicon has been well explained as the result of quantum confinement effect at nano-size material, which has photoluminescence wavelength inversely dependent on particle size [6], [9], [10], as shown in Figure 1-2.

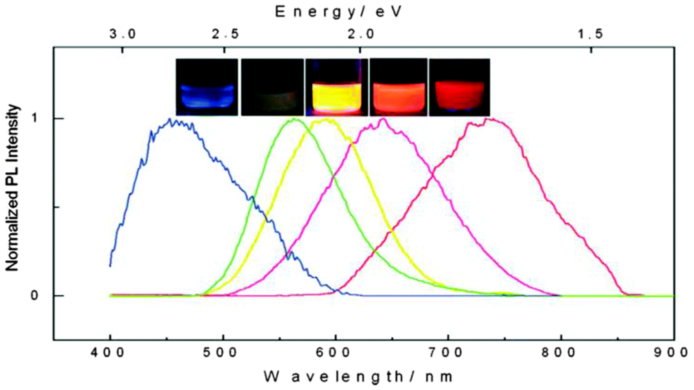

Figure 1-2 Representation of SiNPs size effect on photoluminescence wavelength [10]

SiNPs is wide class materials with a wide range of definition, depend on the dominant properties and application. The term “nanoparticle” is generally used in material science, which refers to a particle with a size smaller than 100 nm [11]. However, SiNPs with a particle size smaller than 10 nm are commonly analyzed for size-dependent properties. With size below 10 nm, containing 2–20,000 atoms per particle, SiNPs has a significant quantum dot effect that appears in photoluminescent and band gap change, as well as thermal properties. SiNCs has been widely studied and reported for its' size-dependent optical, electronic, and thermal properties [4], [12]–[15]. SiNPs, particularly crystalline silicon (silicon nanocrystals; SiNCs) has been widely studied and reported mostly for their size-dependent optical and electronic properties [4], [12], [13], [16]. During the last decades, a number of studies have also been reported on size dependence of thermal transport properties in SiNCs [15], [17]. Controllable thermal transport property of SiNCs present the promising application in various devices, such as thermoelectric and micro-nano thermal management [18]–[20]. Therefore, it is essential to understand the intrinsic nature of thermal transport in SiNCs to provide optimum performance of device application.

There are numerous ways/processes to produce SiNCs, which can be categorized based on the principle process. One of comprehensive and simple categorization was reported by Mangolini, where SiNCs synthesis process is divided into three big groups: porous silicon, direct nucleation in a thin film, and free-standing nucleation. Porous silicon gained much attention as nanostructured silicon when photoluminescence was observed in the visible range [6], [21]–[23]. Porous silicon was produced by electrochemical etching of silicon wafers, so that, it forms nano size crystallites. Porous silicon has limitations of uncontrollable crystallites size during the chemical etching process, and also the crystallites are not isolated from each other. Furthermore, the electrochemical etching process is not compatible with large scale production.

SiNCs also can be synthesized by direct nucleation in a thin film using a two-step process of the deposition of nonstoichiometric silicon-containing films, such as oxide, nitride or carbide, and then thermal annealing to induce the nucleation of silicon crystals [24]–[27]. Compared to porous silicon, direct nucleation in the thin film offers several advantages such as controllable crystal size and compatibility with semiconductor technology. However, since the structure of the silicon-containing film, it is impossible to control the crystal size and particle density independently. This is an important feature for the high-efficiency device.

The last method to synthesize SiNCs is free standing nucleation. Among many proposed methods of free-standing SiNCs nucleation, researchers have been trying to develop a process that synthesizes particles with desired shape and size, with narrow size variation, and high production rate. Furthermore, with independent controllability of particle size and density within the application device, free-standing SiNCs is the most suitable synthesize process for large scale device manufacture/production.

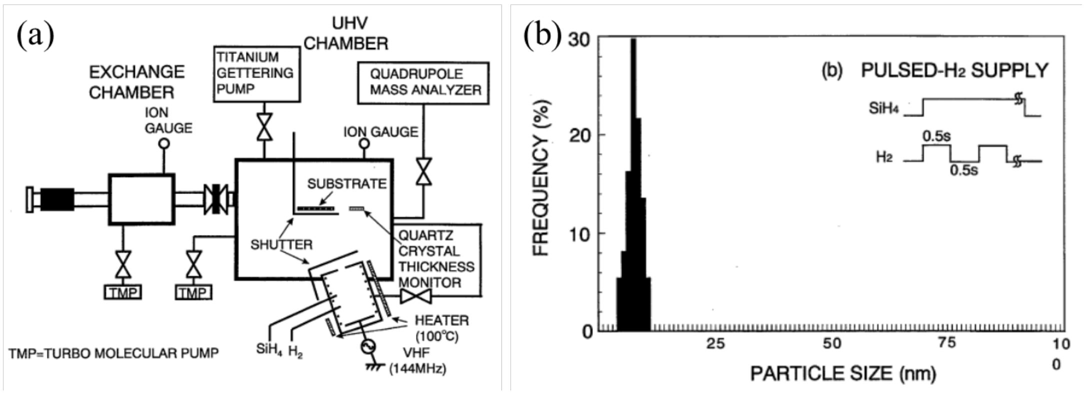

Figure 1-3 (a) Pulsed gas plasma apparatus schematic diagram, (b) Size distribution of SiNCs produced by pulsed H_2 with $SiCl_4$ plasma

Freestanding SiNCs can be produced through various kinds of process, such as thermal decomposition [28], [29], laser-induced pyrolysis[30], solid silicon ablation[31], and plasma synthesis [32]–[35]. Narrow particle size distribution yet preventing the particle coagulation to preserve the nano size has been the target of development on each kind of process. Moreover, high production yield, simple steps, and controllable parameters are also inevitable factors in SiNCs synthesis development. Among all of the process, the gas phases process of plasma-based synthesis method has been well proven to be a method that fulfills all the required parameters.

Nucleation in plasma synthesis is initiated by small radicals, and it occurs rapidly. When low-pressure gas is supplied by electric fields, the electron will be accelerated and then ionized the surrounding that leads to disassociation of silicon precursor. It is then followed by the crystal growth phase from the chemical clustering of precursor radicals. When the particle density has reached the ion density, the agglomeration slows down, and the growth rate decreases. This is an important phenomenon as it does not happen in another process. The further interaction of plasma changed species, and other radicals increase the temperature, which improves the crystallinity of SiNCs through the annealing process.

In terms of production rate, microwave plasma, which is also referred as thermal plasma due to high gas temperature, has been applied to pilot scale of SiNCs production with a high production rate of 0.1−10 g/h [36]. SiNCs with a mean particle size of 13 nm were produced with 200 W of plasma power. Specific energy required for SiNCs production using microwave can be calculated to 20−2000 Wh/g. Compared with thermal plasma, studies on nonthermal plasma are mostly in laboratory scale with low production rate [16], [37]. However, in the matter of specific energy for SiNCs, nonthermal plasma is comparable to thermal plasma, with the specific energy required for SiNCs of approximately 600 Wh/g. Therefore, the high production rate of SiNCs can be achieved by nonthermal plasma while maintaining the minimum specific energy requirement in the plasma reactor.

Controllability of plasma enhanced processes has been reported widely. Ifuku et al. [38] have reported the pulsed gas plasma method to synthesize the SiNCs, where silane was used as the precursor. With the pulsed supply of H_2, the nucleation time length can be adjusted, and the desired narrowed particle size can be achieved, as shown in [39].

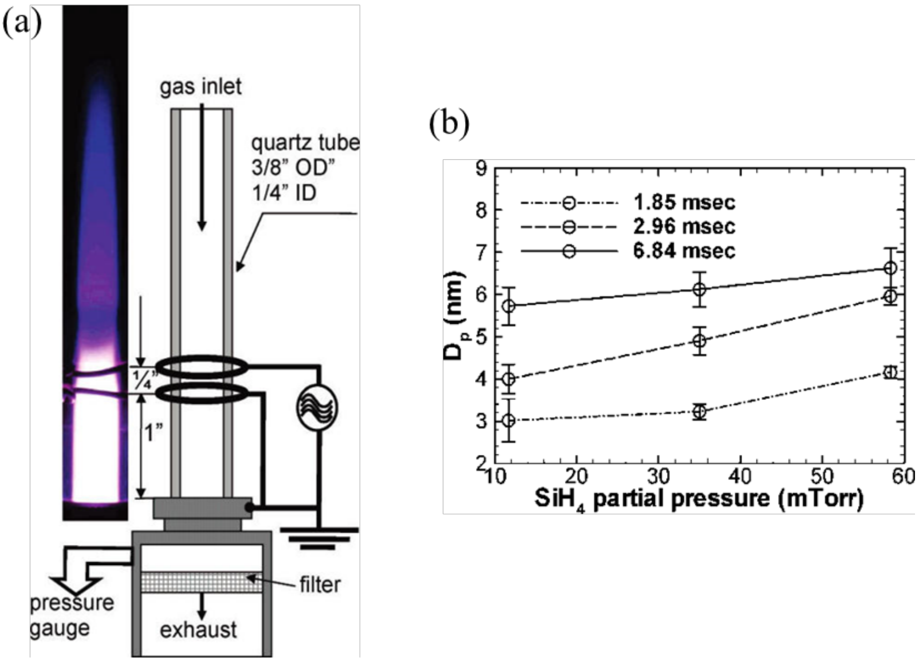

Figure 1-4 (a) Nonthermal plasma (silane) apparatus schematic diagram, (b) Effect of silane partial pressure and residence time in the average particles size

Another group of Mangolini et al. reported the SiNCs synthesis with nonthermal plasma deposition. Silane was used as a precursor, and mixture gas of silane and argon were supplied through the reactor tube, as shown in Figure 1-4(a). RF power was provided to induce plasma that triggered the disassociation of silane and nucleation of SiNCs that is collected in the filter at downstream. Particle size was controlled by adjusting the partial pressure of silane and also residence time within the plasma reactor, as shown in Figure 1-4 (b).

The comparison of various synthesis method of SiNCs is presented in Figure 1-5 that shows X-ray diffraction (XRD) patterns of SiNCs produced by different methods of synthesis based on gas phase plasma approach. X-ray diffraction pattern represents the crystal structure of SiNCs, indicating that all methods shown in Figure 1-5 have a similar pattern of the crystal structure. This may indicate that, at single nano order of SiNCs, crystal structure would be formed by the same mechanism regardless of the processing condition. In addition, the $SiCl_4$ precursor can be used as an alternative precursor to SiH_4, confirmed by the similar crystal structure, as also have been reported previously [40].

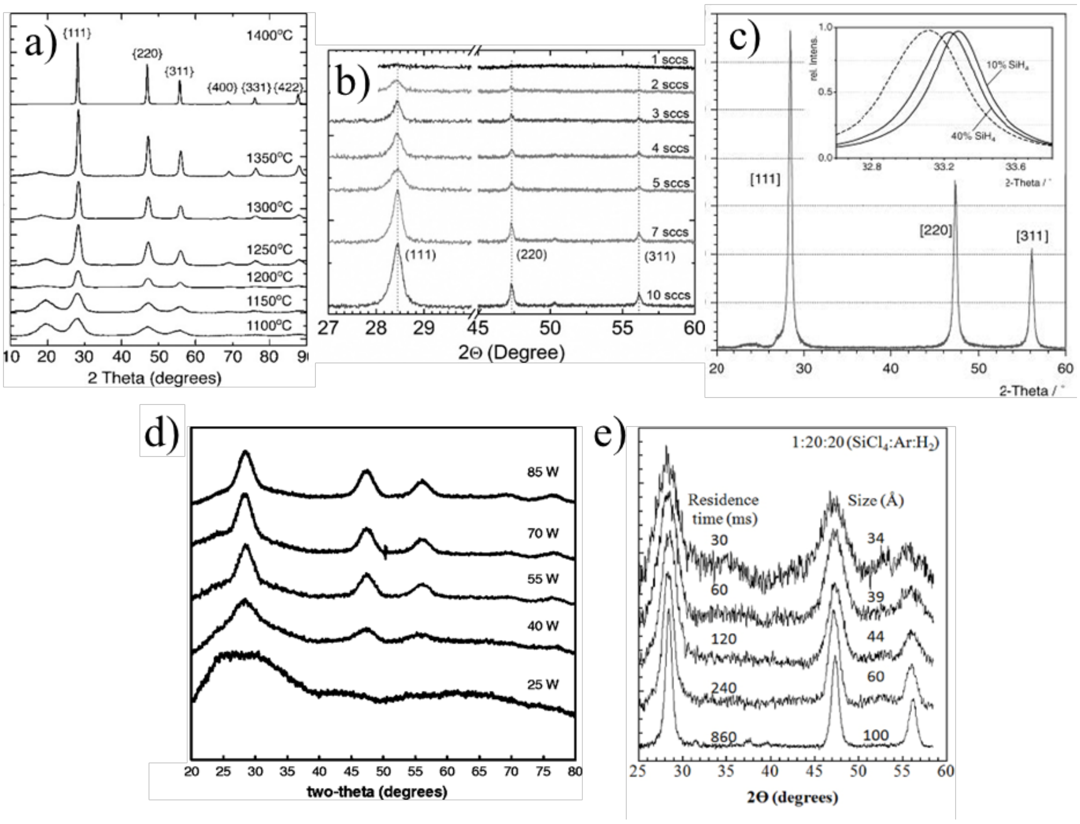

Figure 1-5. X-ray diffraction (XRD) patterns of SiNCs produced by various methods: (a) Solid phase nucleation of SiNC embedded in oxide matrix [41], (b) Thermal plasma (expanding arc plasma) with SiH_4 precursor [42], (c) Thermal plasma (microwave) with SiH_4 precursor [43], (d) Nonthermal plasma CVD (13.56 MHz) with SiH_4 precursor [44], and (e) Nonthermal plasma CVD (70 MHz) with $SiCl_4$ precursor [12].

Silane has been well known as the primary precursor of SiNCs due to the ability to produce SiNCs [14], [39], [45]. However, its toxic property and high cost have led to development for another kind of precursor. Silicon tetrachloride ($SiCl_4$) has been utilized as an alternative precursor due to it is non-toxic and significantly cheaper [32], [46]. Furthermore, chlorine content requires further post-processing of SiNCs surface termination, allowing a variety of surface termination, including controlled oxidation to be analyzed.

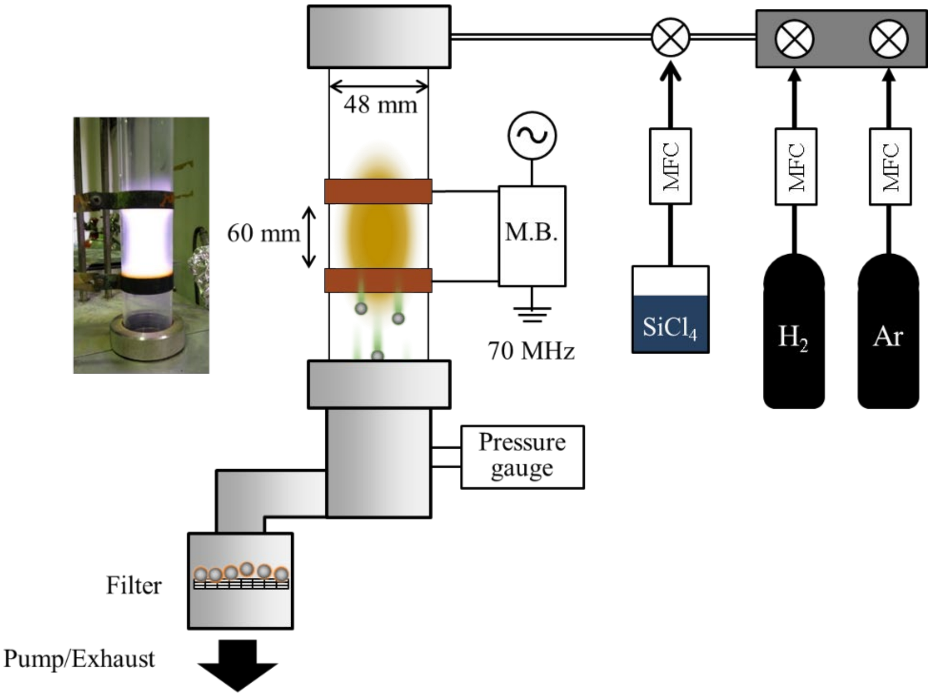

Figure 1-6. Schematic of a nonthermal plasma reactor for SiNPs synthesis with plasma glow during the SiNPs synthesis.

This thesis is working on nonthermal Plasma Enhanced Chemical Vapor Deposition (PECVD), which employs Very High Frequency (VHF) power to generate plasma. SiNCs with size less than 10 nm were produced with narrow size distribution [35], [47]. Furthermore, this method has been proven to be able to control particle size, particle crystallinity, and also produce the amorphous silicon particle [35], [46], [48].

The synthesis apparatus is presented briefly in Figure 1-6. Mixture gas of precursor $SiCl_4$, H_2, and Ar flow through the quartz tube reactor, where SiNCs nucleation and crystal growth process is carried out by employing a very high frequency (70MHz) nonthermal plasma. Decomposition of $SiCl_4$ is carried out in the plasma reactor, started with the reduction by H_2. Atomic hydrogen radical, generated by plasma, promote the further decomposition of $SiCl_4$ and reported to be the key species for low-temperature $SiCl_4$ decomposition.

The decomposition process is followed by nucleation and particle growth process, which is induced by plasma. Nanoparticles are most likely negatively charged in nonthermal plasma; Coulomb repulsion force enables individual growth of nanoparticles without significant agglomeration. Moreover, charge recombination occurring on the nanoparticle surface provide energy necessarily for crystallization [13], [49].

1.3. Thermal Transport Investigation on SiNCs

As mentioned above, understanding the intrinsic nature of thermal transport in SiNCs is important. However, direct thermal transport investigation on the single order nano-size particle is technically challenging and complicated, due to the limitation of measurement apparatus and precision. On the other hand, silicon-based nanostructured materials have been extensively studied and developed to utilize the novel properties of SiNCs. Also, the thermal transport investigation on nanostructured materials provides information regarding the intrinsic mechanism of thermal transport in SiNCs.

A number of studies have been reported regarding the thermal transport investigation in silicon nanostructure, which can be produced by various methods. Most of the nanostructures made from SiNCs are formed by a sintering process, a process which combines high mechanical pressure and high temperature to obtain particles compacted by enhanced diffusion among the particles [13], [15], [18]. Spark plasma sintering (SPS) is the most common method to prepare the nanostructured sample, utilizing large current densities to induce rapid joule heating process (up to 1000ºC) while simultaneously applying high pressure (above 100 MPa) to the sample [15], [18]. Less process time is vital for the sintering process to prevent undesired grain coarsening, which may reduce the maximum density. Wang et al. reported the thermal conductivity measurement of nanostructured SiNCs produced by SPS, showing a significant decrease in the thermal conductivity with a smaller particles size of 64–550 nm [15]. The particle size is determined by process time at high temperature, which also controlled the densification process of nanostructure [15]. Although many studies reported less time required for SPS compared with conventional hot pressing sintering, the high-temperature process is unavoidable in the sintering process, which is the main factor of grain growth [15], [18]. The non-uniform heating process causes broad particle size distribution and porosity formation among the SiNCs, which are detrimental to intrinsic property analysis. In addition, the high-temperature condition of SPS may induce undesired crystallization of amorphous silicon, changing the degree of crystallinity during the sintering process.

Group of Wiggers et al. reported the SPS method (1100°C) utilization to produce SiNCs nanostructure for application in the thermoelectric device [50]. SiNCs were synthesized by a gas-phase based process using microwave plasma power with particles mean diameter below 10 nm [50], [51]. Microwave plasma has been reported successfully utilized to synthesize sufficiently small SiNCs to show the confinement effect with a relatively high SiNCs production rate of 0.1−10 g/h [36], [51]. Microwave plasma increases the gas temperature along the reactor, where the decomposition followed by nucleation and crystal growth [52]. Provided high-temperature gas, which is nearly equal to electron temperature, allowing reaction near the thermal equilibrium condition, the process is known as thermal plasma. Compared with the classical method of thermal decomposition, plasma-induced decomposition has a lower possibility of particle agglomeration, due to highly charged particles that cause inter-particle Coulomb force, preventing them to agglomerate [53].

Plasma sintering method was also employed by Miura et al. to produce nanostructures from phosphorus-doped SiNCs with oxide core-shell [18]. Plasma-enhanced chemical vapor deposition (PECVD) with radio frequency (RF) plasma was utilized to synthesize a single nano order of SiNCs particle size with narrow size distribution. Nanostructured material consists of nanograins of crystalline silicon and amorphous silicon oxide, was employed for the thermoelectric device. Thermal conductivity measurement showed a promising reduction to as low as 5% compared with bulk Si, which is attributed majorly to the phonon scattering mechanism at the grain boundaries of SiNCs. Lower thermal conductivity, coupled with the electric conductivity enhancement by a controlled oxide layer, which provides a promising performance for thermoelectric device application.

However, SiNCs size and size distribution were not preserved during the nanostructure fabrication, which is caused by the high-temperature process of sintering, as shown by the TEM image in Figure 1-7. SiNCs that is originally synthesized with a single nano order of size had a crystal growth up to 30 nm, and the morphology change of core-shell structure was observed shown by agglomerated amorphous oxide region. Further improvement of SiNCs-based nanostructured can be achieved by preserving the single nano order particle size and narrow size distribution.

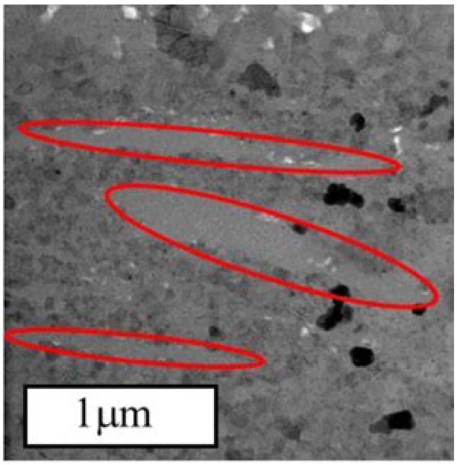

Figure 1-7 TEM image of nanostructure consists of SiNCs region and amorphous Si oxide region (part circled with red). Modified with permission from [18] American Chemical Society 2015.

Thermal conductivity significant reduction in nanostructure with *connected SiNCs* for the thermoelectric application was reported by Nakamura et al. [54]. The SiNCs formation was carried out by molecular beam epitaxy (MBE) produce single nano order particles of 3.1 nm with narrow size distribution. The combination of SiNCs formation and slight oxidation formed SiNCs with very thin oxide layers, which greatly influence the thermal conductivity reduction below the amorphous limit of silicon [54]. Ultra-high vacuum (UHV) process and controlled nanoscale process of MBE ensure the crystalline silicon orientation and nanoscale morphology of core-shell SiNCs.

Another approach of silicon nanostructure is porous silicon. Kihara et al. reported the thermal conductivity measurement result of SiNCs formed in porous silicon [17]. A layer of SiNCs was prepared by electrochemical anodization of a (100) crystalline silicon wafer. The anodization was carried out at constant electrical current density with hydro fluoride (HF) and ethanol as the electrolyte, forming pores in the silicon wafer. Although the measurement result showed a significant decrease of thermal conductivity, which is attributed to size dependence thermal transport of SiNCs, it is difficult to determine the intrinsic property of SiNCs due to the uncontrollable SiNCs' size and the existence of porosity. SiNCs size approximation of 3 nm was determined by photoluminescence observation, size it is technically challenging to measure the particles size in porous silicon qualitatively.

1.4. Thermal Transport Analysis on SiNCs-based Nanocomposite

This thesis is focusing on thermal transport properties investigation on SiNCs by utilizing the nanocomposite regime, which consists of SiNCs and polymer. SiNCs were synthesized by very high frequency (VHF) of 70 MHz plasma-enhanced chemical vapor deposition. Sufficiently small particle size below 10 nm with narrow size distribution have been successfully produced and employed for many device applications, especially solar cell [55], [56]. The SiNCs synthesis process is carried out at nonequilibrium condition where the electron temperature (20,000–50,000K) is significantly higher than gas temperature, which remains nearly room temperature, is commonly referred as nonthermal plasma [16]. A nonthermal plasma is one of the gas-phase processes of SiNCs synthesis, which has the advantage of the ability to produce SiNCs with the desired particle size and narrow size distribution [13], [37].

The produced SiNCs were then dispersed within the polymer matrix through solution processing to produce a heterogeneous nanocomposite. Wide applications of nanocomposite have been reported on thermoelectric [57], thermal management system [58], and solar cell [7], [56] due to the high interface to volume ratio. This thesis is working on thermal transport analysis of SiNCs based nanocomposite polymeric thin films. The nanocomposite of SiNCs and polystyrene (PS) were fabricated through solution processing in a low-temperature environment, preserving the original SiNCs size and narrow size distribution. Preserving the nano size during the process is essential in order to observe the intrinsic properties of SiNCs and its' behavior in the bulk nanostructure.

1.5. Scope of this Thesis

This thesis concentrates on thermal transport analysis of SiNCs/polystyrene nanocomposite structure. Thermal transport property is represented by thermal conductivity, which is determined through multiple measurements of mass density, specific heat, and thermal diffusivity. Most of this thesis is focused on thermal transport mechanism in nanocomposite structure, including the interfacial interaction between SiNCs and polystyrene through experimental measurement and comparison with theoretical thermal conductivity calculations.

Chapter 1 provides an introduction to SiNCs, including synthesis methods and their thermal transport properties and mechanism. Thermal transport analysis on SiNCs is also described, as well as the motivation of analyzing the thermal transport in nanocomposite materials.

Chapter 2 describes the nanocomposite fabrication process and thermal transport properties measurement methods. Thermal properties measurements were validated by measurement of bulk polystyrene as a well-known polymer. The result shows a significant effect of SiNCs in determining thermal transport in nanocomposite with a decreasing trend, despite the conductive properties of SiNCs compared with polystyrene. Extensive material characterizations were investigated to analyze the effect of SiNCs in thermal conductivity of nanocomposite. This chapter is published in Journal of Physics D: Applied Physics by Firman Bagja Juangsa, Yoshiki Muroya, Meguya Ryu, Junko Morikawa, and Tomohiro Nozaki (*Journal of Physics D: Applied Physics*, 49(36), 365303 (2016)).

Chapter 3 describes a further investigation of nanocomposite thermal transport by comparing crystalline and amorphous SiNPs. The result indicates a significant effect of thermal transport mechanism at the material interface. The experimental results are compared with thermal conductivity models for nanocomposite to help determine the contribution of thermal boundary resistance at the material interface. The thermal transport mechanism at the material interface was further investigated by thermal annealing treatment, which showed thermal transport enhancement due to molecular interaction at material boundaries. Portion of this chapter is published in Applied Physics Letters by Firman Bagja Juangsa, Yoshiki Muroya, Meguya Ryu, Junko Morikawa, and Tomohiro Nozaki, (*Applied Physics Letters*, 110(25), 253105 (2017)), and Journal of Physics D: Applied Physics by Firman Bagja Juangsa, Meguya Ryu, Junko Morikawa, and Tomohiro Nozaki, (*J Phys D Appl Phys*. 51(50):505301 (2018)).

Chapter 4 highlights the interfacial region developed at the material interface and its effect in determining the thermal transport of nanocomposite. Further analysis of thermal transport of SiNCs/PS nanocomposites was performed by employing SiNCs with significantly different diameter of 6nm and 60nm. The experimental results are also compared with the thermal conductivity model to investigate the effect of material interface on the interfacial region of polystyrene, which has a highly morphology dependent property. The comparison shows the thermal conductivity model can successfully consider the effect of material interfaces, yet the deviation remains from the experimental result. The thermal conductivity model is improved by modifying the thermal conductivity of matrix due to the confinement effect at the interfacial region, resulting in the well-matched thermal conductivity curves with the measurement result. This chapter is to be submitted as a separated manuscript to an international journal.

Chapter 5 provides conclusions and recommendations for future work.

1.6. References

[1] M. G. Voronkov, “Origin of the silicon era,” *Glas. Phys. Chem.*, vol. 35, no. 3, pp. 231–236, Jun. 2009.

[2] “Reference Tables for Physical Setting/CHEMISTRY,” *The University of The State of New York*, 2011. [Online]. Available: https://www.kentchemistry.com/newRT.pdf. [Accessed: 15-Jan-2019].

[3] T. Thomson, *A system of chemistry: in four volumes*, vol. 4. Abraham Small, 1818.

[4] L. Pavesi and R. Turan, *Silicon Nanocrystals*. Weinheim, Germany: Wiley-VCH Verlag GmbH & Co. KGaA, 2010.

[5] M. A. Green, “Silicon photovoltaic modules: a brief history of the first 50 years,” *Prog. Photovoltaics Res. Appl.*, vol. 13, no. 5, pp. 447–455, Aug. 2005.

[6] A. G. Cullis and L. T. Canham, “Visible light emission due to quantum size effects in highly porous crystalline silicon,” *Nature*, vol. 353, no. 6342, pp. 335–338, Sep. 1991.

[7] Y. Ding, S. Zhou, F. B. Juangsa, M. Sugaya, Y. Asano, X. Zhang, Y. Zhao, and T. Nozaki, “Optical, electrical, and photovoltaic properties of silicon nanoparticles with different crystallinities,” *Appl. Phys. Lett.*, vol. 107, no. 23, p. 233108, Dec. 2015.

[8] Z. Deng, X. D. Pi, J. J. Zhao, and D. Yang, “Photoluminescence from Silicon Nanocrystals in Encapsulating Materials,” *J. Mater. Sci. Technol.*, vol. 29, no. 3, pp. 221–224, 2013.

[9] D. S. English, L. E. Pell, Z. Yu, P. F. Barbara, and B. A. Korgel, “Size Tunable Visible Luminescence from Individual Organic Monolayer Stabilized Silicon Nanocrystal Quantum Dots,” *Nano Lett.*, vol. 2, no. 7, pp. 681–685, 2002.

[10] A. Gupta, F. Erogbogbo, M. T. Swihart, and H. Wiggers, “Photoluminescence behavior of silicon nanocrystals: Role of surface chemistry and size,” in *Materials Research Society Symposium Proceedings*, 2008, vol. 1145, pp. 131–136.

[11] F. E. Kruis, H. Fissan, and A. Peled, “Synthesis of nanoparticles in the gas phase for electronic, optical and magnetic applications—a review,” *J. Aerosol Sci.*, vol. 29, no. 5–6, pp. 511–535, Jun. 1998.

[12] R. Gresback, T. Nozaki, and K. Okazaki, “Synthesis and oxidation of luminescent silicon nanocrystals from silicon tetrachloride by very high frequency nonthermal plasma.,” *Nanotechnology*, vol. 22, no. 30, p. 305605, Jul. 2011.

[13] L. Mangolini, “Synthesis, properties, and applications of silicon nanocrystals,” *J. Vac. Sci. Technol. B Microelectron. Nanom. Struct.*, vol. 31, no. 2, p. 020801, 2013.

[14] L. Mangolini, E. Thimsen, and U. Kortshagen, “High-yield plasma synthesis of luminescent silicon nanocrystals,” *Nano Lett.*, vol. 5, no. 4, pp. 655–659, 2005.

[15] Z. Wang, J. E. Alaniz, W. Jang, J. E. Garay, and C. Dames, “Thermal conductivity of nanocrystalline silicon: Importance of grain size and frequency-dependent mean free paths,” *Nano Lett.*, vol. 11, no. 6, pp. 2206–2213, Jun. 2011.

[16] L. Mangolini, E. Thimsen, and U. Kortshagen, “High-yield plasma synthesis of luminescent silicon nanocrystals,” *Nano Lett.*, vol. 5, no. 4, pp. 655–659, Apr. 2005.

[17] T. Kihara, T. Harada, and N. Koshida, “Precise thermal characterization of confined nanocrystalline silicon by 3ω method,” *Japanese J. Appl. Physics, Part 1 Regul. Pap. Short Notes Rev. Pap.*, vol. 44, no. 6 A, pp. 4084–4087, Jun. 2005.

[18] A. Miura, S. Zhou, T. Nozaki, and J. Shiomi, “Crystalline-Amorphous Silicon Nanocomposites with Reduced Thermal Conductivity for Bulk Thermoelectrics,” *ACS Appl. Mater. Interfaces*, vol. 7, no. 24, pp. 13484–13489, Jun. 2015.

[19] W. Yan, B. Phung, Z. Han, and K. Ostrikov, “Plasma polymer-coated on nanoparticles to improve dielectric and electrical insulation properties of nanocomposites,” *IEEE Trans. Dielectr. Electr. Insul.*, vol. 21, no. 2, pp. 548–555, Apr. 2014.

[20] T. Suzuki, Y. Ohishi, K. Kurosaki, H. Muta, and S. Yamanaka, “Thermal Conductivity of Size-Controlled Bulk Silicon Nanocrystals Using Self-Limiting Oxidation and HF Etching,” *Appl. Phys. Express*, vol. 5, no. 8, p. 081302, Jul. 2012.

[21] V. Lehmann and U. Gösele, “Porous silicon formation: A quantum wire effect,” *Appl. Phys. Lett.*, vol. 58, no. 8, p. 856, Feb. 1991.

[22] J. L. Heinrich, C. L. Curtis, G. M. Credo, M. J. Sailor, and K. L. Kavanagh, “Luminescent colloidal silicon suspensions from porous silicon.,” *Science*, vol. 255, no. 5040, pp. 66–8, Jan. 1992.

[23] L. T. Canham, “Silicon quantum wire array fabrication by electrochemical and chemical dissolution of wafers,” *Appl. Phys. Lett.*, vol. 57, no. 10, p. 1046, Sep. 1990.

[24] D. Song, E.-C. Cho, G. Conibeer, Y.-H. Cho, Y. Huang, S. Huang, C. Flynn, and M. A. Green, “Fabrication and characterization of Si nanocrystals in SiC matrix produced by magnetron cosputtering,” *J. Vac. Sci. Technol. B Microelectron. Nanom. Struct.*, vol. 25, no. 4, p. 1327, Jul. 2007.

[25] B. H. Kim, C. H. Cho, T. W. Kim, N. M. Park, G. Y. Sung, and S. J. Park, "Photoluminescence of silicon quantum dots in silicon nitride grown by NH3 and SiH4," *Appl. Phys. Lett.*, vol. 86, no. 9, pp. 1–3, Feb. 2005.

[26] N.-M. Park, T.-S. Kim, and S.-J. Park, "Band gap engineering of amorphous silicon quantum dots for light-emitting diodes," *Appl. Phys. Lett.*, vol. 78, no. 17, p. 2575, Apr. 2001.

[27] S. Hayashi, T. Nagareda, Y. Kanzawa, and K. Yamamoto, "Photoluminescence of Si-Rich SiO 2 Films: Si Clusters as Luminescent Centers," *Jpn. J. Appl. Phys.*, vol. 32, no. Part 1, No. 9A, pp. 3840–3845, Sep. 1993.

[28] M. K. Alam and R. C. Flagan, "Controlled Nucleation Aerosol Reactors: Production of Bulk Silicon," *Aerosol Sci. Technol.*, vol. 5, no. 2, pp. 237–248, Jan. 1986.

[29] A. A. Onischuk, V. P. Strunin, M. A. Ushakova, and V. N. Panfilov, "Studying of silane thermal decomposition mechanism," *Int. J. Chem. Kinet.*, vol. 30, no. 2, pp. 99–110, Jan. 1998.

[30] W. R. Cannon, S. C. Danforth, J. H. Flint, J. S. Haggerty, and R. A. Marra, "Sinterable Ceramic Powders from Laser-Driven Reactions: I, Process Description and Modeling," *J. Am. Ceram. Soc.*, vol. 65, no. 7, pp. 324–330, Jul. 1982.

[31] D. E. Powers, S. G. Hansen, M. E. Geusic, A. C. Puiu, J. B. Hopkins, T. G. Dietz, M. A. Duncan, P. R. R. Langridge-Smith, and R. E. Smalley, "Supersonic metal cluster beams: laser photoionization studies of copper cluster (Cu2)," *J. Phys. Chem.*, vol. 86, no. 14, pp. 2556–2560, Jul. 1982.

[32] Y. Ding, R. Gresback, K. Okazaki, and T. Nozaki, "Silicon nanocrystal fabrication by using non-thermal plasma and application to hybrid Si-nanocrystal / P3HT solar cells," vol. 305605, no. 2011, p. 305605, 2012.

[33] T. Nozaki, Y. Ding, and R. Gresback, "Plasma Synthesis of Silicon Nanocrystals: Application to Organic/Inorganic Photovoltaics through Solution Processing," *Mater. Sci. Forum*, vol. 783–786, pp. 2002–2004, May 2014.

[34] R. Gresback, Y. Murakami, Y. Ding, R. Yamada, K. Okazaki, and T. Nozaki, "Optical extinction spectra of silicon nanocrystals: Size dependence upon the lowest direct transition," *Langmuir*, vol. 29, no. 6, pp. 1802–1807, Feb. 2013.

[35] Y. Ding, R. Yamada, R. Gresback, S. Zhou, X. Pi, and T. Nozaki, “A parametric study of non-thermal plasma synthesis of silicon nanoparticles from a chlorinated precursor,” *J. Phys. D. Appl. Phys.*, vol. 47, no. 48, p. 485202, 2014.

[36] A. Gupta, M. T. M. T. Swihart, and H. Wiggers, “Luminescent colloidal dispersion of silicon quantum dots from microwave plasma synthesis: Exploring the photoluminescence behavior across the visible spectrum,” *Adv. Funct. Mater.*, vol. 19, no. 5, pp. 696–703, Mar. 2009.

[37] Y. Ding, R. Yamada, R. Gresback, S. Zhou, X. Pi, and T. Nozaki, “A parametric study of non-thermal plasma synthesis of silicon nanoparticles from a chlorinated precursor,” *J. Phys. D. Appl. Phys.*, vol. 47, no. 48, p. 485202, 2014.

[38] T. Ifuku, M. Otobe, A. Itoh, and S. Oda, “Fabrication of nanocrystalline silicon with small spread of particle size by pulsed gas plasma,” *Japanese J. Appl. Physics, Part 1 Regul. Pap. Short Notes Rev. Pap.*, vol. 36, no. 6 SUPPL. B, pp. 4031–4034, 1997.

[39] T. Ifuku, M. Otobe, A. Itoh, and S. Oda, “Fabrication of nanocrystalline silicon with small spread of particle size by pulsed gas plasma,” *Japanese J. Appl. Physics, Part 1 Regul. Pap. Short Notes Rev. Pap.*, vol. 36, no. 6 SUPPL. B, pp. 4031–4034, Jun. 1997.

[40] O. Yasar-Inceoglu, T. Lopez, E. Farshihagro, and L. Mangolini, “Silicon nanocrystal production through non-thermal plasma synthesis: a comparative study between silicon tetrachloride and silane precursors.,” *Nanotechnology*, vol. 23, no. 25, p. 255604, Jun. 2012.

[41] C. M. Hessel, D. Reid, M. G. Panthani, M. R. Rasch, B. W. Goodfellow, J. Wei, H. Fujii, V. Akhavan, and B. A. Korgel, “Synthesis of Ligand-Stabilized Silicon Nanocrystals with Size-Dependent Photoluminescence Spanning Visible to Near-Infrared Wavelengths,” *Chem. Mater.*, vol. 24, no. 2, pp. 393–401, Jan. 2012.

[42] I. Doğan, N. J. Kramer, R. H. J. Westermann, K. Dohnalová, A. H. M. Smets, M. A. Verheijen, T. Gregorkiewicz, and M. C. M. Van De Sanden, “Ultrahigh throughput plasma processing of free standing silicon nanocrystals with lognormal size distribution,” *J. Appl. Phys.*, vol. 113, no. 13, p. 134306, 2013.

[43] H. Wiggers, R. Starke, and P. Roth, “Silicon Particle Formation by Pyrolysis of Silane in a Hot Wall Gasphase Reactor,” *Chem. Eng. Technol.*, vol. 24, no. 3, pp. 261–264, Mar. 2001.

[44] R. Anthony and U. Kortshagen, “Photoluminescence quantum yields of amorphous and crystalline silicon nanoparticles,” *Phys. Rev. B*, vol. 80, no. 11, pp. 1–6, Sep. 2009.

[45] C. R. Gorla, “Silicon and germanium nanoparticle formation in an inductively coupled plasma reactor,” *J. Vac. Sci. Technol. A Vacuum, Surfaces, Film.*, vol. 15, no. 3, p. 860, May 1997.

[46] R. Gresback, T. Nozaki, and K. Okazaki, “Synthesis and oxidation of luminescent silicon nanocrystals from silicon tetrachloride by very high frequency nonthermal plasma.,” *Nanotechnology*, vol. 22, no. 30, p. 305605, Jul. 2011.

[47] Y. Ding, R. Gresback, R. Yamada, K. Okazaki, and T. Nozaki, “Hybrid Silicon Nanocrystal/Poly(3-hexylthiophene-2,5-diyl) Solar Cells from a Chlorinated Silicon Precursor,” *Jpn. J. Appl. Phys.*, vol. 52, no. 11S, p. 11NM04, Nov. 2013.

[48] R. Gresback, S. Kanegae, T. Nozaki, and K. Okazaki, “Nonthermal Plasma Synthesis and Oxidation Mechanisms of Photoluminescent Silicon Nanocrystals from Silicon Tetrachloride,” *Ispc_20*, pp. 2–5, 2011.

[49] U. Kortshagen, “Nonthermal Plasma Synthesis of Nanocrystals: Fundamentals, Applications, and Future Research Needs,” *Plasma Chem. Plasma Process.*, vol. 36, no. 1, pp. 73–84, Jan. 2016.

[50] T. Hülser, S. M. Schnurre, H. Wiggers, and C. Schulz, “Gas-phase synthesis of nanoscale silicon as an economical route towards sustainable energy technology,” *KONA Powder Part. J.*, vol. 29, pp. 191–207, 2011.

[51] J. Knipping, H. Wiggers, B. Rellinghaus, P. Roth, D. Konjhodzic, and C. Meier, “Synthesis of High Purity Silicon Nanoparticles in a Low Pressure Microwave Reactor,” *J. Nanosci. Nanotechnol.*, vol. 4, no. 8, pp. 1039–1044, Nov. 2004.

[52] B. Giesen, H. Wiggers, A. Kowalik, and P. Roth, “Formation of Si-nanoparticles in a microwave reactor: Comparison between experiments and modelling,” *J. Nanoparticle Res.*, vol. 7, no. 1, pp. 29–41, 2005.

[53] M. Gatti and U. Kortshagen, “Analytical model of particle charging in plasmas over a wide range of collisionality,” *Phys. Rev. E*, vol. 78, no. 4, p. 046402, Oct. 2008.

[54] Y. Nakamura *et al.*, “Anomalous reduction of thermal conductivity in coherent nanocrystal architecture for silicon thermoelectric material,” *Nano Energy*, vol. 12, pp. 845–851, Mar. 2015.

[55] Y. Ding, R. Gresback, Q. Liu, S. Zhou, X. Pi, and T. Nozaki, “Silicon nanocrystal conjugated polymer hybrid solar cells with improved performance,” *Nano Energy*, vol. 9, pp. 25–31, 2014.

[56] Y. Ding, S. Zhou, F. B. Juangsa, M. Sugaya, X. Zhang, Y. Zhao, and T. Nozaki, “Double-parallel-junction hybrid solar cells based on silicon nanocrystals,” *Org. Electron.*, vol. 30, pp. 99–104, Mar. 2016.

[57] M. S. Dresselhaus, G. Chen, M. Y. Tang, R. G. Yang, H. Lee, D. Z. Wang, Z. F. Ren, J.-P. Fleurial, and P. Gogna, “New Directions for Low-Dimensional Thermoelectric Materials,” *Adv. Mater.*, vol. 19, no. 8, pp. 1043–1053, Apr. 2007.

[58] Z. Han and A. Fina, “Thermal conductivity of carbon nanotubes and their polymer nanocomposites: A review,” *Prog. Polym. Sci.*, vol. 36, no. 7, pp. 914–944, Jul. 2011.

Chapter 2: Bulk-size Thermal Properties of SiNCs and PS Nanocomposite

This chapter is an adaptation of the published work: Firman Bagja Juangsa, Yoshiki Muroya, Meguya Ryu, Junko Morikawa, Tomohiro Nozaki, (2016). Thermal conductivity of silicon nanocrystals and polystyrene nanocomposite thin films. *Journal of Physics D: Applied Physics*, 49(36), 365303.

2.1. Abstract

Silicon nanocrystals (SiNCs) are well known for their size-dependent optical and electronic properties; they also have the potential for low yet controllable thermal properties. As a silicon-based low-thermal conductivity material is required in microdevice applications, SiNCs can be utilized for thermal insulation. In this paper, SiNCs and polymer nanocomposites were produced, and their thermal conductivity, including the density and specific heat, was measured. Measurement results were compared with thermal conductivity models for composite materials, and the comparison shows a decreasing value of the thermal conductivity, indicating the effect of the size and presence of the nanostructure on the thermal conductivity. Moreover, employing silicon inks at room temperature during the fabrication process enables a low cost of fabrication and preserves the unique properties of SiNCs.

2.2. Introduction

Nanocomposites, or inorganic/organic hybrid structures, have been widely used as promising structures for optoelectronic devices such as solar cells and light emitting devices [1], [2]. They have also been employed in enhancing the thermal conductivity of polymer materials by blending the conductive nanofiller within the polymer matrix [3]–[5]. However, in contrast to other device applications, such as thermoelectric applications, a very low thermal conductivity material is required to increase the device efficiency. In other electronic applications, heat management plays an essential role in maintaining device performance. In microdevice or microsystems, such as microsensors, thermal insulation is required to produce a reliable and highly sensitive device. Current methods that use Si structures have the disadvantage of poor mechanical stability, while the employment of polymer materials is not compatible with well-developed semiconductor technology [6]. A silicon-based nanocomposite material with low thermal conductivity has the ability to overcome these problems.

Silicon nanocrystals (SiNCs) have been widely studied for their size-dependent optical and electronic properties [7]–[10]. These size-dependent properties have been studied for the application of SiNCs in electronic devices such as hybrid solar cells, transistors, and bio-imaging devices [11], [12]. In addition to these optical and electronic properties, SiNCs have also shown a size-dependent behavior with respect to their thermal properties, with promising results achieved for the adjustable thermal conductivity properties of silicon by controlling the particle grain size [13]. Wang et al. reported a significant decrease in the thermal conductivity with smaller silicon particle sizes of 64 nm – 550 nm, where the samples were prepared by current-activated, pressure assisted densification (CAPAD) utilizing mechanical pressing, followed by high-temperature annealing at a temperature above 1200 ^{0}C [13]. Controllable thermal properties of SiNCs have attracted research activity for various applications. In this work, we have produced SiNCs-based nanocomposites with low thermal conductivity.

The thermal conductivity of a material is basically determined by the electron and phonon (lattice vibration) transport. However, in non-metal materials such as silicon, phonon transport mainly determines the thermal conductivity. In this work, nanocrystalline silicon particles with a mean size of 6 nm have been produced. By dispersing the SiNCs into the polymer matrix, the overall thermal conductivity of the nanocomposite is expected to decrease. With a smaller size of SiNCs, there will be a significant increase in the boundary scattering within the SiNCs. Furthermore, by dispersing SiNCs within the polymer matrix, a nanostructured network is created where phonons also experience a significant amount of scattering at the NC/polymer interfaces. As a result, the thermal conductivity of the nanocomposite material is expected to decrease significantly. Additionally, with low-temperature processes, the unique size-dependent properties (the quantum size effect) can be preserved, and low-cost fabrication is highly possible.

2.3. Thermal Conductivity Measurement and Analysis

The nanocomposite sample will be measured for its thermal properties, consists of thermal diffusivity, density, and specific heat. From the measurement results, thermal conductivity can be determined based thermal diffusivity (α), density (ρ), and specific heat (c_p) as the following formula,

$$k = \alpha \rho c_p \tag{2-1}$$

Temperature wave analysis (TWA) is one of the methods to measure the cross-plane/through-thickness direction thermal diffusivity of the specimen. Its measurement is based on the phase shift of temperature wave between the front and the rear surface of the sample [14]. This method through its development has been reported successfully for thermal diffusivity/conductivity on various thin films such as polyimide thin film [15]–[17], low-*k* dielectric thin film[18], single crystals [14] and many other kinds of polymers [19]–[24].

TWA measurement is carried out based on a one-dimensional temperature wave conduction model, as presented in Figure 2-1. The sample is placed between two electrodes and measured for its' cross-plane direction thermal diffusivity. The substrates attached to the samples are assumed very thick enough

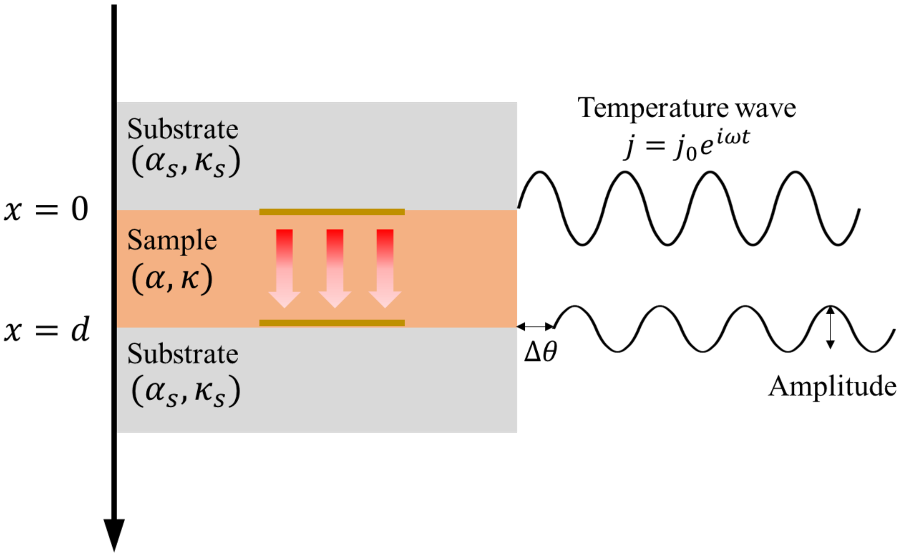

Figure 2-1 One dimensional temperature wave conduction model

Both surfaces of the sample were attached by indium tin oxide (ITO) layer that acts as a heater on the front surface and very thin gold layer as the sensor on the rear surface. Gold is used for its high-temperature-coefficient of resistance and its stability under repeated heating and cooling. Temperature wave is generated with frequency controlled by the frequency generator. The temperature wave is captured on the sensor layer, and the wave signal goes through the amplifier to be processed and analyzed in the PC.

The detail explanation and equation derivation has been published elsewhere [14], [25], [26]. It is assumed that the thickness of the substrate is much thicker than the thin film so that temperature wave in infinite points are zero. It is also assumed that thermal contact resistance at the boundary of the specimen and sputtered sensor/heater are negligible because sputtered layers are much thinner than the specimen thickness and the good adhesive is obtained in the sputtering procedure so that temperature is continuous at the boundaries.

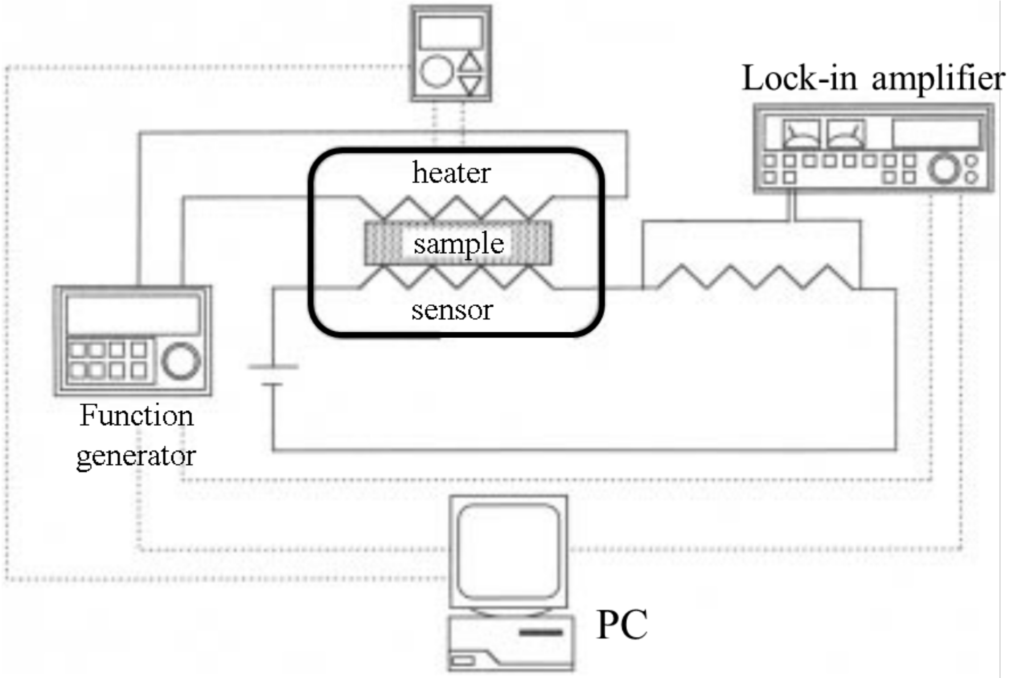

Figure 2-2. Schematic diagram of the temperature wave analysis measurement system [26].

The numerical solution for TWA is derived based on the one-dimensional conduction model displayed in Figure 2-1. The heat flow in cross-plane direction is described by one–dimensional heat diffusion equations along the x axis are shown in following equations,

$$\frac{\partial T}{\partial t} = \alpha_s \frac{\partial^2 T}{\partial x^2} \quad (x \leq 0) \tag{2-2}$$

$$\frac{\partial T}{\partial t} = \alpha \frac{\partial^2 T}{\partial x^2} \quad (0 < x < d) \tag{2-3}$$

$$\frac{\partial T}{\partial t} = \alpha_s \frac{\partial^2 T}{\partial x^2} \quad (d < x) \tag{2-4}$$

Where T is temperature, α is thermal diffusivity of sample, and α_s is thermal diffusivity of substrates. It is also assumed that contact resistance at boundaries of substrates and sample are neglected, resulting in the continuous temperature distribution at boundaries, which is defined by

$$T(-0, t) = T(+0, t) \tag{2-5}$$

$$T(d - 0, t) = T(d + 0, t) \tag{2-6}$$

Heat flux is applied at $x = 0$, creating a thermal balance at interfaces between substrates ad sample as follow.

$$\kappa_s \left.\frac{\partial T}{\partial t}\right|_{x \to -0} - \kappa \left.\frac{\partial T}{\partial t}\right|_{x \to +0} = q(t) = q_0 e^{(i\omega t)} \tag{2-7}$$

$$\kappa \left.\frac{\partial T}{\partial t}\right|_{x \to d-0} - \kappa_s \left.\frac{\partial T}{\partial t}\right|_{x \to d+0} = 0 \tag{2-8}$$

Where κ and κ_s are thermal conductivities of the sample and substrates, respectively. Heat flux is generated by AC joule heating and represented by $q(t)$.

The above equations can be solved in complex function through Laplace transform $T(x, t) \to \theta(x, s)$, resulting in the equations transformed as follow.

$$s\theta(x, s) = \alpha_s \frac{\partial^2}{\partial x^2} \theta(x, s) \qquad (x \le 0) \tag{2-9}$$

$$s\theta(x, s) = \alpha \frac{\partial^2}{\partial x^2} \theta(x, s) \qquad (0 < x < d) \tag{2-10}$$

$$s\theta(x, s) = \alpha_s \frac{\partial^2}{\partial x^2} \theta(x, s) \qquad (d \le x) \tag{2-11}$$

$$\theta(-0,s) = \theta(+0,s) \tag{2-12}$$

$$\theta(d-0,s) = \theta(d+0,s) \tag{2-13}$$

$$\kappa_s \frac{\partial}{\partial t}\theta(x,s)\bigg|_{x\to -0} - \kappa \frac{\partial}{\partial t}\theta(x,s)\bigg|_{x\to +0} = \frac{q_0}{s - i\omega} \tag{2-14}$$

$$\kappa \frac{\partial}{\partial t}\theta(x,s)\bigg|_{x\to d-0} - \kappa_s \frac{\partial}{\partial t}\theta(x,s)\bigg|_{x\to d+0} = 0 \tag{2-15}$$

Since equation (2-9) ~ (2-11) are a single variable function of x, they can be converted as $\theta(x,s) = e^{ux}$, with $(u = constant)$.

$$\frac{s}{\alpha_s} e^{ux} = u^2 e^{ux} \qquad (x \le 0) \tag{2-16}$$

$$\frac{s}{\alpha} e^{ux} = u^2 e^{ux} \qquad (0 < x < d) \tag{2-17}$$

$$\frac{s}{\alpha_s} e^{ux} = u^2 e^{ux} \qquad (d \le x) \tag{2-18}$$

Which has the result of u along thickness direction as follow

$$u = \pm\sqrt{\frac{s}{\alpha_s}} \qquad (x \le 0) \tag{2-19}$$

$$u = \pm\sqrt{\frac{s}{\alpha}} \qquad (0 < x < d) \tag{2-20}$$

$$u = \pm\sqrt{\frac{s}{\alpha_s}} \qquad (d \le x) \tag{2-21}$$

If the above equations are substituted back to equation (2-9), (2-10), and (2-11), complex function form of temperature distribution $\theta(x,s)$ is given by,

$$\theta(x,s) = C_1(s)e^{-\sqrt{\frac{s}{\alpha_s}}x} + C_2(s)e^{+\sqrt{\frac{s}{\alpha_s}}x} \qquad (x \le 0) \tag{2-22}$$

$$\theta(x,s) = C_3(s)e^{-\sqrt{\frac{s}{\alpha}}x} + C_4(s)e^{+\sqrt{\frac{s}{\alpha}}x} \qquad (0 < x < d) \tag{2-23}$$

$$\theta(x,s) = C_5(s)e^{-\sqrt{\frac{s}{\alpha_s}}x} + C_6(s)e^{+\sqrt{\frac{s}{\alpha_s}}x} \qquad (d \leq x) \tag{2-24}$$

Since substrates are assumed very thick, the temperature at the infinite point can be defined as $T(x \to \pm\infty, t) = 0$, resulting in $C_1(s) = C_6(s) = 0$ and giving the temperature distribution equations as follow,

$$\theta(x,s) = C_2(s)e^{+\sqrt{\frac{s}{\alpha_s}}x} \qquad (x \leq 0) \tag{2-25}$$

$$\theta(x,s) = C_3(s)e^{-\sqrt{\frac{s}{\alpha}}x} + C_4(s)e^{+\sqrt{\frac{s}{\alpha}}x} \qquad (0 < x < d) \tag{2-26}$$

$$\theta(x,s) = C_5(s)e^{-\sqrt{\frac{s}{\alpha_s}}x} \qquad (d \leq x) \tag{2-27}$$

At interfaces between substrates and sample, the temperature is defined based on condition (2-5) and (2-6), which is expressed in complex function form as following equations,

$$C_2(s) = C_3(s) + C_4\,(s) \qquad (x = 0) \tag{2-28}$$

$$C_3(s)e^{-\sqrt{\frac{s}{\alpha}}} + C_4(s)e^{+\sqrt{\frac{s}{\alpha}}} = C_5(s)e^{-\sqrt{\frac{s}{\alpha_s}}} \qquad (x = d) \tag{2-29}$$

While the heat flux balance equation (2-14) and (2-15) are rewritten as follow,

$$\kappa_s\sqrt{\frac{s}{\alpha_s}}C_2(s) - \kappa\sqrt{\frac{s}{\alpha}}C_3(s) + -\kappa\sqrt{\frac{s}{\alpha}}C_4(s) = \frac{j}{s - i\omega} \tag{2-30}$$

$$-\kappa\sqrt{\frac{s}{\alpha}}C_3(s)e^{-\sqrt{\frac{s}{\alpha}}d} + \kappa\sqrt{\frac{s}{\alpha}}C_4(s)e^{+\sqrt{\frac{s}{\alpha}}d} - \kappa_s\sqrt{\frac{s}{\alpha_s}}C_5(s)e^{-\sqrt{\frac{s}{\alpha_s}}d} = 0 \tag{2-31}$$

Therefore, C_2, C_3, C_4, C_5 can be obtained mathematically as follow:

$$C_2(s) = \frac{q_0\left[\kappa\sqrt{\frac{s}{\alpha}} - \kappa_s\sqrt{\frac{s}{\alpha_s}} + e^{\sqrt{\frac{s}{\alpha}}2d}\left(\kappa\sqrt{\frac{s}{\alpha}} + \kappa_s\sqrt{\frac{s}{\alpha_s}}\right)\right]}{(s - i\omega)\left[-\left(\kappa\sqrt{\frac{s}{\alpha}} - \kappa_s\sqrt{\frac{s}{\alpha_s}}\right)\left(\kappa\sqrt{\frac{s}{\alpha}} - \kappa_s\sqrt{\frac{s}{\alpha_s}}\right) + e^{\sqrt{\frac{s}{\alpha}}2d}\left(\kappa\sqrt{\frac{s}{\alpha}} + \kappa_s\sqrt{\frac{s}{\alpha_s}}\right)\left(\kappa\sqrt{\frac{s}{\alpha}} + \kappa_s\sqrt{\frac{s}{\alpha_s}}\right)\right]} \tag{2-32}$$

$$C_3(s) = \frac{q_0\left[\kappa\sqrt{\frac{s}{\alpha}} + \kappa_s\sqrt{\frac{s}{\alpha_s}}\right]e^{\sqrt{\frac{s}{\alpha}}2d}}{(s - i\omega)\left[-\left(\kappa\sqrt{\frac{s}{\alpha}} - \kappa_s\sqrt{\frac{s}{\alpha_s}}\right)\left(\kappa\sqrt{\frac{s}{\alpha}} - \kappa_s\sqrt{\frac{s}{\alpha_s}}\right) + e^{\sqrt{\frac{s}{\alpha}}2d}\left(\kappa\sqrt{\frac{s}{\alpha}} + \kappa_s\sqrt{\frac{s}{\alpha_s}}\right)\left(\kappa\sqrt{\frac{s}{\alpha}} + \kappa_s\sqrt{\frac{s}{\alpha_s}}\right)\right]} \tag{2-33}$$

$$C_4(s) = \frac{q_0\left[\kappa\sqrt{\frac{s}{\alpha}} + \kappa_s\sqrt{\frac{s}{\alpha_s}}\right]}{(s - i\omega)\left[-\left(\kappa\sqrt{\frac{s}{\alpha}} - \kappa_s\sqrt{\frac{s}{\alpha_s}}\right)\left(\kappa\sqrt{\frac{s}{\alpha}} - \kappa_s\sqrt{\frac{s}{\alpha_s}}\right) + e^{\sqrt{\frac{s}{\alpha}}2d}\left(\kappa\sqrt{\frac{s}{\alpha}} + \kappa_s\sqrt{\frac{s}{\alpha_s}}\right)\left(\kappa\sqrt{\frac{s}{\alpha}} + \kappa_s\sqrt{\frac{s}{\alpha_s}}\right)\right]} \tag{2-34}$$

$$C_5(s) = \frac{2q_0\kappa\sqrt{\frac{s}{\alpha}}e^{\left(\sqrt{\frac{s}{\alpha}}+\sqrt{\frac{s}{\alpha_s}}\right)d}}{(s - i\omega)\left[-\left(\kappa\sqrt{\frac{s}{\alpha}} - \kappa_s\sqrt{\frac{s}{\alpha_s}}\right)\left(\kappa\sqrt{\frac{s}{\alpha}} - \kappa_s\sqrt{\frac{s}{\alpha_s}}\right) + e^{\sqrt{\frac{s}{\alpha}}2d}\left(\kappa\sqrt{\frac{s}{\alpha}} + \kappa_s\sqrt{\frac{s}{\alpha_s}}\right)\left(\kappa\sqrt{\frac{s}{\alpha}} + \kappa_s\sqrt{\frac{s}{\alpha_s}}\right)\right]} \tag{2-35}$$

As the coefficients have been obtained, the solution for temperature distribution is given by inverse Laplace transform as follow,

$$T(0,t) = \mathcal{L}^{-1}\big(\theta(0,s)\big) = \mathcal{L}^{-1}C_2(s) = \frac{1}{2\pi i}\int_{c-i\infty}^{c+i\infty}[C_2(s)e^{st}]ds$$

$$T(0,t) = \lim_{s\to i\omega}(s - i\omega)C_2(s)e^{st}$$

$$T(0,t) = \frac{q_0\big[(k\kappa + k_s\kappa_s) + (k\kappa + k_s\kappa_s)e^{(-2kd(1+i)}\big]e^{\left(i\left(\omega t-\frac{\pi}{4}\right)\right)}}{\sqrt{2}[(k\kappa + k_s\kappa_s)^2 - (k\kappa - k_s\kappa_s)^2e^{(-2kd(1+i)}]} \tag{2-36}$$

$$T(d,t) = \mathcal{L}^{-1}\big(\theta(d,s)\big) = \mathcal{L}^{-1}C_5(s)e^{-\sqrt{\frac{s}{\alpha_s}}d} = \frac{1}{2\pi i}\int_{c-i\infty}^{c+i\infty}\left[C_5(s)e^{-\sqrt{\frac{s}{\alpha_s}}d}e^{st}\right]ds$$

$$T(d,t) = \lim_{s\to i\omega}(s - i\omega)C_5(s)e^{-\sqrt{\frac{s}{\alpha_s}}d}e^{st}$$

$$T(d,t) = \frac{\sqrt{2}\,q_0k\kappa e^{-kd}e^{\left(i\left(\omega t-kd-\frac{\pi}{4}\right)\right)}}{(k\kappa + k_s\kappa_s)^2 - (k\kappa - k_s\kappa_s)^2e^{(-2kd(1+i)}} \tag{2-37}$$

Where $k = \sqrt{\frac{\omega}{2\alpha}}$ and $k_s = \sqrt{\frac{\omega}{2\alpha_s}}$, representing the reciprocal thermal length of temperature wave. According to Euler formula, $\sqrt{i} = e^{\frac{i\pi}{4}} = \frac{1+i}{\sqrt{2}}$, resulting in the temperature distribution equation converted as follow,

$$T(d,t) = \frac{\left[\frac{q_0e^{i\omega t}}{(1+i)}\right]e^{-(1+i)kd}}{\frac{(k\kappa + k_s\kappa_s)^2 - (k\kappa - k_s\kappa_s)^2e^{(-2kd(1+i))}}{2k\kappa}} \tag{2-38}$$

As previously mentioned, the sufficiently thick sample is required in order to determine the phase shift of temperature wave. Thermally thick condition is represented by $kd > 1$, so that temperature distribution equation can be approximated by the following formula.

$$T(d,t) = \frac{\sqrt{2}q_0 k\kappa e^{(-kd)} e^{\left(i\left(\omega t - kd - \frac{\pi}{4}\right)\right)}}{(k\kappa + k_s\kappa_s)^2} \tag{2-39}$$

Where T is temperature, t is time, α is thermal diffusivity of the specimen, and α_s is thermal diffusivity of the substrates. Then, temperature wave at $x = d$ is described as below [14], [25], [27].

$$T(d,t) = \frac{\sqrt{2}q_0 \kappa k e^{(-kd)}}{(\kappa k + \kappa_s k_s)^2} e^{(i(\omega t - kd - \frac{\pi}{4})} \tag{2-40}$$

where $k = \sqrt{\omega/2\alpha}$ and $k_s = \sqrt{\omega/2\alpha_s}$.

From the above equation, the temperature wave phase shift between the front and the rear surface and thermal diffusivity can be derived as below, respectively.

$$\Delta\theta = -\sqrt{\frac{\omega}{2\alpha}}d - \frac{\pi}{4} \tag{2-41}$$

$$\alpha = \pi\left(\frac{d}{\left(\Delta\theta + \frac{\pi}{4}\right)\Big/\sqrt{f}}\right)^2 \tag{2-42}$$

By varying the frequency of temperature wave, a curve obtained by plotting the square root of the frequency ($\sqrt{f}$) against the phase shift ($\Delta\theta$). The curve is a linear function as shown in Figure 2-3 Example of phase shift $\Delta\theta$ against the square root of temperature frequency $\sqrt{\mathrm{f}}$ as the result of TWA measurementFigure 2-3. The thermal diffusivity (α) can be determined from the slope of the curve for a known sample thickness (d) as presented in equation (2-42).

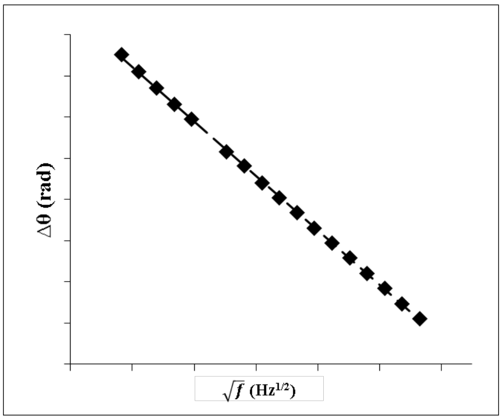

Figure 2-3 Example of phase shift $\Delta\theta$ against the square root of temperature frequency $\sqrt{f}$ as the result of TWA measurement

In addition, the frequency sweep range during TWA measurement is critical as it determines the thermal diffusion length (μ; $\mu = \frac{1}{k} = \frac{\alpha}{\pi f}$) in the sample. Temperature wave at high frequencies produces a short thermal diffusion length because the temperature wave decays at near of the sample surface. This condition is called thermally thick, which is well-suited to measurements of thermal diffusivity with minor external disturbances. On the contrary, low frequency temperature wave has a long thermal diffusion length, which is important to be considered with the comparison with the sample thickness. An ideal sample thickness should be larger than the thermal diffusion length $\left(\frac{d}{\mu} = kd > 1\right)$, in order to avoid the noise/disturbance from environmental condition. Therefore it is important to determine the frequency range based on the sample thickness to achieve thermally thick measurement condition ($kd > 1$).

2.4. Experiment

SiNCs were synthesized by non-thermal plasma CVD. The gas phase nucleation and growth occurred, and highly crystalline SiNCs were synthesized, with excellent, narrow size distribution and mean size of 6 nm [28]–[30]. The synthesis apparatus consisted of a quartz tube reactor with an inner diameter of 45 mm, and with 2 copper electrodes attached to the tube. A very high frequency (VHF) 70 MHz power source supplied the reactor. SiNCs were synthesized from $SiCl_4$, H_2, and Ar with a volumetric ratio of 1:10:30, respectively. The reactor pressure was fixed at 400 Pa, and the input power was set to 80 W. As-produced SiNCs were dry etched by hydrofluoric (HF) acid vapor so that the SiNCs are mostly terminated by hydrogen. The SiNCs were placed on a Teflon mesh above a 50% HF/water solution in a closed container at room temperature for at least 48 hours [31].

The nanocomposite material was made from the SiNCs and an organic polymer. The SiNCs have to be dispersed in the polymer matrix, and the low-cost polymer is required for mass production. Polystyrene (PS) was used as the polymer matrix for the nanocomposite material due to its abundance and low cost. Moreover, various physical properties of PS, such as the crystallinity and molecular weight, can be altered, allowing the possibility of creating tunable models for further analysis. Commercially available atactic polystyrene (Sigma-Aldrich 430102), with an average M_w: ~192,000, was used for this work. The SiNCs and PS were dispersed separately in benzonitrile (anhydrous, Sigma-Aldrich 294098) with predetermined concentrations, as shown in Table 2-1. The same amount of each solution was taken and mixed. The volume fraction of each sample was determined based on the density reference values of silicon and PS (2.329 g/cm^3 and 1.05 g/cm^3, respectively) [32], [33]. The mixed solution of the SiNCs and PS was stirred for 24 hours to obtain a stable, well-dispersed solution. The resulting solution was deposited on the substrate by spin casting to produce nanocomposite thin films. Each thin film sample was dried in a vacuum chamber (<1 Pa) for more than 12 hours to avoid the trapping of gas within the sample.

Table 2-1 Nanocomposite Experimental Condition

No	SiNCs Concentration (mg/cm^3)	PS Concentration (mg/cm^3)	SiNCs Mass Fraction (%)	SiNCs Volume Fraction (%)	Sample Thickness	
					(μm)	Error (μm)
1	0	300	0	0	11.99	0.06
2	25	300	7.7	3.6	4.00	0.05
3	50	300	14.3	7.0	5.61	0.12
4	75	300	20	10.1	6.03	0.33
5	75	75	50	31.1	5.17	0.63

Extensive material characterization was performed by FT-IR and Raman Spectroscopy on the SiNCs and PS as the original material, and also on the nanocomposite materials to analyze whether there were any changes to the chemical and molecular structure. Additionally, transmission electron microscopy (TEM) and atomic force microscopy (AFM) were used to analyze the dispersion of the SiNCs in the PS matrix and the particle size distribution of the SiNCs, respectively.

The structure of the sample measured in this work is shown in Figure 2-4(a). Pre-coated ITO layer on the glass substrate was used as a heating element. ITO layer with a thickness of 250 nm was firstly patterned by photolithography. A very thin layer of gold was then deposited on the electrode part of ITO to enhance the electrical conductivity. The thin film sample was produced by spin coating on the glass substrate. The temperature wave was generated by a function generator on the heating layer by AC Joule heating. The sensing element is used for detecting a temperature wave by measuring the oscillation of the electric resistance of the electric resistor attached to the rear surface. The sensing element was made of gold deposited by magnetron sputtering in order to prevent heating the sample. The direct sputtering on the thin film was done with a very slow rate of 5 nm/min, due to the low glass temperature of PS. Finally, the wiring was attached to the electrode by silver paste and encapsulated by epoxy.

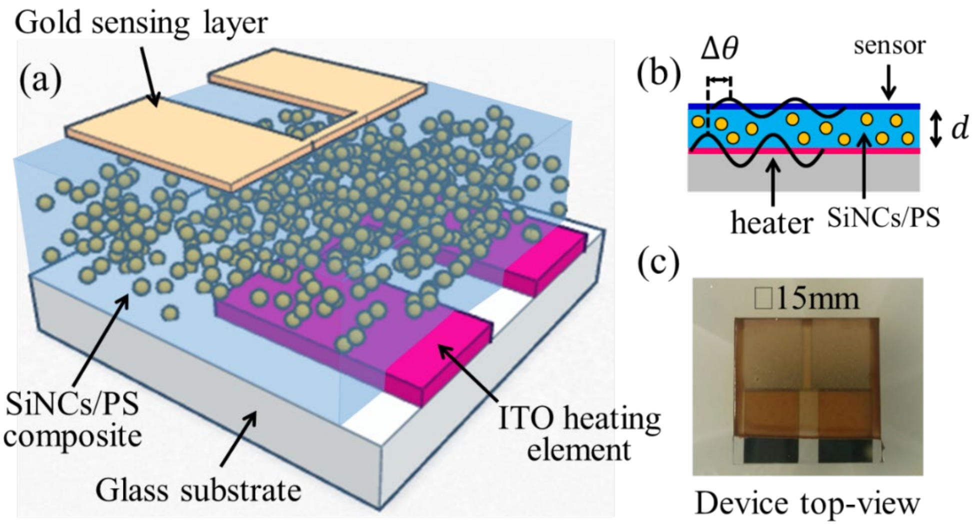

Figure 2-4 (a) Configuration of TWA sensing device, (b) Temperature wave propagation through nanocomposite thin film towards sensing layer with a phase shift of $\Delta\theta$, (c) A top view of TWA sensing device.

The thermal conductivity of the nanocomposite sample was determined based on thermal diffusivity, density and specific heat measurements by Temperature Wave Analysis (TWA), densimeter, and calorimeter, respectively. Briefly, Figure 2-4(b) shows the TWA measurement structure employed in this study, where the nanocomposite thin film is sandwiched between the heater layer and sensor layer. The specimen for TWA measurement is displayed in Figure 2-4(c). The thermal conductivity is determined based on the thermal diffusivity (α), the density (ρ), and the specific heat (c_p) as the following formula:

$$\kappa = \alpha\rho c_p \qquad (2\text{-}43)$$

The nanocomposite sample density was measured by an electronic densimeter (Alfamirage SD-200L) and the specific heat was measured by a Differential Scanning Calorimeter (DSC) (Perkin-Elmer DSC-7). The sample thickness was measured by a profilometer or micro figure measuring instrument (Kosaka Lab, Surfcorder ET200). The thickness was determined by the average value from 10 measurements of the thin film thickness in random positions of the sample, as shown in Table 2-1.

Uniform film thickness is critically important for the accurate determination of the overall thermal diffusivity as formulated in equation (1). Samples with a SiNCs volume fraction higher than 31.1% show a dramatic increase in their surface roughness, and uniform film thickness can no longer be achieved. Therefore, samples containing SiNCs with more than 31.1vol% were excluded from further analysis. The maximum mixing ratio of the SiNCs in the PS matrix was approximately 74%, assuming a hexagonal close packing filling factor [31], as shown in Figure 7. This implies that a SiNCs volume fraction between ca. 74% and 100% is not feasible for the thermal conductivity measurement. It is important to mention that 100% SiNC thin films are obtainable, however, thermal properties of porous SiNC films, without the filling polymer, must be excluded because these films are different composite materials from the SiNCs/PS blended thin films.

2.5. Result and Discussion

2.5.1. Sample Characterization

Figure 2-5 shows a cross-section TEM image. The SiNCs are freestanding, with sizes of approximately 5-7 nm, and dispersed within the PS matrix. Samples with a higher mass fraction of the SiNCs show better dispersion due to the higher concentration of SiNCs, whereas some agglomeration of SiNCs was observed in samples with a lower mass fractions of the SiNCs.

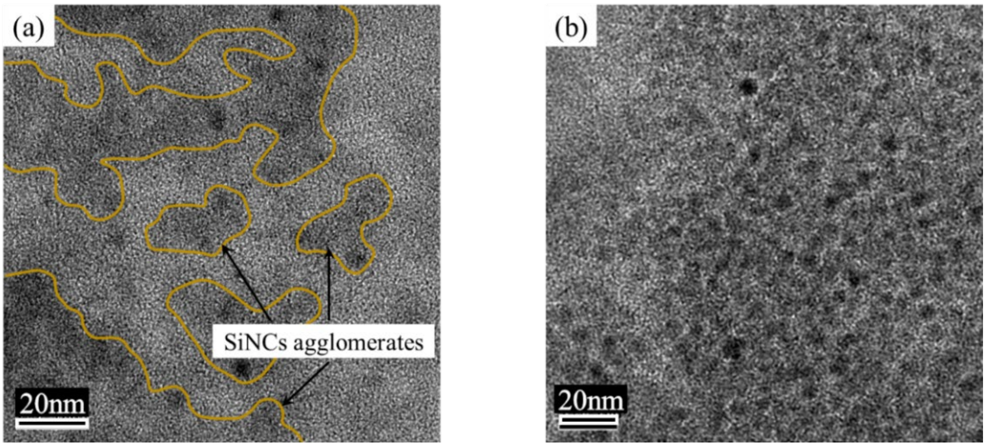

Figure 2-5. TEM image of SiNCs/PS Nanocomposite: (a) SiNCs volume fraction 3.6%; (b) SiNCs volumep fraction 31.1%

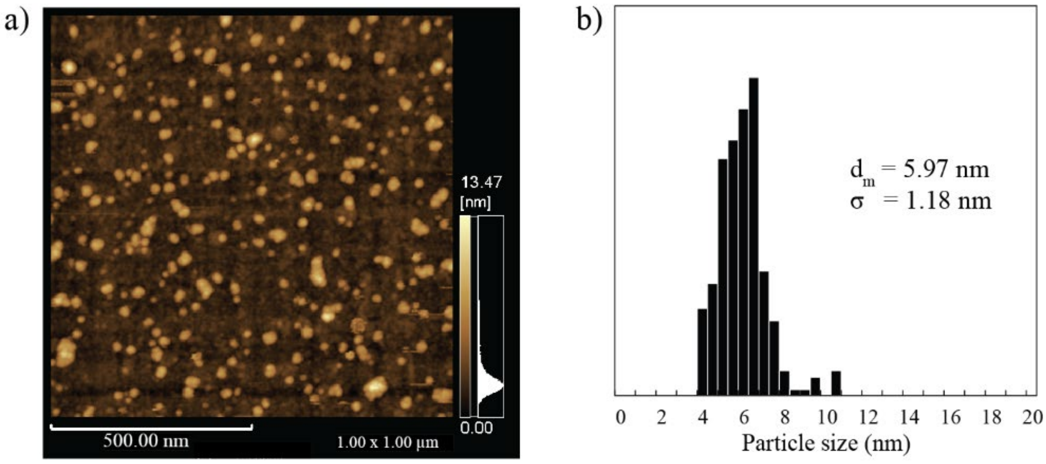

Figure 2-6. Size distribution of SiNCs: (a) AFM image of SiNCs, (b) Statistic of SiNCs size distribution

SiNC particles were analyzed by atomic force microscope (AFM, SPM-9600; Shimadzu Corp.), as shown in Figure 2-6 (a). More than 250 particles were counted for statistical analysis, and Figure 2-6 (b) shows the narrow size distribution of the SiNCs with a mean diameter of 5.97 nm.

Figure 2-7 and Figure 2-8 show Raman (STR750 Laser Raman Spectrometer; Seki Technotron Corp.) and FT-IR Spectroscopy (FTIR-6100; Jasco Corp.) results from the nanocomposite compared with the original material, respectively. A laser with a wavelength of 532 nm was used for Raman spectroscopy, with a 4 × 15 s exposure time, a ×20 objective lens and an excitation power of 2.5 mW. For FT-IR, samples were deposited on one window of an air-free thallium bromoiodide (KRS-5) cell and the spectra were recorded in transmission mode. The composite sample with the highest SiNCs mass fraction of 50% (condition no.5 in Table 2-1) was analyzed by Raman and FT-IR spectroscopy, representing an identical result to the results observed from the other samples. Raman spectroscopy shows that the spectrum of the nanocomposite is a combination of that of the SiNCs and PS, without any significant change to the spectrum of each component. The Raman spectrum also confirmed a high crystallinity of the SiNCs, as shown by the sharp peak at 517 cm^{-1} in Figure 2-7 (inset). The SiNCs peak shifted from the bulk Si at 520 cm^{-1} to a lower wavenumber due to the phonon confinement effect, as was observed theoretically and experimentally for nanocrystals smaller than 20 nm [34]–[36]. However, it is important to note that this peak shift is also caused by stress on the sample [37]. It is also interesting to note that due to the large surface area of the SiNCs, an intense Si-H peak is also observed in Raman spectrum which is not common in bulk H:Si materials [38].

From FTIR spectroscopy of the nanocomposite sample, compared with the original spectrum, minor peak shifts could be observed at several points. The Si-H stretching mode peaks shifted from 2107 cm^{-1} to 2101 cm^{-1} and from 829 cm^{-1} to 822 cm^{-1}. The PS benzene ring deformation peak [39] shifted from 539 cm^{-1} to 545 cm^{-1}. The Si-H stretching mode is sensitive to changes in the environment. This peak shifted by less than 10 cm^{-1}, indicating that the shift is only caused by the physical interaction between the Si-H bonds and PS's benzene rings [40], [41]. The presence of the PS matrix among the SiNCs may suppress the Si-H bonding vibration and result in the shift to a lower wavenumber.

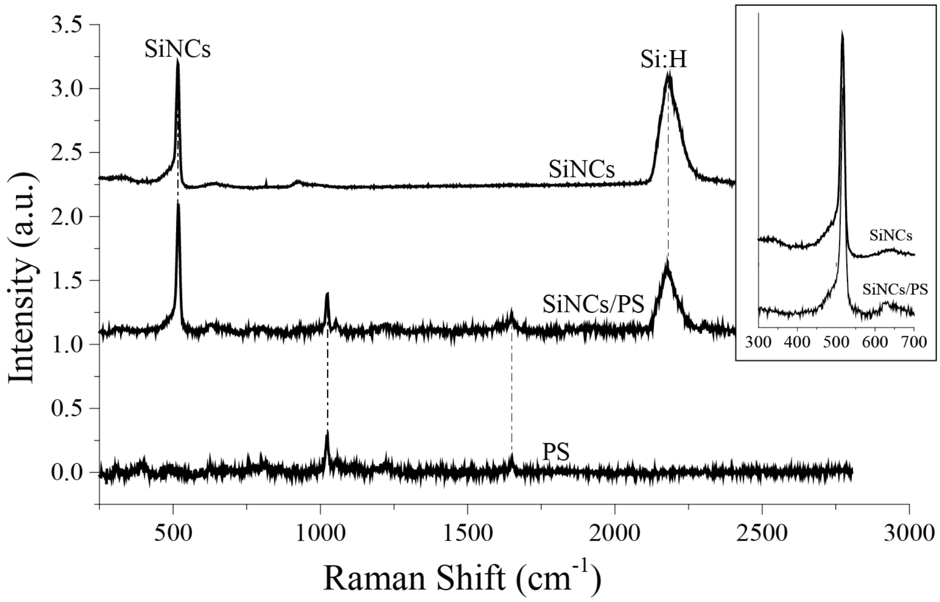

Figure 2-7 Raman spectrum of SiNCs, PS, and SiNCs/PS nanocomposite

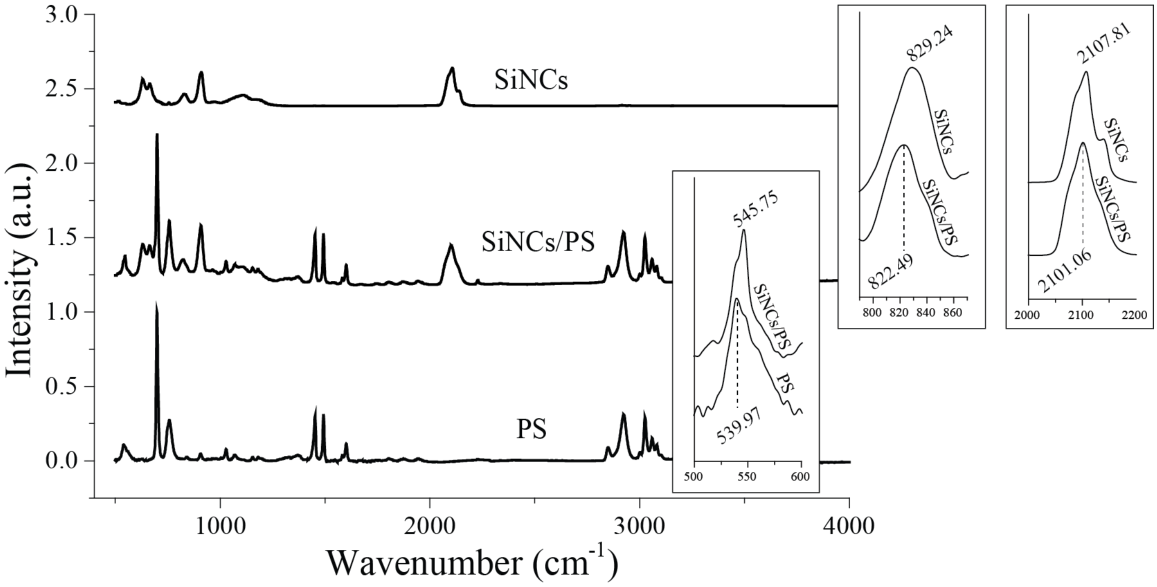

Figure 2-8 FT-IR spectrum of SiNCs, PS, and SiNCs/PS nanocomposite

In summary, both FTIR and Raman Spectroscopy confirmed that there was no chemical reaction or molecular structure change due to the mixture process during nanocomposite fabrication. The properties of the original materials properties, reflected in the nanocomposite spectrum, remained the same, indicating that the mixture results in a composite material. Additionally, from FTIR spectroscopy, the Si-O peak (at approximately 1100 cm^{-1}) was not observed from the spectrum, which is common if oxidation occurs during the fabrication process. This obviously confirmed that oxidation was prevented and the material condition was preserved during the fabrication process.

2.5.2. Density and Specific Heat

The TWA measurement determines the thermal diffusivity of the nanocomposite material, while the density and specific heat were determined experimentally by the hydrostatic and the DSC method, respectively. The density measurement results were compared with the reported reference values of PS (1.05 g/cm^3) and silicon (2.329 g/cm^3) [32], [42], which is shown in Figure 2-9 (a). It is shown that the measurement result has an increasing trend of mass density as SiNCs' fraction increase, because the mass density of silicon is higher than that of PS.

Specific heat values measured by DSC are also compared with calculation result based on the reference value of PS (1275 J/kg.K) and bulk silicon (710 J/kg.K) [32], [42], as shown in Figure 2-9(b). The measurement values show good agreement with the calculated reference value with a decreasing trend in terms of SiNCs fraction, because the specific heat of SiNCs is lower than that of PS. In relation to the specific heat, Kihara et al. reported that the surface oxidation of porous silicon results in an increase in the heat capacity per unit volume, due to changes in the density and specific heat [42]. Our results show no oxidation, as confirmed by the FT-IR spectrum, and there is no significant increase in the specific heat as shown in the DSC measurement result. Furthermore, the heat capacity of porous silicon was reported considerably lower than the value estimated from the porosity of the sample [42]. Heat capacity decrease may be observed as the result of confined material characteristic of nanocrystalline silicon [42]. This can be also observed in DSC measurement result of the nanocomposite, especially at a high fraction of SiNCs (50% mass), indicating that specific heat of SiNCs is lower than the bulk silicon value.

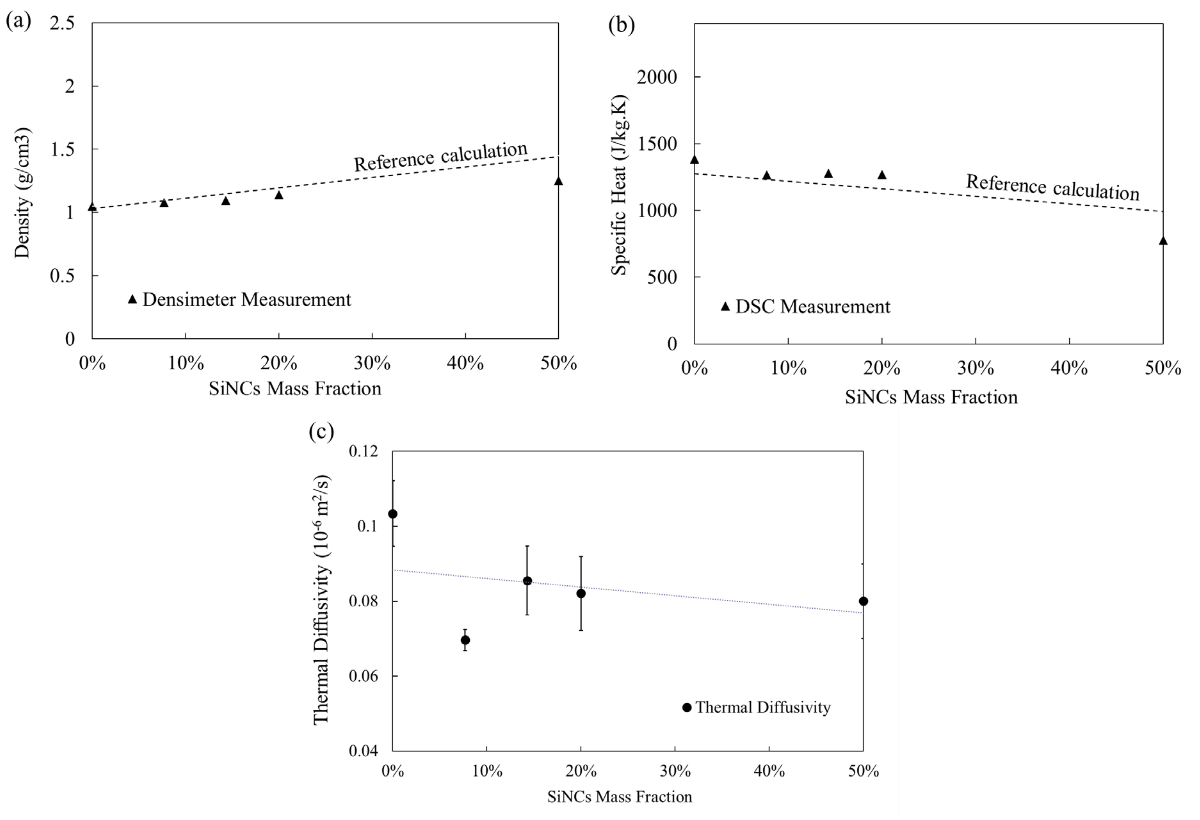

Figure 2-9. Measurement results of (a) density and (b) specific heat compared with the calculated data based on the reference value of SiNCs and PS, and (c) thermal diffusivity by TWA

2.5.3. Thermal Conductivity

The thermal diffusivity measurement result obtained by TWA is shown in Figure 2-9(c). It shows that the thermal diffusivity decreases relative to the SiNCs mass fraction, in spite of the fact that the SiNCs thermal diffusivity (6×10^{-6} m^2 s^{-1}) is higher than that of PS (1.17×10^{-7} m^2 s^{-1}) [32], [42].

The thermal conductivity was determined from the thermal diffusivity, density, and specific heat. The thermal conductivity, which was determined by the experimental data of the thermal diffusivity, density and specific heat, was compared with five fundamental structural thermal conductivity models for two-phase composite materials [43]. Since the first attempts by Maxwell

[44], influencing factors have been taken into account for determining the effective thermal conductivity such as the volume fraction, filler size and shape, and dispersion state. The models shown in Figure 2-10 are basic models for predicting the thermal conductivity of composite materials (κ_c) based on the volume fraction (φ) and thermal conductivity (κ) for each phase, with a different dispersion state for each model. Among five fundamental models, the parallel and series models represent the layered structures of the two-phase composite. Basically, the parallel and series refer to the direction of heat flux and the layer structure, as shown in equation (2-44) and (2-45), respectively.

$$\kappa_c = \varphi_1\kappa_1 + \varphi_2\kappa_2 \tag{2-44}$$

$$\kappa_c = \frac{1}{\varphi_1\kappa_1 + \varphi_2\kappa_2} \tag{2-45}$$

Maxwell-Eucken (ME) model represents a two-phase composite structure that has one continuous phase and another dispersed phase. ME model gives two thermal conductivity equations of ME1 and ME2, representing phase 1 or phase 2 that serve continuous phase, respectively.

$$\kappa_c = \frac{\varphi_1\kappa_1 + \varphi_2\kappa_2\frac{3\kappa_1}{2\kappa_1+\kappa_2}}{\varphi_1 + \varphi_2\frac{3\kappa_1}{2\kappa_1+\kappa_2}} \quad \text{ME1 (1=continuous, 2= dispersed)} \tag{2-46}$$

$$\kappa_c = \frac{\varphi_2\kappa_2 + \varphi_1\kappa_1\frac{3\kappa_2}{2\kappa_2+\kappa_1}}{\varphi_2 + \varphi_1\frac{3\kappa_2}{2\kappa_2+\kappa_1}} \quad \text{ME2 (2=continuous, 1= dispersed)} \tag{2-47}$$

Another fundamental thermal conductivity model of the two-phase composite is based on effective media theory (EMT), assuming both phases are in the dispersed condition in the composite structure. EMT model gives an equal contribution of both phases in the composite thermal conductivity, as shown in the following equation.

$$\varphi_1 \frac{\kappa_1 - \kappa_c}{\kappa_1 + 2\kappa_c} + \varphi_2 \frac{\kappa_2 - \kappa_c}{\kappa_2 + 2\kappa_c} = 0 \tag{2-48}$$

Figure 2-10 also shows the comparison of all five models and the experimental results of our work. Reference values for the thermal conductivity of SiNCs (1.08 W m^{-1} K^{-1}) and PS (0.1549 W m^{-1} K^{-1}) were used for the model calculations [32], [42].

The PS-only sample's measurement result showed good agreement with the reference value for the PS thermal conductivity; this agreement validated the sample fabrication process and the TWA measurement method. With the SiNCs introduced in the PS matrix, the five thermal conductivity models showed that the thermal conductivity of the nanocomposite increases with an increasing mass fraction of silicon simply because the reference value of the SiNCs' thermal conductivity is greater than that of PS. The five thermal conductivity models represent the various dispersion states in composite materials, with the parallel and series states as the upper and lower limit, respectively. In contrary, our measurement shows a negative slope relative to the SiNCs volume fraction. The decrease in the thermal conductivity indicates a significant increase in the overall phonon scattering in the nanocomposite material.

Additionally, although the models considered the dispersion state, volume fraction, filler size and filler shape, other factors such as the boundary effect between the matrix and filler, and the contact resistance at closely attached fillers were not considered in predicting the thermal conductivity. These models are commonly used for composite materials, which typically have filler size on the micrometer scale, thereby neglecting the nano-size effects. In nanoscale composite materials, the fillers have a large surface-volume ratio that significantly influences the thermal conductivity [13] and must be taken into account in thermal conductivity models. This is the principal reason why the SiNC/PS nanocomposite does not follow the conventional prediction model shown in Figure 2-10.

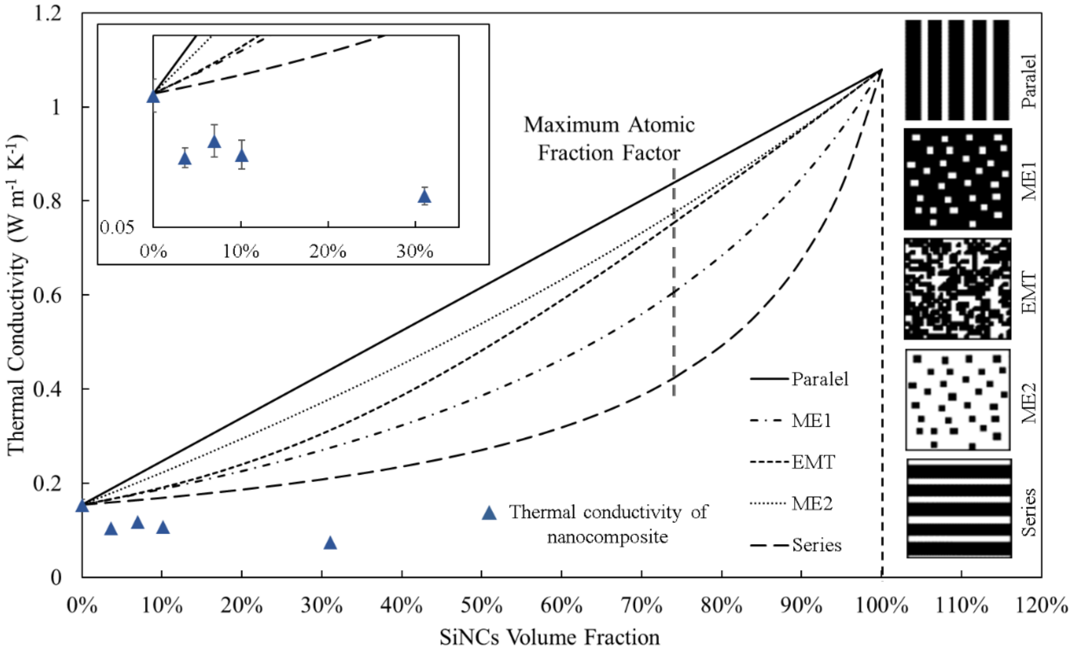

Figure 2-10. Measured thermal conductivity vs. SiNCs volume fraction compared with five fundamental thermal conductivity models [43] for composite materials

Furthermore, Kihara et al. reported thermal conductivity of 1.08 W m^{-1} K^{-1} for porous SiNCs with a smaller diameter (3 nm) with 55% porosity [42]. Additionally, it was reported that the lowest limit of the thermal conductivity of silicon-based materials would be 1–2.5 W m^{-1} K^{-1} in the case of amorphous silicon [45], [46]. It was also recently reported that the thermal conductivity of a c-Si/a-Si combination structure had reached 0.78 W m^{-1} K^{-1}[47], which indicates firmly that the thermal conductivity of SiNCs should not be lower than that of PS.

As mentioned earlier, in nanocomposite materials, the phonon transport and heat conduction at the nanoscale are different from those at the macroscale because of several factors. First, with a significantly smaller particle size of the SiNCs, there is a significant increase in the surface interface between the PS as a matrix and the SiNCs as filler. The significant increase in the surface to volume ratio leads to an increased phonon scattering effect at the material interfaces, which act as thermal resistance.

Second, when the crystal grain size became smaller than the mean free path (MFP; Λ), the thermal conductivity decreased significantly. The phonon MFP is the average distance traveled by a phonon between collisions with another phonon. The phonon MFP in silicon thin films at room temperature has been reported as approximately 300 nm [48], [49], and the important phonon wavelength for heat transfer in silicon was reported as approximately 1~10 nm [13]. The Debye principle explains that the heat transport mechanism by phonon transport can be resolved into traveling waves that carry heat, so that the thermal conductivity is expressed as [13], [50], [51]:

$$\kappa = \frac{1}{3} C v \Lambda \tag{2-49}$$

where C is the specific heat per unit volume, v is the sound velocity in the material, and Λ is the finite mean free path of the phonon. Assuming a perfect crystal solid material, at very low temperatures, the MFP is rather long due to a small amount of phonons, and k is proportional to C and mainly determined by C . However, at higher temperatures (including room temperature), k is mainly dependent on the MFP; therefore, when the phonon density increases significantly, the phonon-phonon scattering also increases.

In the Debye principle mentioned above, it was assumed that the crystal size is infinite or large enough so the MFP is determined mainly by phonon-phonon scattering. In a macroscale crystal, with a large crystal size, the effect of the grain boundaries on the thermal conductivity can only occur at very low temperatures, where the phonon MFP is comparable to the crystal grain size. However, at room temperature, the phonon MFP is much smaller than the macroscale crystal size. In this work, the SiNCs' grain size (below 10nm) is significantly smaller than the phonon MFP in silicon at room temperature (300 nm). When the grain size (L) is smaller than the MFP (Λ), the phonon MFP will be limited by the grain boundary, and the thermal conductivity can be written as [49]:

$$\kappa \propto CvL \tag{2-50}$$

where $L < \Lambda$. Unlike the MFP, the equation above is independent of the phonon frequency and determined only by geometrical properties of the crystal particle. This phonon-boundary scattering has been investigated for the reduction in the thermal conductivity of multi-phase structured materials [13], [49], [52].

Lastly, the phonon dispersion changed due to the comparable size of the crystal and the phonon wavelength. Generally, phonon dispersion in semiconductor materials involves optical and acoustic phonons. Acoustic phonons have frequencies that approach zero when the phonon wave vector approaches zero. They have a relatively larger group velocity than optical phonons, and heat is mainly carried by acoustic phonons [49]. When the particle grain size is much smaller than the MFP and comparable to the phonon wavelength, the boundary condition periodic vibration assumption no longer works in describing the dispersion behavior of acoustic phonons. Balandin et al. have investigated the phonon dispersion behavior at a specific boundary condition in the case of the superlattice or nanowire. It was reported that several branches of acoustic phonons experienced a spatial confinement effect, where they transformed to optical phonon-like branches that do not contribute to heat transfer [49]. Our SiNCs have a grain size below 10 nm that is much lower than MFP (300 nm) and is relatively comparable to the phonon wavelength in silicon at room temperature. The phonon dispersion modification effect may also contribute in reducing the thermal conductivity of the nanocomposite although this requires further analysis and observation.

2.6. Conclusion

We have produced SiNCs/PS nanocomposite thin films and measured their density, specific heat and thermal diffusivity to determine their thermal conductivity. Nanocomposite fabrication utilizing silicon inks enables room temperature processing. It preserves an initial crystal size of less than 10 nm; this enables the use of the nanocomposite in a wide range of inexpensive applications while maintaining the unique properties of silicon nanoparticles. Compared with results from the empirical model of thermal conductivity for composite materials, our measurements show a negative slope and decreasing thermal conductivity in the presence of SiNCs. The nanostructured SiNCs/polymer composite may be a solution for various applications that require a silicon-based low-thermal conductivity material. The increased phonon scattering at the SiNCs/PS boundaries plays a major role in heat conduction in the SiNCs/PS composite; meanwhile, phonon scattering and/or confinement within individual SiNCs is not well understood. For future work, further analysis of thermal transport in nanocomposite using different lattice structure, such as amorphous Si nanoparticles would enable a comprehensive understanding for deeper insight into the phonon transport mechanism in nanocomposite (< 10 nm) materials.

2.7. References

[1] S. Zhao, X. Pi, C. Mercier, Z. Yuan, B. Sun, and D. Yang, “Silicon-nanocrystal-incorporated ternary hybrid solar cells,” *Nano Energy*, vol. 26, pp. 305–312, 2016.

[2] Z. Deng, X. D. Pi, J. J. Zhao, and D. Yang, “Photoluminescence from Silicon Nanocrystals in Encapsulating Materials,” *J. Mater. Sci. Technol.*, vol. 29, no. 3, pp. 221–224, 2013.

[3] M. B. Jakubinek, M. A. White, M. Mu, and K. I. Winey, “Temperature dependence of thermal conductivity enhancement in single-walled carbon nanotube/polystyrene composites,” *Appl. Phys. Lett.*, vol. 96, no. 8, pp. 94–97, Feb. 2010.

[4] Y. Yang, M. C. Gupta, J. N. Zalameda, and W. P. Winfree, “Dispersion behaviour, thermal and electrical conductivities of carbon nanotube-polystyrene nanocomposites,” *Micro Nano Lett.*, vol. 3, no. 2, p. 35, 2008.

[5] Z. Han and A. Fina, “Thermal conductivity of carbon nanotubes and their polymer nanocomposites: A review,” *Prog. Polym. Sci.*, vol. 36, no. 7, pp. 914–944, Jul. 2011.

[6] V. Lysenko, S. Périchon, B. Remaki, and D. Barbier, “Thermal isolation in microsystems with porous silicon,” *Sensors Actuators, A Phys.*, vol. 99, no. 1–2, pp. 13–24, 2002.

[7] L. Pavesi and R. Turan, *Silicon Nanocrystals*. Weinheim, Germany: Wiley-VCH Verlag GmbH & Co. KGaA, 2010.

[8] R. Gresback, T. Nozaki, and K. Okazaki, “Synthesis and oxidation of luminescent silicon nanocrystals from silicon tetrachloride by very high frequency nonthermal plasma.,” *Nanotechnology*, vol. 22, no. 30, p. 305605, Jul. 2011.

[9] L. Mangolini, “Synthesis, properties, and applications of silicon nanocrystals,” *J. Vac. Sci. Technol. B Microelectron. Nanom. Struct.*, vol. 31, no. 2, p. 020801, 2013.

[10] L. Mangolini, E. Thimsen, and U. Kortshagen, “High-yield plasma synthesis of luminescent silicon nanocrystals,” *Nano Lett.*, vol. 5, no. 4, pp. 655–659, Apr. 2005.

[11] Y. Ding, M. Sugaya, Q. Liu, S. Zhou, and T. Nozaki, “Oxygen passivation of silicon nanocrystals : In fl uences on trap states , electron mobility , and hybrid solar cell performance,” *Nano Energy*, vol. 10, pp. 322–328, 2014.

[12] B. F. P. McVey and R. D. Tilley, “Solution synthesis, optical properties, and bioimaging applications of silicon nanocrystals.,” *Acc. Chem. Res.*, vol. 47, no. 10, pp. 3045–51, Oct. 2014.

[13] Z. Wang, J. E. Alaniz, W. Jang, J. E. Garay, and C. Dames, “Thermal conductivity of nanocrystalline silicon: Importance of grain size and frequency-dependent mean free paths,” *Nano Lett.*, vol. 11, no. 6, pp. 2206–2213, Jun. 2011.

[14] J. Morikawa, C. Leong, T. Hashimoto, T. Ogawa, Y. Urata, S. Wada, M. Higuchi, and J. I. Takahashi, “Thermal conductivity/diffusivity of Nd3+ doped GdVO4, YVO4, LuVO4, and Y3Al5O 12 by temperature wave analysis,” *J. Appl. Phys.*, vol. 103, no. 6, p. 063522, 2008.

[15] J. Morikawa and T. Hashimoto, “Thermal diffusivity of aromatic polyimide thin films by temperature wave analysis,” *J. Appl. Phys.*, vol. 105, no. 11, 2009.

[16] F. Takahashi, K. Ito, J. Morikawa, T. Hashimoto, and I. Hatta, “Characterization of Heat Conduction in a Polymer Film,” *Jpn. J. Appl. Phys.*, vol. 43, no. 10, pp. 7200–7204, Oct. 2004.

[17] T. Kurihara, J. Morikawa, and T. Hashimoto, “Measurement of the thermal diffusivity of thin films by an AC joule-heating method,” *Int. J. Thermophys.*, vol. 18, no. 2, pp. 505–513, Mar. 1997.

[18] J. Morikawa and T. Hashimoto, “Thermal diffusivity measurement of low-k dielectric thin film by temperature wave analysis,” *Thermochim. Acta*, vol. 432, no. 2, pp. 216–221, Jul. 2005.

[19] J. Morikawa and T. Hashimoto, “Study on thermal diffusivity of poly(ethylene terephthalate) and poly(ethylene naphthalate),” *Polymer (Guildf).*, vol. 38, no. 21, pp. 5397–5400, 1997.

[20] A. Maesono, Y. Takasaki, Y. Maeda, R. Tye, J. Morikawa, and T. Hashimoto, “A new apparatus for thermal diffusivity and specific heat measurements of films and liquids by

means of Fourier transform thermal analysis," *High Temp. Press.*, vol. 34, no. 2, pp. 127–134, 2002.

[21] W. D. Jung, J. Morikawa, and T. Hashimoto, "Thermal diffusivity measurement of polyamide mesh by temperature wave analysis," *Int. J. Thermophys.*, vol. 21, no. 2, pp. 503–512, 2000.

[22] J. Morikawa and T. Hashimoto, "Thermal diffusivity measurement of papers by an ac Joule heating method," *Polym. Int.*, vol. 45, no. 2, pp. 207–210, 2002.

[23] T. Hashimoto and T. Tsuji, "Thermal diffusivity measurement of polyethylene melt by a new temperature wave method," *J. Therm. Anal.*, vol. 40, no. 2, pp. 721–726, 1993.

[24] W. D. Jung, J. Morikawa, and T. Hashimoto, "Thermophysical properties of poly(propylene)-based composite polymer," *J. Therm. Anal. Calorim.*, vol. 64, no. 2, pp. 509–519, 2001.

[25] T. Hashimoto, J. Morikawa, T. Kurihara, and T. Tsuji, "Frequency dependent thermal diffusivity of polymers by temperature wave analysis," *Thermochim. Acta*, vol. 304–305, pp. 151–156, Nov. 1997.

[26] J. Morikawa, T. Hashimoto, and A. Maesono, "Simultaneous measurement of thermal diffusivity, heat capacity, and thermal conductivity by Fourier transform thermal analysis," *High Temp. Press.*, vol. 33, no. 4, pp. 387–395, 2001.

[27] J. Morikawa, T. Kurihara, T. Hashimoto, and G. Sherbelis, "Thermal diffusivity of thermosetting materials by temperature-wave analysis," *Thermochim. Acta*, vol. 299, no. 1–2, pp. 95–100, Sep. 1997.

[28] Y. Ding, R. Yamada, R. Gresback, S. Zhou, X. Pi, and T. Nozaki, "A parametric study of non-thermal plasma synthesis of silicon nanoparticles from a chlorinated precursor," *J. Phys. D. Appl. Phys.*, vol. 47, no. 48, p. 485202, 2014.

[29] T. Nozaki, Y. Ding, and R. Gresback, "Plasma Synthesis of Silicon Nanocrystals: Application to Organic/Inorganic Photovoltaics through Solution Processing," *Mater. Sci. Forum*, vol. 783–786, pp. 2002–2004, May 2014.

[30] Y. Ding, R. Gresback, R. Yamada, K. Okazaki, and T. Nozaki, "Hybrid Silicon Nanocrystal/Poly(3-hexylthiophene-2,5-diyl) Solar Cells from a Chlorinated Silicon Precursor," *Jpn. J. Appl. Phys.*, vol. 52, no. 11S, p. 11NM04, Nov. 2013.

[31] Y. Ding, R. Gresback, Q. Liu, S. Zhou, X. Pi, and T. Nozaki, "Silicon nanocrystal conjugated polymer hybrid solar cells with improved performance," *Nano Energy*, vol. 9, pp. 25–31, 2014.

[32] B. Ellis and R. Smith, *Polymers: A Property Database*, vol. 2, no. 2. 2008.

[33] R. L. Puurunen, H. Kattelus, and T. Suntola, *Chapter 26 - Atomic Layer Deposition in MEMS Technology*. Elsevier, 2010.

[34] I. Doğan and M. C. M. van de Sanden, "Direct characterization of nanocrystal size distribution using Raman spectroscopy," *J. Appl. Phys.*, vol. 114, no. 13, p. 134310, 2013.

[35] I. Doğan, N. J. Kramer, R. H. J. Westermann, K. Dohnalová, A. H. M. Smets, M. A. Verheijen, T. Gregorkiewicz, and M. C. M. Van De Sanden, "Ultrahigh throughput plasma

processing of free standing silicon nanocrystals with lognormal size distribution," *J. Appl. Phys.*, vol. 113, no. 13, p. 134306, 2013.

[36] K. H. Khoo, A. T. Zayak, H. Kwak, and J. R. Chelikowsky, "First-Principles Study of Confinement Effects on the Raman Spectra of Si Nanocrystals," *Phys. Rev. Lett.*, vol. 105, no. 11, p. 115504, Sep. 2010.

[37] C. Ossadnik, S. Veprek, and I. Gregora, "Applicability of Raman scattering for the characterization of nanocrystalline silicon," *Thin Solid Films*, vol. 337, no. 1–2, pp. 148–151, Jan. 1999.

[38] T. Nozaki, K. Sasaki, T. Ogino, D. Asahi, and K. Okazaki, "Microplasma synthesis of tunable photoluminescent silicon nanocrystals," *Nanotechnology*, vol. 18, no. 23, p. 235603, Jun. 2007.

[39] M. J. Kim and X. S. Sun, "Correlation between Physical Properties and Shear Adhesion Strength of Enzymatically Modified Soy Protein-Based Adhesives," *J. Am. Oil Chem. Soc.*, vol. 92, no. 11–12, pp. 1689–1700, Dec. 2015.

[40] D. V. Tsu, G. Lucovsky, and B. N. Davidson, "Effects of the nearest neighbors and the alloy matrix on SiH stretching vibrations in the amorphous SiOr:H (0<r<2) alloy system," *Phys. Rev. B*, vol. 40, no. 3, pp. 1795–1805, Jul. 1989.

[41] D. R. McKenzie, "Infrared absorption and bonding in amorphous hydrogenated silicon-carbon alloys," *J. Phys. D. Appl. Phys.*, vol. 18, no. 9, pp. 1935–1948, 1985.

[42] T. Kihara, T. Harada, and N. Koshida, "Precise thermal characterization of confined nanocrystalline silicon by 3ω method," *Japanese J. Appl. Physics, Part 1 Regul. Pap. Short Notes Rev. Pap.*, vol. 44, no. 6 A, pp. 4084–4087, Jun. 2005.

[43] J. Wang, J. K. Carson, M. F. North, and D. J. Cleland, "A new structural model of effective thermal conductivity for heterogeneous materials with co-continuous phases," *Int. J. Heat Mass Transf.*, vol. 51, no. 9–10, pp. 2389–2397, May 2008.

[44] J. C. Maxwell, "A treatise on electricity and magnetism | Vol. 1," *Clarendon Press*, vol. 1. 1873.

[45] D. G. Cahill, S. K. Watson, and R. O. Pohl, "Lower limit to the thermal conductivity of disordered crystals," *Phys. Rev. B*, vol. 46, no. 10, pp. 6131–6140, Sep. 1992.

[46] D. Cahill, A. Bullen, and S.-M. Lee, "Interface thermal conductance and the thermal conductivity of multilayer thin films," *High Temp. Press.*, vol. 32, no. 2, pp. 135–142, 2000.

[47] Y. Nakamura *et al.*, "Anomalous reduction of thermal conductivity in coherent nanocrystal architecture for silicon thermoelectric material," *Nano Energy*, vol. 12, pp. 845–851, Mar. 2015.

[48] Y. S. Ju and K. E. Goodson, "Phonon scattering in silicon films with thickness of order 100 nm," *Appl. Phys. Lett.*, vol. 74, no. 20, p. 3005, May 1999.

[49] A. A. Balandin, "Nanoscale Thermal Management," *Ieee Potentials*, no. March, pp. 11–15, 2002.

[50] M. I. Flik, B. I. Choi, and K. E. Goodson, "Heat Transfer Regimes in Microstructures," *J. Heat Transfer*, vol. 114, no. 3, p. 666, Aug. 1992.

[51] D. P. D. Bergman, Theodore L, Adrienne S. Lavine, Frank P. Incropera, *Introduction to Heat Transfer*, vol. XXXIII, no. 2. 2014.

[52] A. Balandin, “Thermal properties of semiconductor low-dimensional structures,” *Phys. Low-Dim. Struct.*, vol. 1/2, no. 1, pp. 1–28, 2000.

Chapter 3: Thermal Boundary Resistance and Heat Transfer at Material Interface

This chapter is an adaptation of the published works:

1. Firman Bagja Juangsa, Yoshiki Muroya, Meguya Ryu, Junko Morikawa, Tomohiro Nozaki, (2017). Comparative study of thermal conductivity in crystalline and amorphous nanocomposite. *Applied Physics Letters*, 110(25), 253105. https://doi.org/10.1063/1.4986920
2. Firman Bagja Juangsa, Meguya Ryu, Junko Morikawa, Tomohiro Nozaki, (2018). Nonthermal plasma synthesis of silicon nanoparticles and their thermal transport properties. *J Phys D Appl Phys*. 51(50):505301. https:// doi.org/10.1088/1361-6463

3.1. Abstract

Silicon nanocrystals (SiNCs)/Polystyrene (PS) nanocomposite has been observed to have a significant decrease in thermal conductivity in terms of the SiNCs fraction with unspecified factors remained unclear. In this section, amorphous silicon nanoparticles (a-SiNPs) with a mean diameter of 6 nm and PS nanocomposites were synthesized, and their thermal conductivity, including the density and specific heat, was compared with our previous work which investigated well-crystalized SiNPs (6 nm) and PS nanocomposite. The difference between amorphous and crystalline structure is insignificant, but phonon scattering at SiNPs and PS boundary is the key influencing factor of thermal conductivity reduction. The effective thermal conductivity models for nanocomposite revealed that the thermal boundary resistance (TBR), explained by Kapitza principle, is estimated to be 4×10^{-7} m^{2}K/W, showing the significant effect of nanostructured heterogenic surface resistance on overall heat transfer behavior. Further treatment by post-processing of thermal annealing was

applied, and thermal conductivity measurement result shows the increase of thermal conductivity values. Although there is no significant enhancement of SiNPs dispersion in the PS matrix, thermal annealing induced molecular structure change, resulting in thermal transport enhancement at the interfacial region. Preservation of unique properties nanoscale materials and low-cost fabrication by silicon inks process at room temperature give the promising potential of the SiNPs-based nanostructured material, and the combination of interfacial region engineering and post-processing provides controllable thermal transport properties for application in heat transfer management.

3.2. Introduction

Heterogeneous materials have been extensively studied for promising application in optical, electronics, and thermal management fields, as well as potential to provide low cost and bulk scale device fabrication [1]–[3]. Nanoscale heterogeneous structured material or nanostructured material introduced additional advantages of nanoscale material that improved device performance, such as reported for photovoltaic (PV) [4] and thermoelectric [5]–[7]. Of particular, there has been growing interest in thermal transport in nanostructured materials as the basic principle of thermoelectric materials for refrigeration and energy harvesting.

Silicon nanocrystal (SiNCs) as one of well-known nanoscale material has been researched for its size dependence thermal properties, where the experimental result has been reported with a significant decrease of thermal conductivity as silicon particles size is reduced [8]–[11]. In this work, we produced hybrid nanostructured materials of silicon nanoparticles (inorganic) and organic polymers. The process is carried out at room temperature that preserves the nanometer particle mean diameter and narrow size distribution. We have previously reported the silicon nanocrystals (SiNCs)/polystyrene nanocomposite thermal conductivity, and the result showed a significant decrease of effective thermal conductivity with the presence of SiNCs despite the higher thermal conductivity compared with the polymer matrix [6]. This unique controllable thermal property of SiNCs and its effect on nanocomposite thermal transport mechanism gives the promising potential for thermal management, especially for electronic devices that have silicon as the main material.

In the previous chapter, it has been analyzed that the phonon transport decrease can be caused by significant increase phonon scattering at boundaries, nanostructured polymer networks, and phonon transport suppression due to nano size characteristic length. In order to distinguish one factor from another, additional analysis is required for further observation.

In this chapter, amorphous silicon is employed as nanoparticle in nanocomposite and measured for thermal conductivity by thermal wave analysis (TWA), which based on the phase shift of temperature wave between two surfaces of the sample [12]. Among amorphous materials, amorphous silicon is one of the most widely used as semiconductor materials due to its excellent electronic and optical properties and low-cost potential [13]–[15]. Regarding thermal transport, lattice vibration plays a major role in the amorphous semiconductor material, such as a-SiNPs [14], [15]. Due to lack of translational symmetry and periodicity over a long distance, the term “phonon” in amorphous material refers to lattice vibration that cannot be quantized. Consequently, the phonon waves concept, group velocity, and mean free path (MFP) are not fully applicable. However, those concepts can be partly used to simplify the thermal transport in amorphous silicon. By comparing the thermal conductivity of a-SiNPs and SiNCs in nanocomposite material, the major cause of thermal transport suppression was analyzed.

Furthermore, additional analysis of thermal transport in nanocomposite film was carried out by observing post-processing thermal annealing. Post-processing annealing effect on thermal transport is evaluated with regards to nanocomposite structure, the interfacial interaction between filler and matrix, and molecular crystallinity of each substance.

Finally, as nanocomposite structures have a significantly high ratio of interfaces to volume, modeling the thermal transport is also a challenging topic. In the previous chapter, thermal conductivity models for two-phase material were used for modeling, and it was observed that the experimental result did not agree with the model because conventional macroscopic models do not consider the effect of thermal boundary resistance. In this chapter, several modified thermal conductivity models for nanocomposite were reviewed and applied with the consideration of thermal boundary resistance that plays a major role in nanocomposite thermal transport.

3.3. Experiment Method and Condition

Silicon nanoparticles (SiNPs) were synthesized by nonthermal plasma CVD method [6], [16]. This method allows controllable amorphous-crystalline fraction by adjusting the input power of plasma [16]. Amorphous SiNPs were synthesized by the same reactor employed for SiNCs, by decreasing the input power to 30 W. The synthesize apparatus has a quartz tube reactor with an inner diameter of 45 mm equipped with two copper as the electrodes on the tube. Very high frequency (VHF) of 70 MHz power source is supplied to the reactor to generate the plasma. SiNPs were synthesized from $SiCl_4$, H_2, and Ar with a volumetric ratio of 1:20:30 respectively, maintaining the reactor pressure at around 400 Pa. SiNPs surface termination was treated by dry etched by hydrofluoric acid vapor (HF) so that SiNPs is mostly terminated by hydrogen[6].

Similar to the process explained in the previous chapter, the nanocomposite of a-SiNPs and polystyrene were produced by the solution process [6]. Atactic polystyrene (Sigma-Aldrich 430102) with average molecular weight ca. 192,000 was used for this work. The a-SiNPs and PS were dispersed in benzonitrile (anhydrous, Sigma-Aldrich 294098) with predetermined concentrations, as shown in Table 3-1. The volume fraction of each sample was determined based on the density reference values of amorphous silicon and PS (2.29 g/cm^3 and 1.05 g/cm^3, respectively) [17], [18]. The mixed solution of the a-SiNPs and PS was stirred for 24 hours to obtain a stable, well-dispersed solution, before deposited on the substrate to produce thin film sample. The thin film sample was dried in a vacuum chamber (<1 Pa) for 12 hours, in order to avoid gas trapped within the sample and to evaporate the remaining solvent.

Extensive material characterizations were employed to identify the characteristics of the nanocomposite thin film sample. The amorphous fraction of SiNPs was analyzed by Raman Spectroscopy (STR750 Laser Raman Spectrometer; Seki Technotron Corp.), and the thin film thickness was measured by profilometer or micro figure measuring instrument (Kosaka Lab, Surfcorder ET200).

Table 3-1. a-SiNPs/PS Nanocomposite Experimental Condition

No	SiNPs concentration (mg/cm^3)	PS concentration (mg/cm^3)	SiNPs Mass Fraction (%)	SiNPs Volume Fraction (%)	Sample Thickness Average	
					(μm)	Error (μm)
1	0	300	0	0	11.99	0.06
2	25	300	7.7	3.7	4.58	0.11
3	50	300	14.3	7.1	5.14	0.22
4	75	300	20	10.3	5.92	0.19
5	75	150	33.3	18.7	4.05	0.29
6	75	100	43	25.6	2.32	0.09

The thermal properties analysis methods are similar to that of SiNCs based nanocomposite explained in the previous chapter. Thermal conductivity was determined based on measurement of thermal diffusivity, specific heat, and mass density by temperature wave analysis (TWA), differential scanning calorimeter (DSC) (Perkin-Elmer DSC-7), and electronic densimeter (Alfamirage SD-200L), respectively, based on the following equation,

$$\kappa = \alpha \rho c_p \tag{3-1}$$

Post-processing of thermal annealing on nanocomposite thin film was also carried out in N_2 atmosphere glove box (<0.1 ppm oxygen and water, MIWA). Each sample was annealed on a hot plate at 150°C for 12 hours. Thermal annealing is done at a temperature well above the glass transition temperature (T_g) of the polymer matrix, which is 100°C for most of amorphous PS [18].

Additional analysis of thermal annealing temperature effect on SiNPs was carried out by electron spin resonance (ESR, JEOL JES-FA100), measuring atomic defect of SiNPs. SiNPs powder was annealed in H_2 atmosphere at atmospheric pressure. The same amount of SiNPs powder was measured to compare the relative amount of defect, which is represented by the ESR signal. SiNPs with higher annealing temperature (150, 200, and 250°C) were characterized by ESR spectroscopy. SiNPs powder was placed into ESR sample tubes, which is prepared in a N_2 atmosphere glove box.

Thermal annealing was applied to the nanocomposite samples of both SiNCs and a-SiNPs, which have been measured for their thermal conductivity values. Group of samples with minimum standard deviation were selected for thermal annealing process, to observe the thermal transport characteristic change represented by thermal conductivity. Based on the thermal conductivity measurement data, nanocomposite samples with the SiNPs volume fraction of 2.2%, 3.6%, 5.7%, 18.7%, and 31.1% were selected for thermal annealing.

Material characterizations after thermal annealing treatment were carried out by Raman Spectroscopy, and FTIR Spectroscopy (FT/IR-6100; JASCO Corp.). Raman Spectroscopy is equipped with a laser wavelength of 532 nm, and measurement condition of 20 × 10 s exposure time, ×100 objective lens and excitation power of 1.3 mW. Minimum excitation power with multiple accumulations was selected in order to minimize the effect of heating on the Raman shift peaks. FTIR with attenuated total reflection (ATR) module was employed in this work. ATR is known ideal for solid film sample, allows the direct measurement on the thin film sample deposited on the glass substrate. Multi-reflector ATR (ATR PRO410-M) with ZnSe prism was used, giving the measurement range above 550 cm^{-1}. Additionally, the thin film was characterized using a transmission electron microscope (TEM, JEM-2010F) to observe the dispersion condition of SiNPs in the nanocomposite sample. The effect of post-process thermal annealing treatment on thermal conductivity of nanocomposite was by TWA measurements, where the thermal conductivity (κ), which represent the thermal transport property of the material, is determined based on equation (2-43).

3.4. Comparison of Thermal Conductivity in Crystalline and Amorphous Nanocomposite

3.4.1. Amorphous Silicon Characterization

Raman spectra for SiNPs synthesized using different amounts of input power are presented in Figure 3-1. The spectra were then deconvoluted into two components with peaks intensity at 480 cm^{-1} (amorphous) and 520 cm^{-1} (crystalline). Raman shift as a result of Raman spectroscopy, refers to the energy difference between an incoming photon and exited photon from a substance. In crystalline materials such as SiNCs, incoming photon excites a lattice vibration (phonon) with zero momentum according to the momentum conservation law. The momentum conservation law only allows certain energy level of phonon, producing narrow and sharp peat of Raman shift at 520 cm^{-1}. In the amorphous structure of silicon, the momentum selection is relaxed, which produces a variety of phonon modes. As a result, a broad peak centered at 480 cm^{-1} is displayed, representing the amorphous structure of silicon.As also mentioned in the previous chapter, SiNCs peak shifted from the bulk Si at 520 cm^{-1} to a lower wavenumber due to the phonon confinement effect, as was observed theoretically and experimentally for nanocrystals smaller than 20 nm [19]–[21]

Amorphous silicon spectrum, which is synthesized by low input power (30 W) shows a considerably negligible fraction of crystalline silicon compared to the SiNCs. This is due to the low amount of plasma input power that caused insufficient plasma heating effect during synthesize process. The same method has been reported that the amorphous SiNPs are crystallized as the input power increases with an insignificant change of particles size [22].

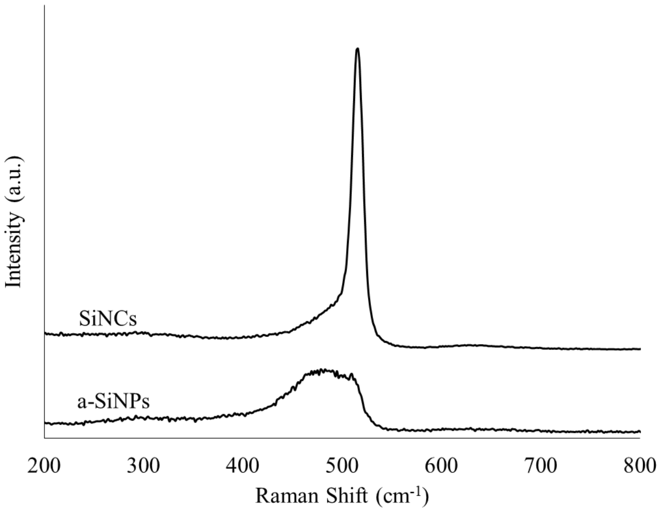

Figure 3-1 Raman spectra of amorphous silicon nanoparticles (a-SiNPs) compared with silicon nanocrystals (SiNCs)

3.4.2. Thermal Conductivity

Mass density and specific heat were determined experimentally by DSC (Perkin-Elmer DSC-7), and electronic densimeter (Alfamirage SD-200L). For measurement validation, the results were compared with calculation based on the reference values of both a-Si (2.29 g/cm^3, 680.17 J/kg.K) and PS (1.05 g/cm3, 1275 J/kg.K) [17], [18], [23]. Figure 3-2 (a) and (b) shows measurement result of specific heat and density, respectively, and their comparison with reference values. The results show the measurement result of density and specific heat have good agreement with the calculation result of the reference value. In term of specific heat, Kihara et al. reported that the surface oxidation of porous silicon has a result of increasing the heat capacity per unit volume, due to changes of density and specific heat [9]. It is important to be noted from the result that without a significant increase of both density and specific heat confirmed, oxidation was successfully prevented, as well reported for similar process on crystalline silicon [6].

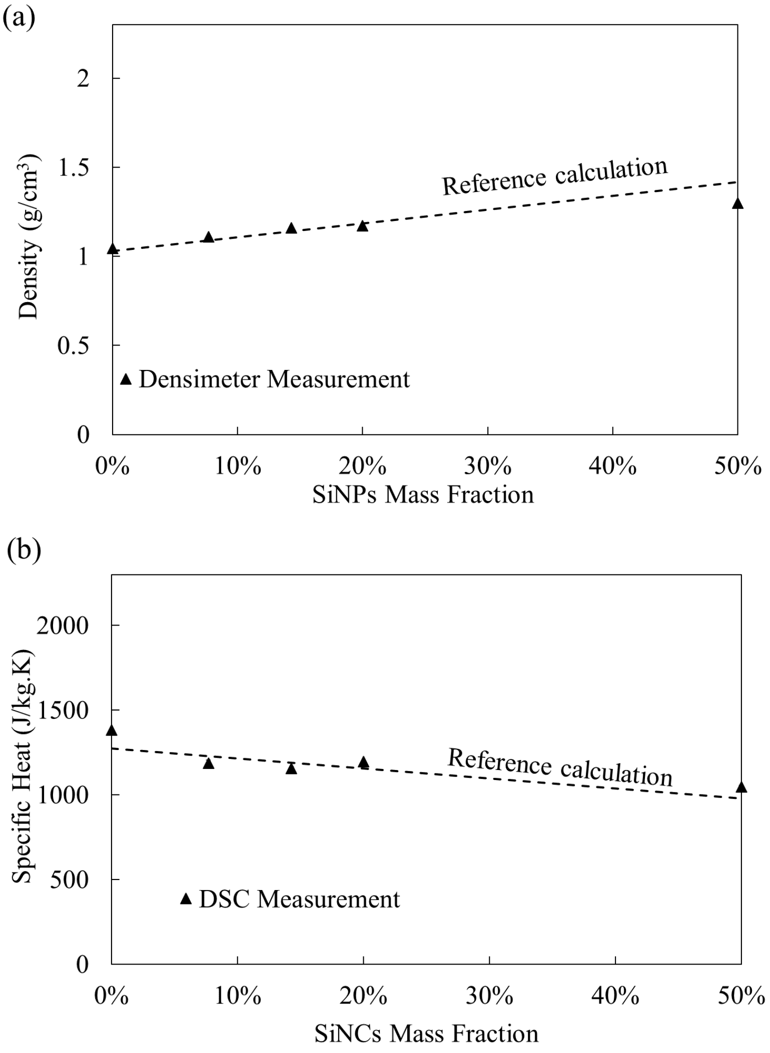

Figure 3-2 Measurement results of (a) Specific heat and (b) Mass density compared with the calculation data based on the reference value of SiNCs and PS

According to equation (2-43), thermal conductivity κ is determined based on thermal diffusivity α, specific heat c_p, and mass density ρ. Figure 3-3 shows the thermal conductivity of a-SiNPs/PS nanocomposite compared with previously reported SiNCs/PS nanocomposite [6]. The result shows that the thermal conductivity of a-SiNPs/PS nanocomposite decrease with increasing value of SiNPs fraction with an insignificant difference with its crystalline counterpart. The decrease of a-SiNPs/PS nanocomposite thermal conductivity indicates a significant increase of overall phonon scattering rate in the nanocomposite, as was also observed in SiNCs/PS nanocomposites. The identical thermal conductivity result of amorphous and crystalline fraction in nanocomposite confirms that phonon scattering at interface boundary between filler and matrix plays a major role in thermal transport at nanocomposite, compared with phonon confinement effect at the inside of the crystalline structure of silicon.

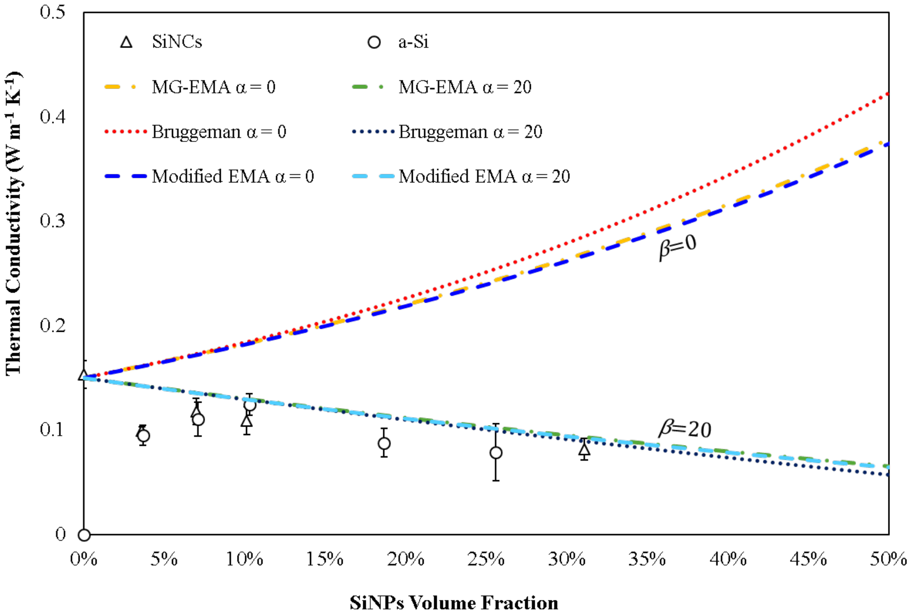

Figure 3-3 Thermal conductivity measurement results of a-SiNPs/PS and SiNCs/PS nanocomposites determined based on specific heat, mass density, and thermal diffusivity measurements, with the comparison with thermal conductivity models which include the effect of thermal boundary resistance

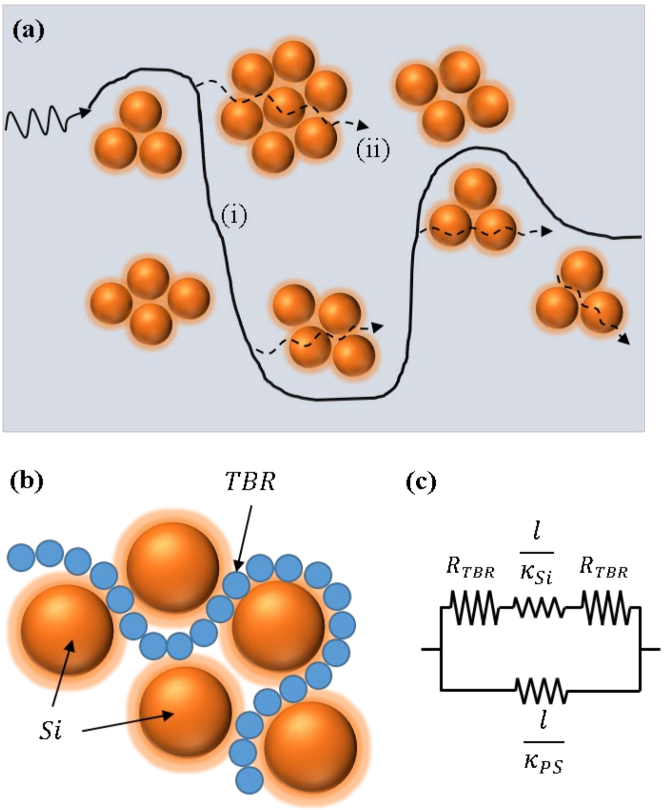

Figure 3-4 (a) Simplified phonon transport pathway in nanocomposite, mainly through the (i) PS network, and partially through (ii) SiNPs' aggregates due to the thermal boundary resistance created by surface hydrogen and PS complex thin layer as shown in (b) details schematic and (c) equivalent thermal circuit of phonon transport pathways.

Furthermore, the decrease in thermal conductivity can be analyzed based on the phonon transport pathway. As shown in the previous chapter, TEM images of SiNCs/PS nanocomposite show the aggregations of SiNCs, forming groups of SiNCs that are separated by the PS matrix. Phonon scattering at interface boundary induces the phonons to transport mainly through the PS matrix, as shown schematically in Figure 3-4(a). Large thermal resistance due to scattering at the boundary, allows an only small part of phonon going through the aggregated SiNPs, which include the PS networks among the SiNPs, as shown in Figure 3-4(b), creating longer phonon pathway and resulted in decreasing thermal conductivity. The equivalent thermal circuit was employed to provide the semi-quantitative analysis, based on the thermal resistance of each component, as shown in Figure 3-4(c). As the SiNPs fraction increase there are more SiNPs that create complex networks of PS matrix; leads to the negative slope of thermal conductivity with respect to the SiNPs fraction.

The phonon confinement effect, commonly referred as band folding effect, interference effect, or phonon dispersion modification is phenomena of significant phonon transport decrease due to the comparable or smaller size of material characteristic length than phonon wavelength [5], [24]–[26]. When it comes to this region, phonon cannot be treated as a particle and starts to be considered as wave nature. It was reported that critical phonon wavelength for thermal transport in silicon material at room temperature is around ~1-10 nm [26]–[28], and the SiNPs characteristic length (diameter) is around 6 nm [6], [22]. Although the SiNPs size is much smaller than phonon mean free path (MFP), which reduced the thermal conductivity of bulk silicon for two orders, it is not small enough to develop the phonon confinement effect due to the comparable ratio of phonon wavelength and surface roughness [26], [28]. In order to observe the phonon confinement effect, phonon wavelength shall be much longer than the characteristic length, which can be achieved in the low-temperature region.

3.4.3. Thermal Boundary Resistance (TBR)

Furthermore, the measurement results of nanocomposites were compared with thermal conductivity models that consider the thermal boundary resistance (TBR). After early investigation on the effective thermal conductivity of macroscopic heterogeneous materials by Maxwell [29], there are numerous research and models have been proposed to include TBR, which is particularly essential for thermal transport in nanoscale materials. Maxwell’s theory was modified by Hasselman and Johnson, and by Benvensite to include the TBR, called Maxwell-Garnet type Effective Medium Analysis (MG-EMA), as the following formula [30],

$$\frac{\kappa_c}{\kappa_m} = \frac{1 + 2\varphi(1-\beta)/(1+2\beta)}{1 - \varphi(1-\beta)/(1+2\beta)} \tag{3-2}$$

where κ_c is thermal conductivity of composite, κ_m is thermal conductivity of matrix, φ is the volume fraction of filler particles, and β is the dimensionless parameter representing the TBR. It is important to be noted that equation (3-2) has been derived for composite where the intrinsic thermal conductivity of filler particle is much greater than that of the matrix.

Based on MG-EMA, Every et al. also reported a model based Bruggeman's theory, which has been known as the most accurate model for higher volume fractions, while Maxwell's theory is rather suitable for low volume fraction [30]–[32]. Modified Bruggeman model with spherical filler is shown as following formula [30],

$$(1-\varphi)^3 = \left\{\frac{\kappa_m}{\kappa_c}\right\}^{\frac{(1+2\beta)}{(1-\beta)}} \left\{\frac{\kappa_c - \kappa_p(1-\beta)}{\kappa_m - \kappa_p(1-\beta)}\right\}^{\frac{3}{(1-\beta)}} \tag{3-3}$$

where it takes into account κ_p which is the thermal conductivity of filler particles.

In the later development, Minnich et al. modified the EMA model furthermore to be particularly suitable for nanocomposite, by introducing interface density that enhanced the effect of TBR in determining the effective thermal conductivity [33]. Interface density (Φ) was determined based on filler particles volume fraction (φ) and its' diameter (D) as the following formula,

$$\Phi = \frac{6\varphi}{D} \tag{3-4}$$

Interface density value was included in the calculation of effective thermal conductivity for both filler particles and matrix so that the thermal conductivity of composite is a function of interface density and the diameter of the particles as the following formula,

$$\kappa_m(\Phi, D) = \frac{1}{3} C_m v_m \frac{1}{\left(\frac{1}{\Lambda_m}\right) + \left(\frac{\Phi}{4}\right)}$$

$$\times \frac{\kappa_p(D)\big(1 + 2\beta(\Phi, D)\big) + 2\kappa_m(\Phi) + 2\left(\frac{\Phi D}{6}\right)\left[\kappa_p(d)\big(1 - \beta(\Phi, D)\big) - \kappa_m(\Phi)\right]}{\kappa_p(D)\big(1 + 2\beta(\Phi, D)\big) + 2\kappa_m(\Phi) - \left(\frac{\Phi D}{6}\right)\left[\kappa_p(d)\big(1 - \beta(\Phi, D)\big) - \kappa_m(\Phi)\right]} \tag{3-5}$$

where C_m, v_m, and $\Lambda_m$are volumetric specific heat, phonon group velocity, and phonon MFP for matrix, respectively. In this work, PS is used as matrix and the reference value for volumetric specific heat was used for calculation. Sound velocity in PS was used for phonon group velocity while phonon MFP was estimated by inverse calculation from the reference value of thermal conductivity, density, specific heat and sound velocity [18], [34].

All of these models have a common parameter of β, which is a dimensionless parameter depending on the TBR between filler and matrix. It is defined as $\beta = r_{\mathrm{TBR}}/(d/2)$, where $d = 6$ nm, which is SiNPs size and r_{TBR} is Kapitza radius representing the thermal resistance at the boundary of filler and matrix. Kapitza radius is defined as $r_{\mathrm{TBR}} = R_{TBR}\kappa_m$, where $R_{TBR}$is thermal resistance at the material interface, formed by the interaction between hydrogen and PS molecules, as shown schematically in of Figure 3-4(d). The minimum value of TBR ($\alpha = 0$) and the maximum value of TBR were calculated for each model. Devpura et al. utilized Biot number in order to determine the value of interface thermal resistant, with maximum Biot number of 10 [31], [35]. The Biot number for a particle of spherical shape is written as,

$$Bi = \frac{r_{\mathrm{TBR}}}{D} = \frac{1}{2}\beta \tag{3-6}$$

The thermal conductivity of well-defined bulk crystalline silicon (148 W m^{-1} K^{-1})[36], porous nanocrystalline silicon (3 nm, porosity 55%, 1.08 W m^{-1} K^{-1})[9], and PS (0.1549 W m^{-1} K^{-1})[18] were used for each model calculations, and they were compared with measurement result as shown in

Figure 3-4(a). It is important to be noted that the lowest limit of silicon would be 1~2.5 W m^{-1} K^{-1} in the case of amorphous silicon [37], [38]. The thermal conductivity of nanocrystalline silicon was used for MG-EMA and Bruggeman models, while modified EMA used bulk crystalline silicon due to phonon MFP calculation included within the model.

Figure 3-4(a) shows that, without TBR ($\beta = 0$), the effective thermal conductivity of all models increases with increasing value of SiNPs fraction simply because of the higher value of filler's thermal conductivity. On the other hand, models with maximum TBR ($\beta = 20$) shows decreasing the value of the effective thermal conductivity, and our measurement results of both a-Si and SiNCs show well match value with the thermal conductivity models.

We have analyzed the material characterization of nanocomposite by FT-IR Spectroscopy in the previous chapter. A slight shift of IR peaks was observed after nanocomposite fabrication, which is indicating a physical interaction between PS and SiNPs in molecular level [6], particularly on PS benzene ring and Si-H peaks. Physical interaction of polymer and its surrounding has been observed to have an effect on phonon transport [39]. This interaction produces the physical mismatch between characteristic frequencies for thermal vibration and intermolecular collision of two different materials [39], which supports our measurement result of decreasing thermal conductivity due to interaction at the interfacial boundary of SiNPs and PS.

Figure 3-5 shows the relationship between thermal conductivity and the dimensionless parameter α, represented with SiNPs fraction of 0, 50, and 74% (maximum hexagonal close packing filling factor [40]). Thermal conductivity decreases sharply from $\beta = 0$ to $\beta = 5$ and less than 0.1% decrease at $\beta = 20$. In this study, we assume that $\alpha = 20$ is the sufficiently large value describing significant thermal boundary resistance that represents experimental data semi-quantitatively. Based on the Kapitza radius formula, with $\alpha = 20$, thermal resistance was enhanced at least approximately to 4 × 10^{-7} m^2K/W. As shown in Figure 3-5, further increase of thermal resistance does not have a significant effect on the effective thermal conductivity. The thermal resistance of silicon and PS nanocomposite is greater than that of both silicon and PS composite with other materials, such as Si/SiO_2 (0.2~0.9 × 10^{-9} m^2K/W) [41], [42] and Sapphire/PS (0.4~1.4 × 10^{-7} m^2K/W) [43].

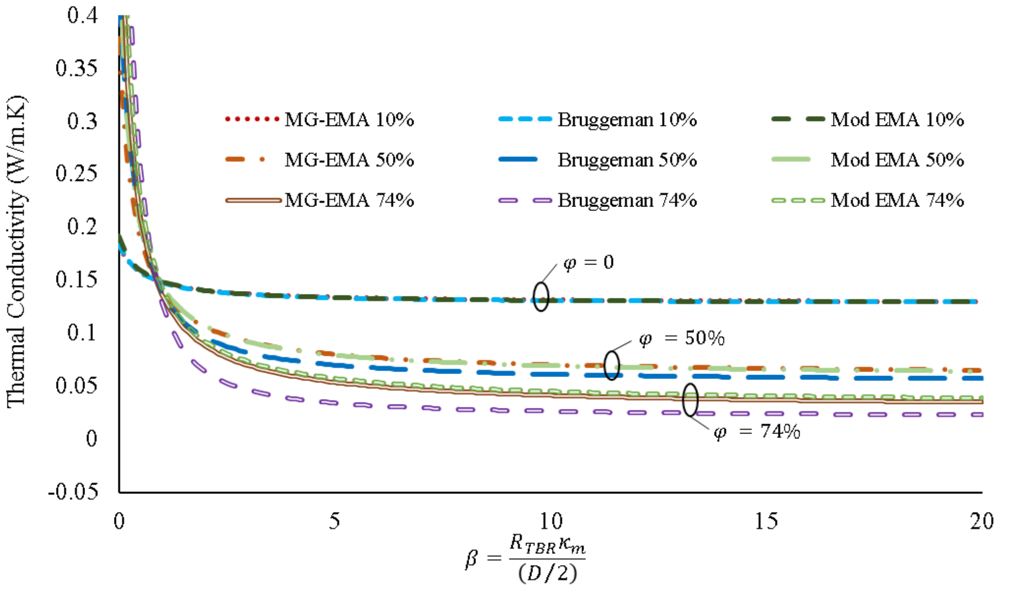

Figure 3-5. Calculation result of thermal conductivity models as the effect of dimensionless parameter β

Based on the above TBR estimation, the thermal circuit shown in Figure 3-4(d) can be calculated. The above-mentioned thermal conductivity of PS and nanocrystal silicon were used to calculate the thermal resistance, based on the equal length (l) of 6 nm. Thermal conductivity of bulk polymer was used, since phonon MFP of amorphous polymer is only a few angstroms [44]. Simple calculation confirmed phonon main pathway through PS network, as thermal resistance of a SiNC is 8.05 × 10^{-7} m^2K/W, 20 times greater than that of PS (4 × 10^{-8} m^2K/W).

Also, it is noted from the literature that all the models were developed for well-quantized phonon transport in crystalline materials based on phonon wave concept [30], [31], [33]; nevertheless, the measurement result shows amorphous organic polymer has a similar trend with the crystalline model. This result provides an intuitive understanding that the phonon wave concept can be analogously applied also on amorphous materials, such as PS. With thermal conductivity and volumetric specific heat is known and phonon group velocity is represented by sound velocity (v_c), quasi-MFP for amorphous material (Λ') can be simply determined according to the following formula [45],

$$\Lambda' = \frac{3\kappa}{Cv_c} \tag{3-7}$$

The above quasi-MFP calculation was applied on Modified EMA model in equation(3-5), which requires the phonon MFP of the matrix material. The Modified EMA model calculation result shows good agreement with other models and also our measurement result, indicating that the above quasi-MFP is acceptable. This result enables the extended application of nanostructured materials by improving the dispersion of SiNPs in the organic polymer matrix towards the periodic nanostructured, which has been well reported on superlattice and phononic crystal [26], [46]. Phonon interference effect has been reported to occur also in amorphous silicon (a-Si), especially for low-frequency phonon, which quasi-MFP is much longer than structure characteristic length [47]; consistent with applicable quasi-MFP we employed in this study.

However, one should note that, in high frequency, the MFP of the phonon in amorphous material reduces to a few nanometers, inducing the diffusive interfacial scattering, which makes the phonon interference effects negligible. As the lattice vibration (phonon) transport in amorphous and crystalline materials are fundamentally mechanism, the relevancy of quasi-MFP application in amorphous material is to be verified furthermore. Cryogenic measurements at very low temperature

(~4K) on both a-Si and SiNCs nanocomposites are expected to give a deeper understanding regarding the nanostructured material's phonon transport.

3.5. Post Processing Thermal Annealing Treatment Effect

Further analysis is applied on SiNPs/PS nanocomposite related to the effect of post-processing thermal annealing on the thermal properties of the nanocomposite. Thermal annealing on polymer nanocomposite has been reported to have a significant influence on spherical particle dispersion in the polymer matrix [48]. Chandran et al. reported a significant dispersion improvement of gold (Au) nanoparticle in PS by thermal annealing at 150°C. It is described that the annealing temperature plays an important role, as the dispersion of the nanoparticles is complete when annealed above bulk T_g. Furthermore, the interfacial interaction between particle and matrix is also critical for uniform dispersion of nanocomposite. Surface modification of nanoparticle has been widely known as one of the methods to create stable dispersion. Surface grafting of nanoparticles with appropriate polymers can form stable dispersions in suitable host polymer matrix even without annealing [49]. If the grafted chains are sufficiently longer than the matrix chain, while the grafting density remains low, the matrix chains can interpenetrate to promote miscibility between the particles and the matrix [49]. Dispersion change due to thermal annealing was attributed to the surface mobility, which induces the change of interaction between nanoparticle and matrix polymer.

In this work, however, hydrogen-terminated SiNCs was utilized, which is limiting the surface mobility effect on dispersion mechanism. In electronic device application, organic ligands are not preferable since they inhibit the charge transfer, reducing the device performance significantly [50]. Therefore, due to minor surface mobility among the particles and matrix, there is no significant dispersion enhancement observed after thermal annealing.

3.5.1. Thermal Annealing Temperature

Figure 3-6 shows the effect of thermal annealing temperature on the ESR signal, representing the amount of defect in SiNPs semi-quantitatively~~.~~ Thermal annealing at 150°C reduces the amount of defect significantly, nearly 80% of the non-annealed sample. However, higher annealing temperature at 200°C and 250°C show an increase of ESR signal intensity, although it still has a lower amount of defect compared to the non-annealed sample. Thermal annealing has been reported for defect reduction (dangling bond) at the surface of SiNPs [51]. The temperature of thermal annealing SiNPs plays an essential role, as it may affect the Si-H bonding at the surface of SiNPs. Thermal annealing with a temperature above 200°C causes the desorption of hydrogen at the surface, resulting in the increase of defect that is represented in the ESR signal increase. On the other hand, the annealing temperature well above the glass transition of PS is required for interfacial interaction between filler and matrix. Therefore, thermal annealing at 150°C was employed for thermal transport investigation on nanocomposite samples.

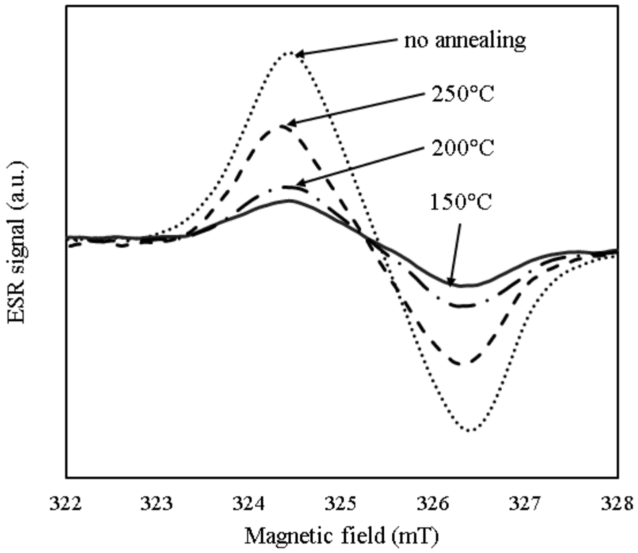

Figure 3-6. ESR spectra of SiNPs before and after thermal annealing at different temperatures of 150°C, 200°C, and 250°C.

3.5.2. Nanocomposite Characterization

Material characterizations by Raman spectroscopy was carried out to observe any molecular changes in the interfacial region of materials. Samples with a high volume fraction (31.1%) were analyzed in order to gain the maximum effect of the interfacial molecular structure at material boundaries. Raman spectra of thermal annealed SiNPs/PS nanocomposite is compared with that of before annealing and PS only sample, as shown in Figure 3-7. It is shown that most of the peaks have no significant change due to a thermal annealing process. However, a peak shift was observed near 2100 cm^{-1}, which is attributed to Si-H stretching vibration modes [6]. The peak shifted from 2117 cm^{-1} to lower frequency at 2105 cm^{-1} on the annealed sample. This peak shift of Raman spectrum indicates the changes in molecular behavior that is triggered by a thermal annealing process. Si-H peak is sensitive to changes in the environment, and the Raman peak shift to lower frequency can be caused by the release of compressive stress [52], [53]. Therefore, the peak shift of the Si-H stretching mode may indicate the stress releasing during the thermal annealing process. Furthermore, it is also interesting to note that strong peak at approximately 2100 cm^{-1}, which is not commonly observed in hydrogen passivated bulk Si, is caused by the effect of the large surface area of SiNCs [54].

In addition, the existence of highly crystalline SiNPs can be explicitly confirmed by the sharp peak of Raman shift at 517 cm^{-1}. Compared with bulk crystalline silicon, which has a peak at 520 cm^{-1}, slight peak shift was observed due to the phonon confinement effect, as was observed theoretically and experimentally for nanocrystals smaller than 20 nm [19]–[21]. Redshift (change to lower wavenumber) of the Raman spectrum can also be caused by mechanical stress on the sample [55].

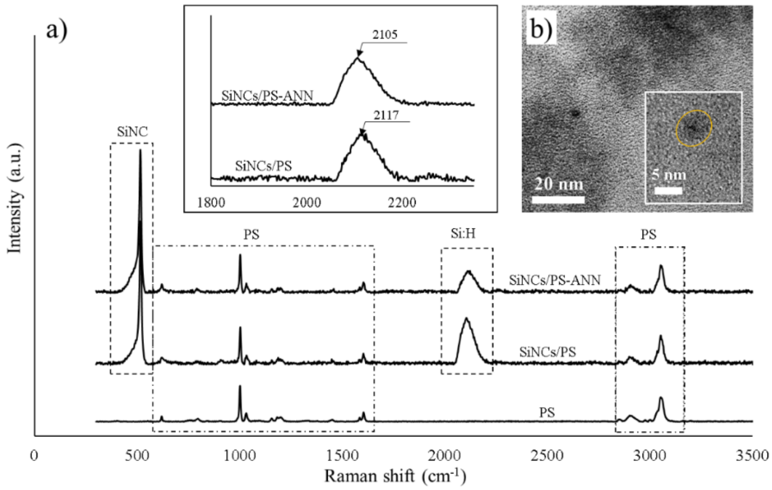

Figure 3-7. a) Raman spectra of thermal annealed SiNCs/PS nanocomposite (SiNCs/PS-ANN) at 150°C compared with the samples before annealing of nanocomposite (SiNCs/PS) and polystyrene (PS), presenting the region of the peak of SiNCs and PS components. Peak shift observed at Si-H stretching vibration (inset) represents the effect of thermal annealing on molecular physical interaction at interfacial region; b) TEM cross-section image of SiNCs/PS nanocomposite after the thermal annealing process.

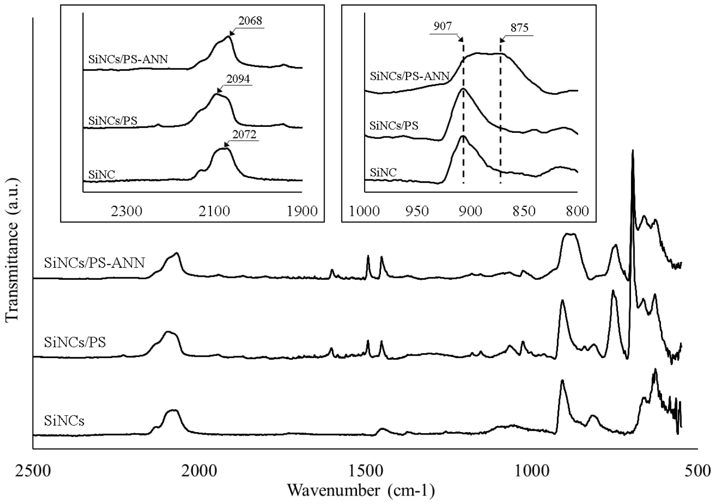

Figure 3-8. FTIR spectra: (i) Thermal annealed SiNCs/PS nanocomposite (SiNCs/PS-ANN) at 150°C; (ii) The nanocomposite sample before annealing (SiNCs/PS); (iii) SiNCs. Peak shift shown at several vibration modes (inset) represents the effect of thermal annealing on the surface hydrogen and PS interaction.

Physical dispersion condition of SiNCs in the PS matrix is shown in Figure 3-7(b). TEM cross-section image of thermally annealed nanocomposite sample (3.6vol%) indicates that agglomerates of SiNCs (dark area) could still be observed within the PS matrix (light area). TEM image also implies that particle size of ca. 6 nm is preserved during the thin film fabrication and thermal annealing process.

In addition to Raman spectra, FTIR spectra of samples are presented in Figure 3-8. In agreement with Raman spectra, FTIR spectra show peak changes at near 2100 cm^{-1}, representing the stretching mode of $Si–H_2$, which can be blurred by $(Si–H_2)_n$ [56]. The SiNCs' peak at 2072 cm^{-1} shifted to the higher wavenumber of nanocomposite at 2094 cm^{-1}, indicates the compressive stress due to the presence of PS among the SiNCs. Thermal annealing on nanocomposite causes the peak shift to lower wavenumber at 2069 cm^{-1}, which is analogous with Raman spectra, induced by stress release during the thermal annealing process.

Further analysis is carried out on FTIR spectra at lower wavenumber around 870–910 cm^{-1}, attributed to di-hydride $(Si–H_2)$ and poly-hydride $((Si–H_2)_2)$ complexes [56]–[58]. The identical peaks at 907 cm^{-1} are observed in both SiNCs and non-treated nanocomposite sample. However, broad spectrum with multiple peaks at 875–907 cm^{-1}, attributed to the bending (scissor) vibration modes [56]–[58]. The broadening effect of IR peaks indicates more $Si–H_2$ bonds are formed due to thermal annealing. This result is also in agreement with ESR spectra, which shows defect (dangling bond) reduction after thermal annealing.

Thermal conductivity of SiNPs/PS nanocomposite as a function of SiNPs volume fraction is presented in Figure 3-9. Compared with the samples before annealing, thermal conductivity measurement results show increasing value at a wide range of SiNPs volume fraction. The increase of nanocomposite thermal conductivity supports the hypothesis that phonon transport mechanism at the material interface of filler and matrix play has major effect, regardless of the crystallinity of the filler (SiNPs).

The material characterization provided by Raman spectroscopy and FTIR spectroscopy shows a peak shift of Si-H_x, indicating the change in the interaction between molecules at the surface of SiNPs and PS after thermal annealing. However, Raman spectra show only peak change of SiNPs component, without any significant peak change observed from PS molecules. The Si-H are located at the surface of SiNPs, with direct interaction with the surrounding environment, i.e., PS molecule. Therefore, it can be easily affected by any changes of neighboring molecules, and strongly represented in Raman spectra. On the other hand, there is no particular part of the PS molecule that has direct interaction with the SiNPs surface. With only a part of PS that has direct interaction with SiNPs, it is difficult to show any molecular vibrational changes of PS that is caused by interaction with the environment at the material interface.

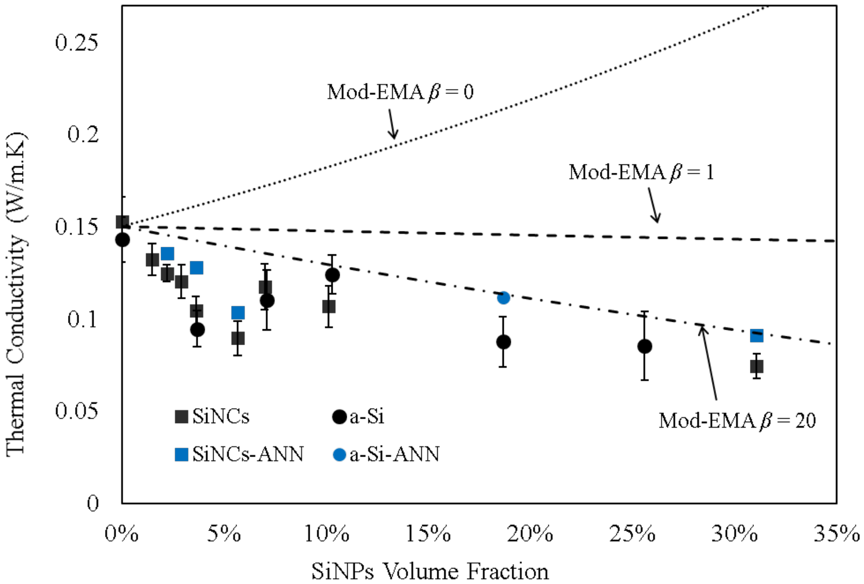

Figure 3-9. Thermal conductivity of annealed SiNPs/PS nanocomposite samples (blue) and as-produced nanocomposite sample (black) measured by TWA, compared with thermal conductivity model (Mod-EMA) that include the effect of thermal boundary resistance, represented by α

Peak shift to a lower frequency, or commonly known as redshift, represents the releasing of residual stress that may be formed during the thin film fabrication by spin coating [59]. As a result, the phonon scattering rate at the material interface decrease and the overall thermal conductivity of nanocomposite increase. Furthermore, the interface between filler and matrix has been studied due to its critical effect on nanocomposite properties [60]. Li et al. describe that interfacial interaction of filler and matrix forms a 3D interfacial region at the surrounding of fillers. Although this region may be very thin, which depend on the interaction of filler/matrix, it has a significant effect on the bulk properties of nanocomposite due to the large interfacial area to volume ratio of the nanocomposite. Therefore, any minor change in the molecular structure at the interfacial region, which is observed on Si-H in this case, have a significant role in determining the thermal transport properties of the nanocomposite. Defect reduction at SiNPs surface, which is observed by ESR, may also affect the molecular structure at the interfacial region. However, the effect of lattice defect on phonon scattering mechanism requires further observation and analysis.

In addition, a numerical simulation study of nanocomposite based on extended irreversible thermodynamic (ETI) also described the major role of the material interface in the effective thermal conductivity of nanocomposite [61]. Particles dimension and material boundary properties were expressed as major parameters that determine the thermal transport properties, playing a decisive role in the decrease or increase of thermal conductivity [61]. Materials boundary will affect the interfacial region, which determines the type of phonon-interface scattering (diffusive or specular). In agreement with the result explained in the previous chapter, phonon scattering at the interfacial region, which is represented by thermal boundary resistance, is a major role in determining the thermal transport mechanism in the nanocomposite.

3.6. Conclusion

In summary, we have produced a-Si/PS nanocomposite and measured the density, specific heat, and thermal diffusivity to determine thermal conductivity. The measurement results were compared with SiNCs/PS nanocomposite and showed insignificant discrepancy due to the lattice structure, revealed that the phonon scattering as the main factor of thermal conductivity decrease.

Compared with the thermal conductivity models for nanocomposite, which include the effect of thermal boundary resistance, our measurement results show the good agreement of thermal conductivity. Phonon confinement effect may be neglected, and phonon scattering at SiNPs/PS boundary plays a major role in determining thermal transport at room temperature.

Post-processing of thermal annealing was applied on nanocomposite, and thermal conductivity measurement result shows the increase of thermal conductivity values. Although there is no significant enhancement of SiNPs dispersion in the PS matrix, thermal annealing at above T_g induced molecular structure change of stress release or restructuration, resulting in thermal transport enhancement at the interfacial region. Large interfacial area of nanocomposite amplifies the minor change in the molecular structure at the interfacial region, significantly determining the thermal transport properties of the nanocomposite. The combination of interfacial region engineering, which also determines the particle dispersion, and post-processing provides controllable thermal transport properties of the nanostructured material and to be exploited for further study.

3.7. References

[1] A. Miura, S. Zhou, T. Nozaki, and J. Shiomi, “Crystalline-Amorphous Silicon Nanocomposites with Reduced Thermal Conductivity for Bulk Thermoelectrics,” *ACS Appl. Mater. Interfaces*, vol. 7, no. 24, pp. 13484–13489, Jun. 2015.

[2] Y. Ding, R. Gresback, R. Yamada, K. Okazaki, and T. Nozaki, “Hybrid silicon nanocrystal/poly(3-hexylthiophene-2,5-diyl) solar cells from a chlorinated silicon precursor,” *Jpn. J. Appl. Phys.*, vol. 52, no. 11 PART 2, pp. 2–7, 2013.

[3] T. Nozaki, Y. Ding, and R. Gresback, “Plasma Synthesis of Silicon Nanocrystals: Application to Organic/Inorganic Photovoltaics through Solution Processing,” *Mater. Sci. Forum*, vol. 783–786, pp. 2002–2004, May 2014.

[4] Y. Ding, R. Gresback, K. Okazaki, and T. Nozaki, “Silicon nanocrystal fabrication by using non-thermal plasma and application to hybrid Si-nanocrystal / P3HT solar cells,” vol. 305605, no. 2011, p. 305605, 2012.

[5] S. Volz, J. Shiomi, M. Nomura, and K. Miyazaki, “Heat conduction in nanostructured materials,” *J. Therm. Sci. Technol.*, vol. 11, no. 1, pp. JTST0001–JTST0001, 2016.

[6] F. B. Juangsa, Y. Muroya, M. Ryu, J. Morikawa, and T. Nozaki, “Thermal conductivity of silicon nanocrystals and polystyrene nanocomposite thin films,” *J. Phys. D. Appl. Phys.*, vol. 49, no. 36, p. 365303, Sep. 2016.

[7] Y. Nakamura, M. Isogawa, T. Ueda, S. Yamasaka, H. Matsui, J. Kikkawa, S. Ikeuchi, T. Oyake, T. Hori, J. Shiomi, and A. Sakai, “Anomalous reduction of thermal conductivity in coherent nanocrystal architecture for silicon thermoelectric material,” *Nano Energy*, vol. 12, pp. 845–851, Mar. 2015.

[8] Z. Wang, J. E. Alaniz, W. Jang, J. E. Garay, and C. Dames, “Thermal conductivity of nanocrystalline silicon: Importance of grain size and frequency-dependent mean free paths,” *Nano Lett.*, vol. 11, no. 6, pp. 2206–2213, Jun. 2011.

[9] T. Kihara, T. Harada, and N. Koshida, “Precise thermal characterization of confined nanocrystalline silicon by 3ω method,” *Japanese J. Appl. Physics, Part 1 Regul. Pap. Short Notes Rev. Pap.*, vol. 44, no. 6 A, pp. 4084–4087, Jun. 2005.

[10] M. C. Wingert, S. Kwon, M. Hu, D. Poulikakos, J. Xiang, and R. Chen, “Sub-amorphous Thermal Conductivity in Ultrathin Crystalline Silicon Nanotubes,” *Nano Lett.*, vol. 15, no. 4, pp. 2605–2611, Apr. 2015.

[11] L. Yang, Y. Yang, Q. Zhang, Y. Zhang, Y. Jiang, Z. Guan, M. Gerboth, J. Yang, Y. Chen, D. Greg Walker, T. T. Xu, and D. Li, “Thermal conductivity of individual silicon nanoribbons,” *Nanoscale*, vol. 8, no. 41, pp. 17895–17901, 2016.

[12] T. Kurihara, J. Morikawa, and T. Hashimoto, “Measurement of the thermal diffusivity of thin films by an AC joule-heating method,” *Int. J. Thermophys.*, vol. 18, no. 2, pp. 505–513, Mar. 1997.

[13] J. Kalowekamo and E. Baker, “Estimating the manufacturing cost of purely organic solar cells,” *Sol. Energy*, vol. 83, no. 8, pp. 1224–1231, Aug. 2009.

[14] S. Moon, M. Hatano, M. Lee, and C. P. Grigoropoulos, “Thermal conductivity of amorphous silicon thin films,” *Int. J. Heat Mass Transf.*, vol. 45, no. 12, pp. 2439–2447, Jun. 2002.

[15] M. C. Wingert, J. Zheng, S. Kwon, and R. Chen, “Thermal transport in amorphous materials: a review,” *Semicond. Sci. Technol.*, vol. 31, no. 11, p. 113003, 2016.

[16] Y. Ding, R. Yamada, R. Gresback, S. Zhou, X. Pi, and T. Nozaki, “A parametric study of non-thermal plasma synthesis of silicon nanoparticles from a chlorinated precursor,” *J. Phys. D. Appl. Phys.*, vol. 47, no. 48, p. 485202, 2014.

[17] D. Gracin, K. Juraic, and I. Bogdanovic-Radovic, “Estimation of amorphous silicon thin film density by optical methods,” *Vacuum*, vol. 80, no. 1, pp. 146–150, 2005.

[18] S. Holding, “Polymers: A Property Database,” *Chromatographia*, vol. 72, no. 5–6, pp. 587–587, Sep. 2010.

[19] I. Doğan and M. C. M. van de Sanden, “Direct characterization of nanocrystal size distribution using Raman spectroscopy,” *J. Appl. Phys.*, vol. 114, no. 13, p. 134310, 2013.

[20] I. Doğan, N. J. Kramer, R. H. J. Westermann, K. Dohnalová, A. H. M. Smets, M. A. Verheijen, T. Gregorkiewicz, and M. C. M. Van De Sanden, “Ultrahigh throughput plasma processing of free standing silicon nanocrystals with lognormal size distribution,” *J. Appl. Phys.*, vol. 113, no. 13, p. 134306, 2013.

[21] K. H. Khoo, A. T. Zayak, H. Kwak, and J. R. Chelikowsky, “First-Principles Study of Confinement Effects on the Raman Spectra of Si Nanocrystals,” *Phys. Rev. Lett.*, vol. 105, no. 11, p. 115504, Sep. 2010.

[22] Y. Ding, R. Yamada, R. Gresback, S. Zhou, X. Pi, and T. Nozaki, “A parametric study of non-thermal plasma synthesis of silicon nanoparticles from a chlorinated precursor,” *J. Phys. D. Appl. Phys.*, vol. 47, no. 48, p. 485202, 2014.

[23] R. K. Endo, Y. Fujihara, and M. Susa, “Calculation of the density and heat capacity of silicon by molecular dynamics simulation,” *High Temp. - High Press.*, vol. 35–36, no. 5, pp. 505–511, 2003.

[24] A. A. Balandin, “Nanoscale Thermal Management,” *Ieee Potentials*, no. March, pp. 11–15, 2002.

[25] A. A. Balandin and D. L. Nika, “Phononics in low-dimensional materials,” *Mater. Today*, vol. 15, no. 6, pp. 266–275, Jun. 2012.

[26] M. Maldovan, “Phonon wave interference and thermal bandgap materials,” *Nat. Mater.*, vol. 14, no. 7, pp. 667–674, Jun. 2015.

[27] K. Esfarjani, G. Chen, and H. T. Stokes, “Heat transport in silicon from first-principles calculations,” *Phys. Rev. B*, vol. 84, no. 8, p. 085204, Aug. 2011.

[28] R. Anufriev and M. Nomura, “Reduction of thermal conductance by coherent phonon scattering in two-dimensional phononic crystals of different lattice types,” *Phys. Rev. B*, vol. 93, no. 4, pp. 1–6, 2016.

[29] J. C. Maxwell, “A treatise on electricity and magnetism | Vol. 1,” *Clarendon Press*, vol. 1. 1873.

[30] A. G. Every, Y. Tzou, D. P. H. Hasselman, and R. Raj, “The effect of particle size on the thermal conductivity of ZnS/diamond composites,” *Acta Metall. Mater.*, vol. 40, no. 1, pp. 123–129, 1992.

[31] K. Pietrak and T. S. Winiewski, “A review of models for effective thermal conductivity of composite materials,” *Open Access J. J. Power Technol.*, vol. 95, no. 1, pp. 14–24, 2015.

[32] C.-W. Nan, R. Birringer, D. R. Clarke, and H. Gleiter, “Effective thermal conductivity of particulate composites with interfacial thermal resistance,” *J. Appl. Phys.*, vol. 81, no. 10, p. 6692, 1997.

[33] A. Minnich and G. Chen, “Modified effective medium formulation for the thermal conductivity of nanocomposites,” *Appl. Phys. Lett.*, vol. 91, no. 7, p. 073105, Aug. 2007.

[34] D. R. Lide, *CRC handbook of chemistry and physics*. CRC Press, 2009.

[35] A. Devpura, Patrick E. Phelan, Ravi S., “Size Effects on the Thermal Conductivity of Polymers Laden With Highly Conductive Filler Particles,” *Microscale Thermophys. Eng.*, vol. 5, no. 3, pp. 177–189, Jul. 2001.

[36] D. P. D. Bergman, Theodore L, Adrienne S. Lavine, Frank P. Incropera, *Introduction to Heat Transfer*, vol. XXXIII, no. 2. 2014.

[37] D. G. Cahill, S. K. Watson, and R. O. Pohl, “Lower limit to the thermal conductivity of disordered crystals,” *Phys. Rev. B*, vol. 46, no. 10, pp. 6131–6140, Sep. 1992.

[38] D. G. Cahill, M. Katiyar, and J. R. Abelson, “Thermal conductivity of a-Si:H thin films,” *Phys. Rev. B*, vol. 50, no. 9, pp. 6077–6081, 1994.

[39] S. Pal, G. Balasubramanian, and I. K. Puri, “Modifying thermal transport in electrically conducting polymers: Effects of stretching and combining polymer chains,” *J. Chem. Phys.*, vol. 136, no. 4, p. 044901, Jan. 2012.

[40] T. C. Hales, “The status of the kepler conjecture,” *Math. Intell.*, vol. 16, no. 3, pp. 47–58, Jun. 1994.

[41] J. Chen, G. Zhang, and B. Li, “Thermal contact resistance across nanoscale silicon dioxide and silicon interface,” *J. Appl. Phys.*, vol. 112, no. 6, p. 064319, Sep. 2012.

[42] E. Lampin, Q.-H. Nguyen, P. A. Francioso, and F. Cleri, “Thermal boundary resistance at silicon-silica interfaces by molecular dynamics simulations,” *Appl. Phys. Lett.*, vol. 100, no. 13, p. 131906, Mar. 2012.

[43] K. Zheng, F. Sun, X. Tian, J. Zhu, Y. Ma, D. Tang, and F. Wang, “Tuning the Interfacial Thermal Conductance between Polystyrene and Sapphire by Controlling the Interfacial Adhesion,” *ACS Appl. Mater. Interfaces*, vol. 7, no. 42, pp. 23644–23649, Oct. 2015.

[44] Y. Agari, A. Ueda, Y. Omura, and S. Nagai, “Thermal diffusivity PMMA / PC blends and conductivity of,” *Polymer (Guildf).*, vol. 38, no. 4, pp. 801–807, 1997.

[45] R. Sultan, A. D. Avery, J. M. Underwood, S. J. Mason, D. Bassett, and B. L. Zink, “Heat transport by long mean free path vibrations in amorphous silicon nitride near room temperature,” *Phys. Rev. B*, vol. 87, no. 21, p. 214305, Jun. 2013.

[46] R. Anufriev, J. Maire, and M. Nomura, “Reduction of thermal conductivity by surface scattering of phonons in periodic silicon nanostructures,” *Phys. Rev. B*, vol. 93, no. 4, p. 045411, Jan. 2016.

[47] Z. Liang, T. E. Wilson, and P. Keblinski, “Phonon interference in crystalline and amorphous confined nanoscopic films,” *J. Appl. Phys.*, vol. 121, no. 7, p. 075303, 2017.

[48] S. Chandran and J. K. Basu, “Effect of nanoparticle dispersion on glass transition in thin films of polymer nanocomposites,” *Eur. Phys. J. E*, vol. 34, no. 9, p. 99, Sep. 2011.

[49] A. Arceo, L. Meli, and P. F. Green, “Glass Transition of Polymer−Nanocrystal Thin Film Mixtures: Role of Entropically Directed Forces on Nanocrystal Distribution,” *Nano Lett.*, vol. 8, no. 8, pp. 2271–2276, Aug. 2008.

[50] R. Gresback, T. Nozaki, and K. Okazaki, “Synthesis and oxidation of luminescent silicon nanocrystals from silicon tetrachloride by very high frequency nonthermal plasma.,” *Nanotechnology*, vol. 22, no. 30, p. 305605, Jul. 2011.

[51] S. Niesar, A. R. Stegner, R. N. Pereira, M. Hoeb, H. Wiggers, M. S. Brandt, and M. Stutzmann, “Defect reduction in silicon nanoparticles by low-temperature vacuum annealing,” *Appl. Phys. Lett.*, vol. 96, no. 19, p. 193112, May 2010.

[52] D. A. Strubbe, E. C. Johlin, T. R. Kirkpatrick, T. Buonassisi, and J. C. Grossman, “Stress effects on the Raman spectrum of an amorphous material: Theory and experiment on a-Si:H,” *Phys. Rev. B - Condens. Matter Mater. Phys.*, vol. 92, no. 24, p. 241202, Dec. 2015.

[53] D. R. McKenzie, “Infrared absorption and bonding in amorphous hydrogenated silicon-carbon alloys,” *J. Phys. D. Appl. Phys.*, vol. 18, no. 9, pp. 1935–1948, 1985.

[54] T. Nozaki, K. Sasaki, T. Ogino, D. Asahi, and K. Okazaki, “Microplasma synthesis of tunable photoluminescent silicon nanocrystals,” *Nanotechnology*, vol. 18, no. 23, p. 235603, Jun. 2007.

[55] C. Ossadnik, S. Vepřek, and I. Gregora, “Applicability of Raman scattering for the characterization of nanocrystalline silicon,” *Thin Solid Films*, vol. 337, no. 1–2, pp. 148–151, 1999.

[56] L. Gao, N. P. Lu, L. G. Liao, A. L. Ji, and Z. X. Cao, “Nanocrystalline Si : H thin films grown at room temperature with plasma-enhanced chemical vapour deposition at a very high pressure,” *J. Phys. D. Appl. Phys.*, vol. 45, no. 33, p. 335104, Aug. 2012.

[57] L. S. Sidhu, T. Kosteski, S. Zukotynski, and N. P. Kherani, “Infrared vibration spectra of hydrogenated, deuterated, and tritiated amorphous silicon,” *J. Appl. Phys.*, vol. 85, no. 5, pp. 2574–2578, Mar. 1999.

[58] M. Cardona, “Vibrational spectra of Hydroge nin Silicon and Germanium,” *Phys. Status Solidi*, vol. 118, no. 463, 1983.

[59] P. Damman, S. Gabriele, S. Coppée, S. Desprez, D. Villers, T. Vilmin, E. Raphaël, M. Hamieh, S. Al Akhrass, and G. Reiter, “Relaxation of Residual Stress and Reentanglement of Polymers in Spin-Coated Films,” *Phys. Rev. Lett.*, vol. 99, no. 3, p. 036101, Jul. 2007.

[60] Y. Li, Y. Huang, T. Krentz, B. Natarajan, T. Neely, and L. S. Schadler, “Polymer Nanocomposite Interfaces: The Hidden Lever for Optimizing Performance in Spherical Nanofilled Polymers,” in *Interface/Interphase in Polymer Nanocomposites*, Hoboken, NJ, USA: John Wiley & Sons, Inc., 2016, pp. 1–69.

[61] G. Lebon, H. Machrafi, and M. Grmela, “An extended irreversible thermodynamic modelling of size-dependent thermal conductivity of spherical nanoparticles dispersed in homogeneous media,” *Proc. R. Soc. A Math. Phys. Eng. Sci.*, vol. 471, no. 2182, p. 20150144, Oct. 2015.

Chapter 4: Interfacial Properties and Phonon Transport

This chapter is under preparation for submission as: Firman Bagja Juangsa, Ryu Meguya, Junko Morikawa, Tomohiro Nozaki "Interfacial region effect on thermal conductivity of silicon nanocrystals and polystyrene nanocomposite".

4.1. Abstract

Thermal transport in nanosize materials has been widely studied due to the novel properties, including size-dependent thermal transport properties. Bulk-size nanostructures are often utilized for thermal property investigation as well as device application. Nanocomposite structure of silicon nanocrystals (SiNCs) and polystyrene (PS) has been studied and reported to have a significant thermal transport suppression that is attributed to the thermal resistance at material interfaces. Theoretical effective medium approximation (EMA) model for nanocomposite has considered the thermal boundary resistance, yet a constant deviation is observed between model and measurement result. In this work, thermal transport investigation is focused on the properties of the polymer, which is known as morphology dependent, at a region near to interfacial boundary. Nanocomposites were produced from SiNCs with significantly different diameter of 6 nm and 60 nm and measured for thermal conductivity to analyze the effect of particle size to the effective thermal conductivity and its deviation. The result showed that interfacial region of PS matrix has a significant effect on thermal transport, and the EMA model can be enhanced by modifying the thermal conductivity of matrix due to confinement effect at the interfacial region, and well-matched with the measurement result. The result presents that interaction at the material interface and its effect on interfacial region doubtlessly play an essential role in determining the thermal transport, and it would provide the possibility of

controllable thermal transport properties for wide application of polymer-based nanocomposite devices.

4.2. Introduction

Thermal transport in nanosize materials has been extensively studied due to their novel properties, which is fundamentally different from the bulk form. Having well-known utilized in optoelectronic devices, nano-size crystalline silicon (silicon nanocrystals; SiNCs) have been observed for their size-dependent properties, where the thermal conductivity is significantly influenced by the particle size [1], [2]. Size-dependent of thermal transport property occurs when the material size is comparable to or smaller than the intrinsic phonon mean free path of the material, known as the Casimir effect [3], [4].

Meanwhile, nano-size materials such as SiNCs are often utilized as bulk-size nanostructured materials, such as nanocomposite, for thermal properties investigation as well as device application such as solar cell [5], [6] and thermoelectric [7]. Since the specific surface area of SiNCs increases with decreasing size due to the high surface to volume ratio, thermal transport properties of nanocomposite are dominantly determined by the mechanism at the interfacial boundary. Therefore, understanding the thermal transport at the interfacial boundary is essential to investigate and control the effect of SiNCs characteristics on the properties of the nanocomposite.

A number of experimental investigations on thermal conductivity of nanocomposite reported a significant effect of thermal transport suppression in the nanocomposite, which is attributed to the thermal resistance at material interfaces [8]–[10]. Theoretical thermal conductivity based on the conventional theory of effective medium approximation (EMA) model has been developed to consider the effect of interfacial thermal resistance into the models [11], [12]. Those thermal conductivity models are in good agreement with the experimental result and Monte Carlo numerical simulation of nanocomposites such as Si/Ge, SiC/Al, and diamond/ZnS. However, the effect of material interface on polymer-based nanocomposite is not well understood.

As a soft material, the polymer has unique properties compared to hard materials, such as crystalline solid. Thermal conductivity of polymers is highly dependent on their morphology [13]–[15]. Most of the polymers in bulk form have a typical thermal conductivity value at the order of 0.1 W/m.K, which is a result of extended vibration modes of lattice vibration. Chain alignment control has been reported as one method to adjust the thermal conductivity, which can be carried out by chemical doping, mechanical strain, or modification during the polymerization process [13], [16], [17]. Very high thermal conductivity of 42~104 W/m.K were reported from nanofiber of polyethylene, by measuring thermal conductivity in the orientation direction of a drawn single nanofiber and further reduce the defect [18], [19]. However, alignment strategy of the polymer chain is only effective and well-observed for crystalline structure, while the effect of alignment and material size in amorphous polymers are still not fully understood. Therefore, in nanostructured materials with polymer employed as a matrix, it is crucial to understand how the polymer at material interface influenced by interfacial interaction between filler and matrix.

In this work, SiNCs/polystyrene (PS) nanocomposites are produced and measured for their thermal conductivity, representing the thermal transport property of nanostructured materials. Crystalline silicon particles with significantly different diameter of 6nm and 60nm were employed to investigate the size effect on thermal conductivity of nanocomposite. Furthermore, experimental results are compared with numerical calculation of thermal conductivity models to estimate the thermal boundary resistance value at the material interface and analyze the effect of material interface on polymer morphology. Based on the comparison result, the polymer morphology effect is taken into account to improve the thermal conductivity model for polymer-based nanocomposite.

Fabrication process and measurement methods are performed at low temperature, allowing the preservation of unique size-dependent properties (the quantum size effect) and low-cost fabrication.

4.3. Experiment methods

SiNPs were produced by nonthermal plasma enhanced chemical vapor deposition (CVD), as explained in details at previous chapters. SiNCs nucleation and crystal growth process is carried out in the reactor where a very high plasma (VHF) 70 MHz power is supplied. Mixture gas of precursor $SiCl_4$, H_2, and Ar flow through the quartz tube reactor as shown schematically in Figure 4-1.

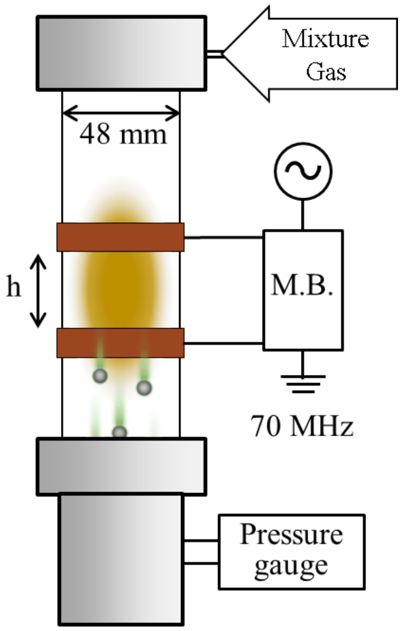

Figure 4-1. Schematic of a nonthermal plasma reactor with a plasma region indicated between two electrodes.

The decomposition process of $SiCl_4$ is followed by nucleation and particle growth process, which is induced by plasma. Nanoparticles are most likely negatively charged in nonthermal plasma; Coulomb repulsion force enables individual growth of nanoparticles without significant agglomeration. Moreover, charge recombination occurring on the nanoparticle surface provide energy necessarily for crystallization [20], [21]. The particles growth process is determined by reaction time in the plasma region, which is called residence time. By increasing the residence time, the larger size of SiNPs can be produced with the consideration of plasma input power that is determining the crystalline fraction in SiNPs.

The residence time of the synthesis process can be increased by increasing the distance between two electrodes (*h*), as shown in Figure 4-1. However, the maximum value of *h* is limited by several factors, such as the dimension of the synthesis apparatus and the plasma generation. Practically the length of *h* is limited by the length of the quartz tube reactor. If the length of *h* is large enough, it will affect the uniformity of plasma generated along the reactor, and a further increase of *h* length would prevent the plasma generation.

Therefore, highly crystalline silicon nanoparticles with a larger particle size are synthesized by tuning the residence time up to the maximum possible size with the current apparatus. For much larger particle size, SiNCs with an average size of 60nm were provided from EM Japan (NP-SI-2-1). Hydrogen surface termination is applied on all SiNCs by hydrofluoric (HF) etching process. SiNCs powder was placed on a Teflon mesh above a 50% HF/water solution in a closed container for more than 48 hours and followed by drying process by vacuuming for at least 2hours.

Nanocomposite samples were produced by the same process, as explained in the previous chapter. Atactic polystyrene (Sigma-Aldrich 430102) with average molecular weight ca. 192,000 was used for this work. SiNCs and PS were dispersed in benzonitrile (anhydrous, Sigma-Aldrich 294098) with predetermined SiNCs mass fraction of 0 ~ 50%. The volume fractions of each sample were determined based on the density reference values of silicon and PS (2.39 g/cm^3 and 1.05 g/cm^3, respectively) [22], [23]. The mixed solution of the SiNCs and PS was stirred for 24 hours to obtain a stable, well-dispersed solution before deposited on the substrate to produce a thin film sample. The thin film sample was dried in a vacuum chamber (<1 Pa) for 12 hours, in order to avoid gas trapped within the sample and to evaporate the remaining solvent. Thermal conductivity was determined based on measurement of thermal diffusivity by temperature wave analysis (TWA), while the specific heat and mass density are provided from the measurement result explained in the previous chapter.

4.4. Result and Discussion

4.4.1. Large Size SiNCs Synthesis

The mechanism of SiNPs synthesis process can be analyzed by observing the parameters on yield, crystallinity, and size of SiNPs produced by nonthermal plasma [24]. The synthesis yield is determined by specific energy input (SEI). SEI is defined as energy input per unit volume of gas as the following equation:

$$\mathrm{SEI}\ = \frac{\text{Plasma input power (W)}}{\text{Gas flow rate }(\mathrm{cm^3/s})}\,(\mathrm{J/cm^3}) \tag{4-1}$$

Figure 4-2a show the relationship between the yield of SiNPs, SEI, and $H_2/SiCl_4$ ratio. SiNPs yield is defined as the weight ratio of SiNPs collected at mesh filter to the silicon precursor contained in $SiCl_4$. For the various ratio of $H_2/SiCl_4$, SEI has an optimum value that produces a maximum yield of 50%. Below the optimum value, the yield increases with SEI because higher power produces a higher conversion rate of $SiCl_4$. However, above the optimum value, further increase of SEI lead to excessive consumption of initial $SiCl_4$, which plays an essential role in the nucleation process of SiNPs. Therefore, it is essential to maintain the SEI during parameter tuning in order to produce an optimum yield of SiNPs.

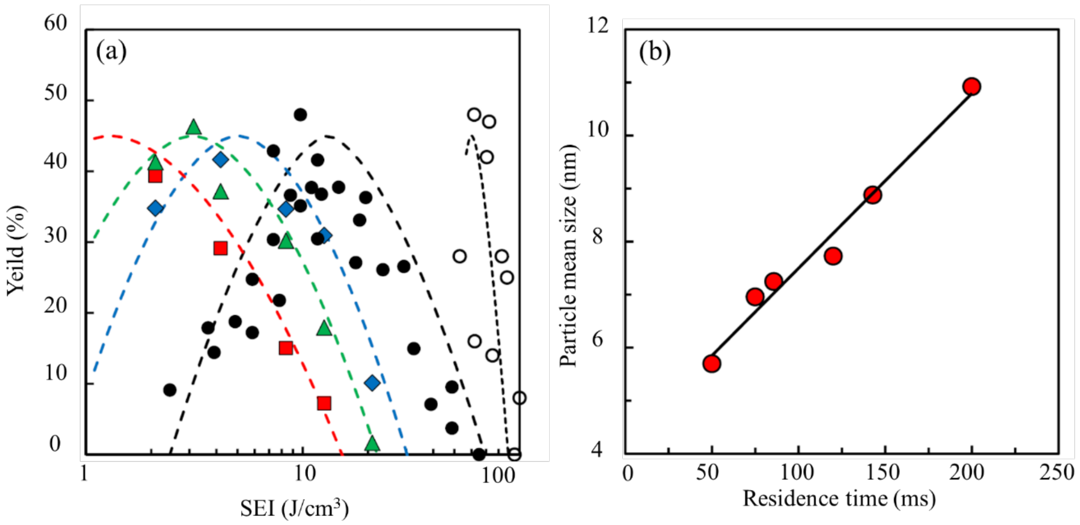

Figure 4-2. (a) SiNPs yield as a function of SEI and $H_2/SiCl_4$ ratio of 10(●), 5(♦), 2(▲), 1(■), and [25](○); (b) Particle mean size vs. residence time. Modified from [24] with permission from IOP Publishing 2014.

Large size SiNPs are produced by increase the residence time, which can be calculated as the following equation.

$$T\ (\text{residence time}) = \frac{\text{Plasma reactor volume } (\text{cm}^3)}{\text{Gas flow rate } (\text{cm}^3/\text{s})} \times 10^3 (\text{ms}) \tag{4-2}$$

According to the above formula, a larger size of SiNPs can be produced with a larger size of plasma reactor and less gas flow rate. As mentioned previously, plasma reactor volume is limited by the size of the synthesis apparatus and maximum distance between electrodes. Therefore the total gas flow rate supplied into the reactor is decreased to the minimum value. Minimum gas flow rate is tuned while considering the value of SEI and plasma power, which determines the yield and the crystallinity of SiNCs, respectively. Previous work reported an adjustable particle size with a linear relationship with residence time as presented in Figure 4-2(b)

In this work, the larger size of SiNPs is analyzed by AFM, and the result of mean particle size is presented in Figure 4-3. Maximum residence time of 185ms produce SiNPs with a mean particle size of 11.65 nm, nearly twice larger than the standard SiNPs size of 6 nm. Narrow size distribution is also observed from AFM analysis, indicating the perseverance of nonthermal plasma characteristic at a longer residence time process.

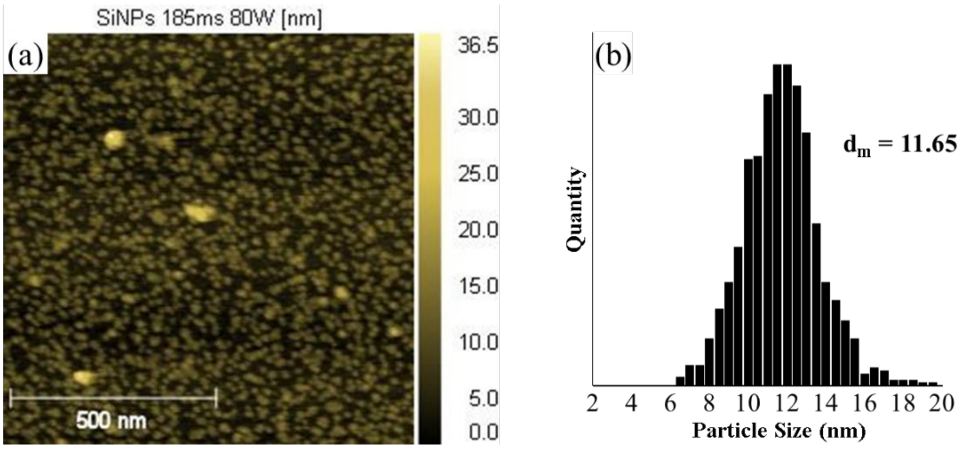

Figure 4-3. Mean size of SiNPs with longer residence time, which is determined based on (a) AFM image and (b) statistically calculated SiNPs size distribution.

However, in order to investigate the SiNPs size effect on nanocomposite thermal transport, the significant size difference is required. As previously shown in Figure 3-5, effective thermal conductivity has a negligible change for region $\beta > 5$. Since nanocomposite with SiNPs size 6 nm is well represented by $\beta = 20$, twice larger particles would give $\beta = 10$, which has a negligible effect on thermal conductivity of nanocomposite. The effect of material interface would still dominates over the effect of parthe ticle size effect. Therefore, for further analysis on larger particle size, crystalline silicon nanoparticles with a mean size of 60 nm (EM Japan; NP-SI-2-1) are employed for nanocomposite thermal transport analysis.

4.4.2. Interfacial Region Effect on Thermal Conductivity of Nanocomposite

Thermal conductivity values of nanocomposite determined by thermal properties measurement for both crystalline (SiNCs) and amorphous (a-SiNPs) with a particle size of 6 nm are shown in

Figure 4-4. Result obtained in previous works [10] indicated an insignificant effect of thermal transport mechanism inside the filler materials, represented by amorphous and crystalline silicon particles, showing a decreasing trend of thermal conductivity in terms of SiNPs volume fraction. In this work, further measurements were conducted on low SiNPs fraction region below 5 vol%, which is showing a continuous decreasing thermal conductivity trend from PS-only (0 vol%) sample to the thermal conductivity trend of SiNPs fraction above 5 vol%.

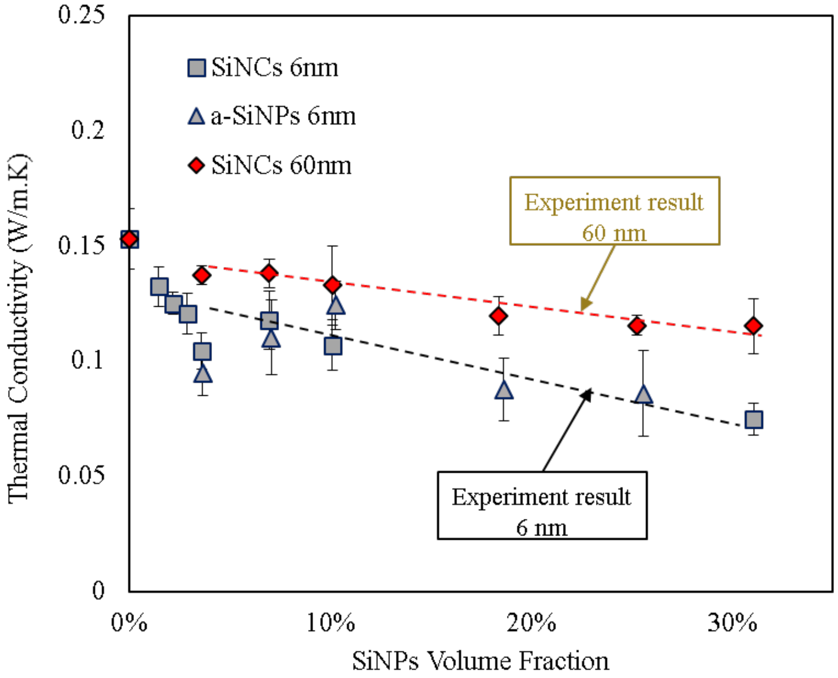

Figure 4-4 Thermal conductivity measurement results of nanocomposite employing silicon nanoparticles with different structure of crystalline and amorphous, and different particle size of 6 nm (grey) and 60 nm (red)

Figure 4-4 also demonstrates the effect of filler particle size in nanocomposite thermal conductivity by comparing the thermal conductivity measurement of SiNPs with 6 nm and 60 nm of particle diameter size. It can be identified that nanocomposite samples with larger particle size have higher thermal conductivity than smaller particle size, which is exhibited uniformly at any SiNPs volume fraction. This is mainly caused by the decrease of the interface are at larger particle size, which is reducing the effect of thermal resistance at the material interface on the overall thermal conductivity of nanocomposite. Also, the decrease of material interface density has an effect that thermal transport of nanocomposite is less determined by the mechanism at the material interface, while thermal transport properties of nanoparticle have an increasing effect on nanocomposite thermal conductivity. As the intrinsic thermal transport property of SiNPs is proportional to the particle size, it is understandable that nanocomposite samples with larger SiNPs size have higher thermal conductivity values.

Dispersion of SiNPs in nanocomposite is examined by TEM analysis, as presented in Figure 4-5. Similar dispersion condition is displayed in TEM images for both nanocomposite with different SiNCs size. At a low fraction of 3.7 vol%, presented in Figure 4-5 (a) and (c), groups of SiNCs are observed forming large islands of SiNCs regardless of the size of SiNCs. Similar dispersion of SiNCs at nanocomposite with a different SiNCs size indicates an identical interfacial interaction between SiNCs and PS. Since both of 6 nm and 60 nm, SiNCs has a hydrogen-terminated surface, which is produced by the HF etching process, the interaction between hydrogen molecules and PS molecules produce a similar interaction at the material interface, resulting in the similar dispersion of SiNCs in PS matrix. At a higher SiNCs fraction of 31.1 vol%, closely packed SiNCs structure can be observed from TEM images of both 6 nm and 60 nm SiNCs, shown in Figure 4-5 (b) and (d), respectively.

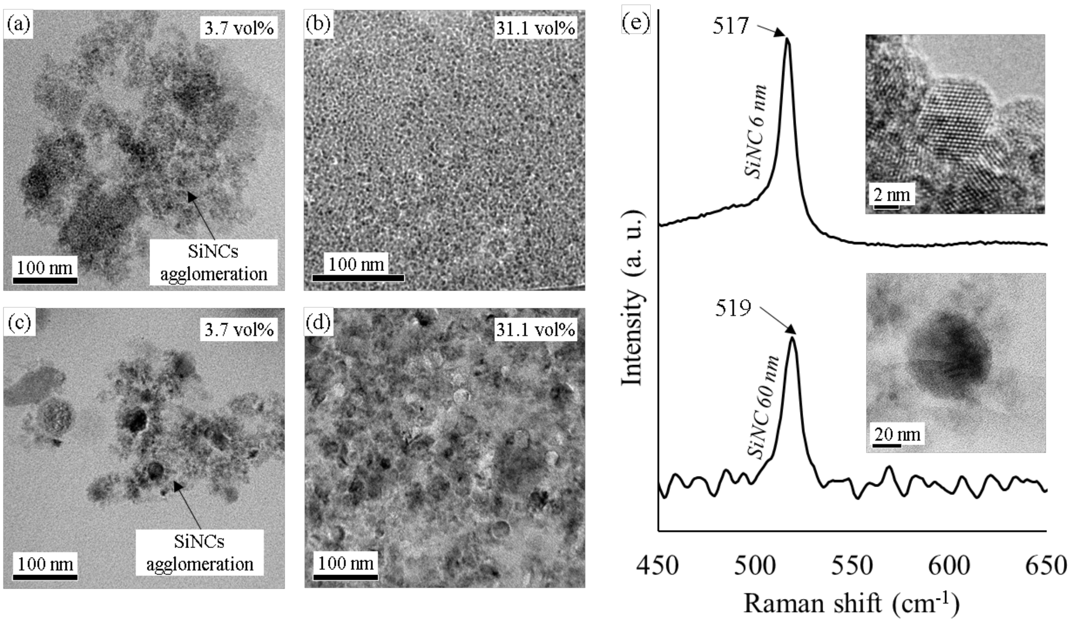

Figure 4-5 TEM images of SiNCs dispersion in PS matrix: agglomerations of SiNCs shown at low filler fraction of 3.7 vol%, for both (a) 6 nm and (d) 60 nm SiNCs; relatively close-packed structure of SiNCs at highest filler fraction of 31.1 vol% for both (b) 6 nm and (e) 60 nm SiNCs; TEM image of single SiNC, showing particle size of (c) 6 nm and (f) 60 nm SiNCs.

Raman spectra of both type of SiNC shown in Figure 4-5 (e), displaying a highly crystalline particle that is represented by sharp Raman peaks at 517 cm^{-1} and 519 cm^{-1} for 6 nm and 60 nm SiNC, respectively. The different Raman peaks of two SiNC size is due to the difference of phonon confinement effect that is shifting the Raman peak from bulk's value at 520 cm^{-1} to the lower wavenumber, as was observed theoretically and experimentally for SiNCs [26]–[28]. TEM images of SiNCs are presented as the inset of Figure 4-5 (e), showing the larger SiNCs is nearly ten times larger than the smaller SiNCs, indicated by the scale bar of each image.

Further analysis of thermal conductivity is observed by comparing the measurement values with the thermal conductivity model for nanocomposite material that considers the effect of the material interface in the calculation. At the previous chapter, a series of models are evaluated, and modified-

EMA model reported by Minnich et al. showed good agreement with experiment result by considering the significance of material interface as well as the thermal boundary resistance (TBR). Modified-EMA model can successfully calculate the thermal conductivity of nanocomposite (κ_c) with consideration of the material interface effect, which is represented with interface density (Φ) as shown in the following equation.

$$\Phi = \frac{6\varphi}{D} \tag{4-3}$$

$$\kappa_c(\Phi, d) = \frac{1}{3} C_m v_m \frac{1}{\left(\frac{1}{\Lambda_m}\right) + \left(\frac{\Phi}{4}\right)}$$
$$\times \frac{\kappa_p(D)\big(1 + 2\beta(\Phi, D)\big) + 2\kappa_m(\Phi) + 2\left(\frac{\Phi D}{6}\right)\left[\kappa_p(D)\big(1 - \beta(\Phi, D)\big) - \kappa_m(\Phi)\right]}{\kappa_p(D)\big(1 + 2\beta(\Phi, D)\big) + 2\kappa_m(\Phi) - \left(\frac{\Phi D}{6}\right)\left[\kappa_p(D)\big(1 - \beta(\Phi, D)\big) - \kappa_m(\Phi)\right]} \tag{4-4}$$

Where φ and d are volume fraction and particle size of SiNPs, while C, v, and Λ are volumetric specific heat, phonon group velocity, and phonon MFP for matrix and filler, represented by subscripts of m and p, respectively. The equation consists of two parts, the first part refer to the overall thermal conductivity that is affected by the interface density Φ. For macroscale filler size, the effect of interface density is negligible, so that the first part refers to the thermal conductivity of the polymer matrix. The second part of the equation accounts for the effect of particle size and the TBR parameter β. The increase of phonon scattering at the material interface due to particle size effect is represented the interface density Φ in the second term, resulting in the decreasing thermal conductivity as SiNPs fraction increases, as shown in Figure 4-4.

The comparison of thermal conductivity values obtained from the experimental measurement and modified-EMA model is presented in Figure 4-6. It has been explained in the previous chapter that β, which is a dimensionless parameter depending on the TBR between filler and matrix, well match with the experimental data at $\beta = 20$ for the particle size of 6 nm. According Kapitza radius formula that defines $\beta = R_{TBR}\kappa_m/(D/2)$, with the constant value of R_{TBR} and κ_m, β can be calculated for nanocomposite with larger particle size, giving $\beta = 2$ for the particle size of 60 nm. Modified-EMA model considers interface density (Φ) that amplifies the effect of TBR as SiNPs volume fraction increase. As the result, thermal conductivity value has a decreasing value, in an identical slope gradient with the measurement displayed in Figure 4-6. This confirms that Modified-EMA model can successfully represent the effect of material interfaces and their thermal resistance in determining the nanocomposite thermal conductivity. However, if we take a detailed view of the graph, there is a constant deviation between model calculation and experiment result for both of 6 and 60 nm SiNPs. The deviation may indicate the change of properties employed in the model due to the presence of SiNPs in nanocomposite.

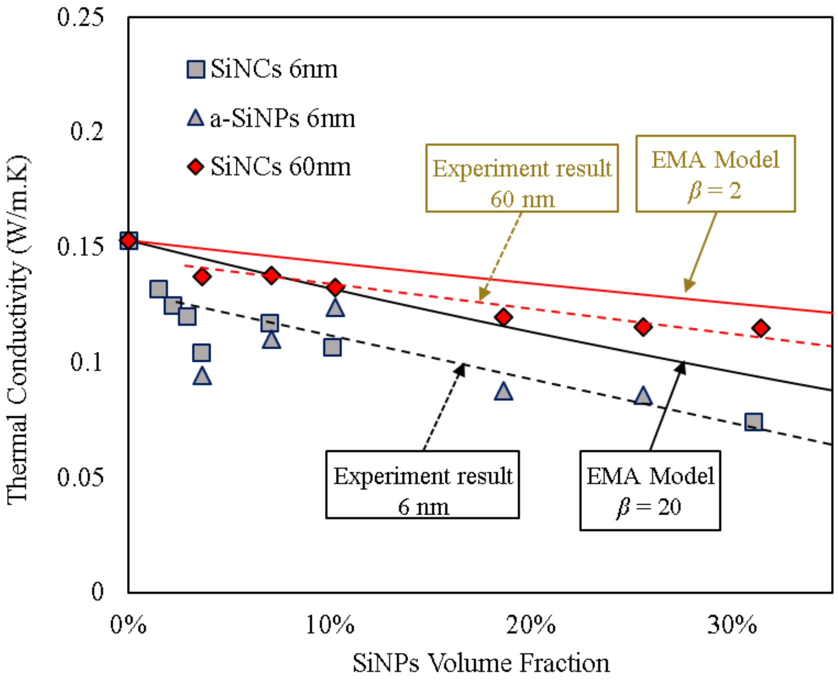

Figure 4-6 Thermal conductivity measurement results of nanocomposite samples compared with the modified-EMA model considering the thermal boundary resistance at the material interface

Polymer is a soft material, which has different behavior with other hard-solid materials, may be affected by interfacial interaction at material boundaries. The study on interfacial interaction at polymer nanocomposites suggested the critical role of structure and properties of filler/matrix interface in determining the bulk-properties of nanocomposite [29]. Interaction at the material interface affects the properties of the matrix, especially on soft material such as a polymer that is highly morphology-dependent. Morphology-dependent thermal transport property of polymers has been widely studied, including the very high thermal conductivity of ultra-drawn polyethylene nanofiber at 104 W/mK, which is two orders higher than its bulk form[19]. In the nanocomposite structure, the polymer matrix near particle that is affected by interfacial interaction would have different properties from the bulk polymer matrix and called the interfacial region, as shown in Figure 4-7.

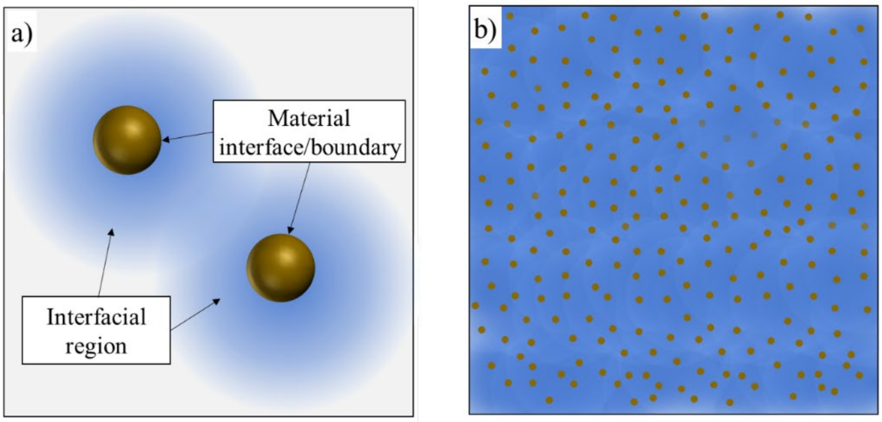

Figure 4-7 Schematic drawings of 2D nanocomposite with similar volume fraction (4 vol%) of SiNPs illustrating the significant fraction of interfacial region (thickness of 100 nm) as a function of filler particle size: nanocomposite with SiNPs size of a) 60 nm and b) 6 nm.

The effect of interfacial interaction on the interfacial region of the polymer has been observed experimentally by measuring the change of glass transition temperature (T_g) in poly(methyl methacrylate) (PMMA)-based nanocomposite [30]. Notable T_g increase of 5~10 K was observed from a relatively low nanoparticles fraction of 0.5 vol%, indicating a critical effect of filler presence in determining nanocomposite properties. The T_g deviation from bulk properties was attributed to the nanoparticle-polymer interactions that lead to internal stresses (confinement effect) within the polymer matrix, mainly near the material interface, forming an area called interfacial region. As a result, the internal stress induces the morphology change in the polymer at the interfacial region, which leads to deviation in thermal properties represented by T_g. In order to observe furthermore on interparticle spacing effect on the interfacial region, T_g of thin films was measured while changing the film thickness. The result showed that the interfacial region formed around the nanoparticle can be as large as 250 nm, and depends on the interaction between polymer and nanoparticle. This quantitative analysis of the interfacial region may explain the deviation of T_g can be observed at a relatively low volume fraction of filler.

Confinement effect on thermal properties has been observed on thermal conductivity of PS [31], [32]. Measurement on PS thin film showed a decrease in thermal conductivity at film thickness below 300 nm [31], which is in the same order of film thickness as a result reported in PMMA thin film. A significant thermal conductivity decrease is observed at film thickness that is comparable with the radius of gyration, suggesting the morphology-dependent thermal conductivity of PS. Further analysis by numerical simulation of molecular dynamics (MD) is in agreement with experimental study, showed the decrease of thermal conductivity as the amorphous PS film thickness decreases and comparable with the radius of gyration of PS [32]. The dependence of thermal conductivity on film thickness was attributed to strong chain confinement and less entangled chain as film thickness decreased, which leads to lower thermal conductivity. In the amorphous polymers, such as PS in general, the internal stress induces the confinement effect, which leads to less chain entanglement and heat conducting path. As a result, the thermal conductivity of amorphous polymer decreases due to the confinement effect, supporting the fact that the thermal conductivity of the polymer is highly dependent on its morphology. In this work, amorphous PS is employed as the matrix, resulting in a high possibility of the interfacial region established around SiNPs; therefore, it is essential to consider the properties of interfacial region in analyzing the thermal transport in the nanocomposite.

In the nanocomposite structure, the volume fraction of the interfacial region is determined by nanoparticle's size and may dominate the fraction of matrix, as shown in Figure 4-7. At a relatively low volume fraction of 4 vol% with the interfacial region thickness of 100 nm, a nanocomposite of large size SiNPs (60 nm) has only a minor fraction of interfacial region with the majority of the matrix are remain unaffected bulk PS. However, if the SiNPs' size decreases to one-tenth, the fraction of interfacial region may significantly increase as there are ten times of surface density (Φ). Figure 4-7b shows nanocomposite with SiNPs size of 6 nm has the matrix dominantly filled with the interfacial region, indicating a strong influence of filler size in determining the properties of the matrix.

Furthermore, particle size has also a direct effect on filler dispersion condition in the nanocomposite structure. With a smaller size of the particle, there will be a significant increase in particle number, resulting in the decreasing of interparticle distance. Based on the law of ideal gas, assuming a random distribution of particles, the mean interparticle distance or nearest neighbor distribution (r) is inversely proportional to the particle density (n), as the following equation.

$$r \propto \left(\frac{1}{n}\right)^{1/3} \qquad (4\text{-}5)$$

Where $n = N/V$, representing the number of particles (N) in a unit volume (V).

At the same volume fraction in the nanocomposite, the ratio of the number of particles is proportional to particle size (D) as shown in the following equation.

$$\frac{N_6}{N_{60}} = \left(\frac{D_{60}}{D_6}\right)^3 \tag{4-6}$$

Therefore, the change of interparticle distance due to the change of the particle size can be estimated as the following equation, showing that interparticle distance of the nanocomposite with 6 nm SiNPs is one-tenth shorter than that of 60 nm SiNPs.

$$\frac{r_6}{r_{60}} \propto \frac{D_6}{D_{60}} = \frac{1}{10} \tag{4-7}$$

The decrease of interparticle distance has a direct effect on the volume fraction of the interfacial region. If the interparticle distance decrease, there will be less fraction of matrix with bulk-properties, while the interfacial region is dominating the fraction in the matrix. As a result, the properties of the matrix are dominantly determined by the properties of the interfacial region, as shown in Figure 4-7. Further decrease in the interparticle distance would induce a change in the thermal transport property of the interfacial region. When there is no more unaffected region of the polymer matrix, the decrease of filler's particle size would cause the increase of confinement effect, which is caused by the increase of internal stress in the interfacial region, as illustrated in Figure 4-7 by the darker color of the interfacial region. Both experimental and numerical analysis showed that as the film thickness decreases, the degree of confinement increases, resulting in the decrease of thermal conductivity [30]–[32].

Based on the above analysis on the properties change of interfacial region, it can be summarized that the thermal conductivity of the matrix (κ_m) in nanocomposite would be lower than the thermal conductivity of bulk-PS due to the effect of the interfacial region. The modified value of κ_m is applied in the equation (4-4) to consider the interfacial region effect in determining the thermal conductivity of nanocomposite. The result of modified κ_m for both large and small SiNPs is presented in Figure 4-8, together with a comparison with the experimental measurement results. It is shown that $\kappa_m = 0.14$ W/mK for SiNPs size of 60 nm and $\kappa_m = 0.12$ W/mK for SiNPs size of 6 nm give a good agreement of the EMA model with the measurement values. Compared with the thermal conductivity of bulk-PS, the thermal conductivity of the matrix with 60 nm SiNPs ($\kappa_{m,60}$) and 6 nm SiNPs ($\kappa_{m,6}$) are 93% and 80% of bulk-PS's thermal conductivity, respectively. The thermal conductivity of the interfacial region varies depending on the fraction of interfacial region and the degree of confinement in the interfacial region. Due to the more fraction of interfacial region and the possibility of a higher degree of confinement, it is understandable that $\kappa_{m,6}$ has a lower value than $\kappa_{m,60}$ as also expressed in Figure 4-8.

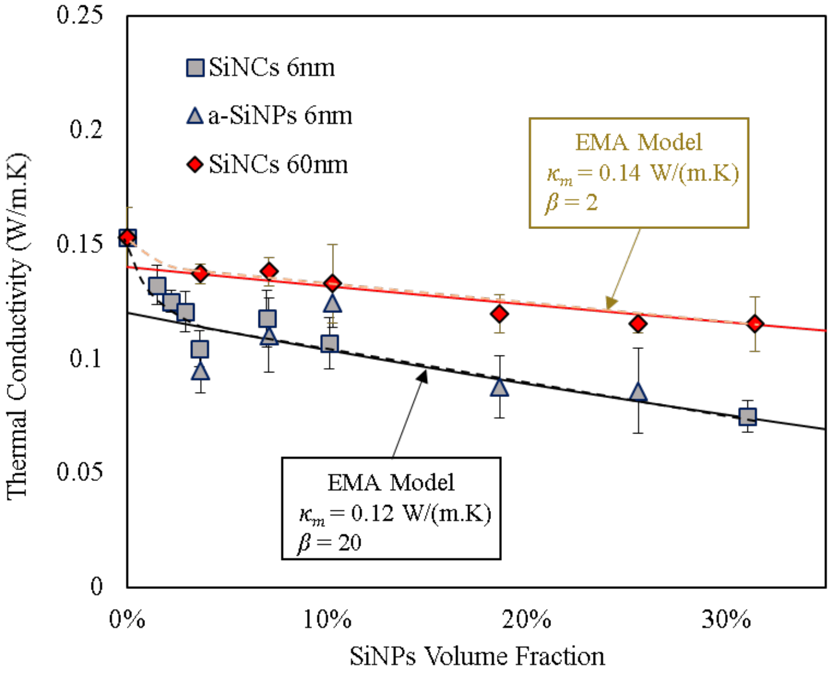

Figure 4-8 Thermal conductivity measurement results of nanocomposite samples compared with the modified-EMA model with modified thermal conductivity of the matrix (κ_m) due to the effect of the interfacial region.

Furthermore, Figure 4-8 shows that the measurement results of nanocomposite thermal conductivity can be divided into two: nonlinear region below 5 vol% and the linear region above 5 vol% that well match with the thermal conductivity models. Below 5 vol%, the number of SiNPs is relatively low, and the interfacial region is not fully developed due to large interparticle distance. At higher volume fraction of SiNPs above 5 vol%, the interfacial region has fully developed, and the further increase of SiNPs fraction will increase the phonon scattering at the material interface as represented in EMA model of equation (4-4). The interfacial region of PS is fully developed at a relatively low fraction of 5 vol%, which indicates a significant thickness of interfacial region and in agreement with other reports on PS confinement effect [31], [32].

Effective medium approximation (EMA) models have been widely employed to represent the thermal transport of nanocomposite materials. The EMA model assumes that heat is transported in the same way in matrix and filler as in the corresponding bulk materials, without any consideration on the kind of excitation, which significantly simplifies the calculation process. However, there is a problem of EMA for application in nanocomposite with relatively small particles, which require the consideration of phonon scattering by the material interface. Modified EMA model has successfully integrated interface effect at interfaces, by modifying the mean free path due to nanostructured materials [12].

However, conventional theory of EMA and modified EMA described above are only applicable in hard-materials, where the thermal properties of the material remain constant unless at the interface with other material. In soft material, which is highly dependent on morphology, material interface induces a change in morphology of surrounding molecules (interfacial region), resulting in the change of thermal transport property. At nano-scale particles, a significant fraction of interfacial region established, which is required to be considered in the thermal conductivity model based on EMA theory.

On the other hand, the quantitative analysis on the degree of confinement in the interfacial region remains as the next challenging topic to be exploited. The degree of confinement is determined by multiple factors, such as filler's size, interfacial interaction at filler/matrix interface, and interparticle distance, which are simultaneously related to each other. Further study on polymer-based nanocomposite with the consideration of the interfacial region may provide controllable thermal transport properties for wide application.

4.5. Conclusion

SiNCs are often utilized in bulk-size nanostructured materials, including for thermal properties investigation such as polymer-based nanocomposite material. A number of studies have been reported on the significance of thermal transport suppression in nanocomposite due to phonon scattering at material interfaces. The material interface effect has been considered in the thermal conductivity models of effective medium approximation (EMA), showing a decreasing trend of thermal conductivity as the representation of interfacial scattering effect.

In this work, further thermal transport of SiNPs/PS nanocomposites was analyzed by employing SiNPs with significantly different diameter of 6nm and 60nm. The measurement result shows that the nanocomposite with larger particles has uniformly higher thermal conductivity than smaller ones, mainly due to the decrease of the material interface area. The experimental results are also compared with the EMA models to investigate the effect of material interface on the interfacial region of PS that is highly morphology dependent. The result shows the EMA model can successfully represent the effect of material interfaces, yet the deviation remains for both 6 and 60 nm SiNPs. The EMA model is enhanced by modifying the thermal conductivity of matrix due to the confinement effect at the interfacial region, resulting in the well-matched thermal conductivity curves with the measurement result. The thermal conductivity of the interfacial region varies depending on the fraction of interfacial region and the degree of confinement in the interfacial region.

Fabrication process and measurement methods are performed at low temperature, allowing the preservation of unique size-dependent properties (the quantum size effect) and low-cost fabrication. The study on polymer-based nanocomposite with the consideration on interfacial region presents that interaction at the material interface and the effect doubtless play an important role in determining the thermal transport, and it would provide controllable thermal transport properties for wide application of devices.

.

4.6. References

[1] Z. Wang, J. E. Alaniz, W. Jang, J. E. Garay, and C. Dames, "Thermal conductivity of nanocrystalline silicon: Importance of grain size and frequency-dependent mean free paths," *Nano Lett.*, vol. 11, no. 6, pp. 2206–2213, Jun. 2011.

[2] J. de Boor, D. S. Kim, X. Ao, D. Hagen, A. Cojocaru, H. Föll, and V. Schmidt, "Temperature and structure size dependence of the thermal conductivity of porous silicon," *EPL (Europhysics Lett.*, vol. 96, no. 1, p. 16001, Oct. 2011.

[3] D. G. Cahill, P. V. Braun, G. Chen, D. R. Clarke, S. Fan, K. E. Goodson, P. Keblinski, W. P. King, G. D. Mahan, A. Majumdar, H. J. Maris, S. R. Phillpot, E. Pop, and L. Shi, "Nanoscale thermal transport. II. 2003–2012," *Appl. Phys. Rev.*, vol. 1, no. 1, p. 011305, Mar. 2014.

[4] H. B. G. Casimir, "Note on the conduction of heat in crystals," *Physica*, vol. 5, no. 6, pp. 495–500, Jun. 1938.

[5] Y. Ding, S. Zhou, F. B. Juangsa, M. Sugaya, X. Zhang, Y. Zhao, and T. Nozaki, "Double-parallel-junction hybrid solar cells based on silicon nanocrystals," *Org. Electron.*, vol. 30, pp. 99–104, Mar. 2016.

[6] Y. Ding, S. Zhou, F. B. Juangsa, M. Sugaya, Y. Asano, X. Zhang, Y. Zhao, and T. Nozaki, "Optical, electrical, and photovoltaic properties of silicon nanoparticles with different crystallinities," *Appl. Phys. Lett.*, vol. 107, no. 23, p. 233108, Dec. 2015.

[7] A. Miura, S. Zhou, T. Nozaki, and J. Shiomi, “Crystalline-Amorphous Silicon Nanocomposites with Reduced Thermal Conductivity for Bulk Thermoelectrics,” *ACS Appl. Mater. Interfaces*, vol. 7, no. 24, pp. 13484–13489, Jun. 2015.

[8] S. Hida, T. Hori, T. Shiga, J. Elliott, and J. Shiomi, “Thermal resistance and phonon scattering at the interface between carbon nanotube and amorphous polyethylene,” *Int. J. Heat Mass Transf.*, vol. 67, pp. 1024–1029, Dec. 2013.

[9] H. Zou, S. Wu, and J. Shen, “Polymer/Silica Nanocomposites: Preparation, Characterization, Properties, and Applications,” *Chem. Rev.*, vol. 108, no. 9, pp. 3893–3957, Sep. 2008.

[10] F. B. Juangsa, Y. Muroya, M. Ryu, J. Morikawa, and T. Nozaki, “Comparative study of thermal conductivity in crystalline and amorphous nanocomposite,” *Appl. Phys. Lett.*, vol. 110, no. 25, p. 253105, Jun. 2017.

[11] C.-W. Nan, R. Birringer, D. R. Clarke, and H. Gleiter, “Effective thermal conductivity of particulate composites with interfacial thermal resistance,” *J. Appl. Phys.*, vol. 81, no. 10, p. 6692, 1997.

[12] A. Minnich and G. Chen, “Modified effective medium formulation for the thermal conductivity of nanocomposites,” *Appl. Phys. Lett.*, vol. 91, no. 7, pp. 4–7, 2007.

[13] J. Liu and R. Yang, “Tuning the thermal conductivity of polymers with mechanical strains,” *Phys. Rev. B*, vol. 81, no. 17, p. 174122, May 2010.

[14] J. Liu and R. Yang, “Length-dependent thermal conductivity of single extended polymer chains,” *Phys. Rev. B*, vol. 86, no. 10, p. 104307, Sep. 2012.

[15] T. Zhang, X. Wu, and T. Luo, “Polymer Nanofibers with Outstanding Thermal Conductivity and Thermal Stability: Fundamental Linkage between Molecular Characteristics and Macroscopic Thermal Properties,” *J. Phys. Chem. C*, vol. 118, no. 36, pp. 21148–21159, Sep. 2014.

[16] A. Hamidi-Sakr, L. Biniek, J.-L. Bantignies, D. Maurin, L. Herrmann, N. Leclerc, P. Lévêque, V. Vijayakumar, N. Zimmermann, and M. Brinkmann, “A Versatile Method to Fabricate Highly In-Plane Aligned Conducting Polymer Films with Anisotropic Charge Transport and Thermoelectric Properties: The Key Role of Alkyl Side Chain Layers on the Doping Mechanism,” *Adv. Funct. Mater.*, vol. 27, no. 25, p. 1700173, Jul. 2017.

[17] T. Andritsch, R. Kochetov, P. H. F. Morshuis, and J. J. Smit, “Proposal of the polymer chain alignment model,” in *2011 Annual Report Conference on Electrical Insulation and Dielectric Phenomena*, 2011, pp. 624–627.

[18] C. L. Choy, Y. W. Wong, G. W. Yang, and T. Kanamoto, “Elastic modulus and thermal conductivity of ultradrawn polyethylene,” *J. Polym. Sci. Part B Polym. Phys.*, vol. 37, no. 23, pp. 3359–3367, Dec. 1999.

[19] S. Shen, A. Henry, J. Tong, R. Zheng, and G. Chen, “Polyethylene nanofibres with very high thermal conductivities,” *Nat. Nanotechnol.*, vol. 5, no. 4, pp. 251–255, Apr. 2010.

[20] L. Mangolini, “Synthesis, properties, and applications of silicon nanocrystals,” *J. Vac. Sci. Technol. B Microelectron. Nanom. Struct.*, vol. 31, no. 2, p. 020801, 2013.

[21] U. Kortshagen, “Nonthermal Plasma Synthesis of Nanocrystals: Fundamentals, Applications, and Future Research Needs,” *Plasma Chem. Plasma Process.*, vol. 36, no. 1, pp. 73–84, Jan. 2016.

[22] D. Gracin, K. Juraic, and I. Bogdanovic-Radovic, “Estimation of amorphous silicon thin film density by optical methods,” *Vacuum*, vol. 80, no. 1, pp. 146–150, 2005.

[23] S. Holding, “Polymers: A Property Database,” *Chromatographia*, vol. 72, no. 5–6, pp. 587–587, Sep. 2010.

[24] Y. Ding, R. Yamada, R. Gresback, S. Zhou, X. Pi, and T. Nozaki, “A parametric study of non-thermal plasma synthesis of silicon nanoparticles from a chlorinated precursor,” *J. Phys. D. Appl. Phys.*, vol. 47, no. 48, p. 485202, 2014.

[25] O. Yasar-Inceoglu, T. Lopez, E. Farshihagro, and L. Mangolini, “Silicon nanocrystal production through non-thermal plasma synthesis: a comparative study between silicon tetrachloride and silane precursors.,” *Nanotechnology*, vol. 23, no. 25, p. 255604, Jun. 2012.

[26] I. Doğan and M. C. M. van de Sanden, “Direct characterization of nanocrystal size distribution using Raman spectroscopy,” *J. Appl. Phys.*, vol. 114, no. 13, p. 134310, 2013.

[27] I. Doğan, N. J. Kramer, R. H. J. Westermann, K. Dohnalová, A. H. M. Smets, M. A. Verheijen, T. Gregorkiewicz, and M. C. M. Van De Sanden, “Ultrahigh throughput plasma processing of free standing silicon nanocrystals with lognormal size distribution,” *J. Appl. Phys.*, vol. 113, no. 13, p. 134306, 2013.

[28] K. H. Khoo, A. T. Zayak, H. Kwak, and J. R. Chelikowsky, “First-Principles Study of Confinement Effects on the Raman Spectra of Si Nanocrystals,” *Phys. Rev. Lett.*, vol. 105, no. 11, p. 115504, Sep. 2010.

[29] Y. Li, Y. Huang, T. Krentz, B. Natarajan, T. Neely, and L. S. Schadler, “Polymer Nanocomposite Interfaces: The Hidden Lever for Optimizing Performance in Spherical Nanofilled Polymers,” in *Interface/Interphase in Polymer Nanocomposites*, 2016, pp. 1–69.

[30] P. Rittigstein, R. D. Priestley, L. J. Broadbelt, and J. M. Torkelson, “Model polymer nanocomposites provide an understanding of confinement effects in real nanocomposites,” *Nat. Mater.*, vol. 6, no. 4, pp. 278–282, Apr. 2007.

[31] J. Liu, S. Ju, Y. Ding, and R. Yang, “Size effect on the thermal conductivity of ultrathin polystyrene films,” *Appl. Phys. Lett.*, vol. 104, no. 15, p. 153110, Apr. 2014.

[32] H. Ma and Z. Tian, “Effects of polymer chain confinement on thermal conductivity of ultrathin amorphous polystyrene films,” *Appl. Phys. Lett.*, vol. 107, no. 7, p. 073111, Aug. 2015.

Chapter 5: Conclusions and Outlook for Future Work

5.1. Conclusions

This thesis concentrates on the thermal transport property of SiNCs/polystyrene nanocomposite materials. Thin film nanocomposite of SiNCs/polystyrene is carefully fabricated to preserve the novel properties of nanomaterial, and measured for thermal conductivity that represents the thermal transport property of nanocomposite. Understanding the fundamental factors that determine the thermal transport in SiNCs/polymer is highlighted. The study in this thesis analyzes the effect of the thermal transport mechanism in the filler (SiNCs), the matrix (polystyrene), and the material interfaces, on the effective thermal conductivity of nanocomposite structure. The change of molecular structure, as well as the particle size of filler, and interfacial interaction, have been extensively investigated. The current work provides fundamental information for future applications of nanocomposite structure, especially for polymer-based nanocomposite device.

In chapter 2, the fabrication process and thermal transport properties measurement methods of the nanocomposite are explained. It is demonstrated that the low-temperature fabrication process and measurement method can successfully preserve the particle size of SiNCs as well as the surface termination without notable oxidation. Thermal properties measurements were validated by measurement of bulk polystyrene as a well-known polymer. Despite the more conductive property of SiNCs than that of polystyrene, thermal conductivity measurement result shows a decreasing trend as the SiNCs' fraction increases. The interfacial interaction at the material boundary is observed from material characterization, which leads to the significant effect of phonon scattering at the material interface, while phonon confinement effect inside SiNCs remains as the potential determining factor of transport in the nanocomposite.

In chapter 3, a further investigation of nanocomposite thermal transport is demonstrated by comparing crystalline and amorphous SiNPs as the filler. The result indicates the negligible effect of thermal transport mechanism inside the filler, which leads to the significant effect of thermal transport mechanism at the material interface. The experimental results are compared with thermal conductivity models for nanocomposite to computationally determine the contribution of thermal boundary resistance at the material interface. It is both experimentally and computationally shown that phonon confinement effect inside the filler may be neglected, and phonon scattering at SiNPs/polystyrene boundary plays a significant role in determining thermal transport of nanocomposite structure at room temperature. Additionally, the thermal transport mechanism at the material interface was further investigated by thermal annealing treatment, which shows thermal transport enhancement due to molecular interaction at material boundaries.

In chapter 4, the interfacial interaction is highlighted, and the effect on the polystyrene matrix is observed. Further analysis of thermal transport of SiNCs/PS nanocomposites was performed by employing SiNCs with significantly different diameter of 6nm and 60nm. The measurement result shows that the nanocomposite with larger particles has uniformly higher thermal conductivity than smaller ones, mainly due to the decrease of the material interface area. The experimental results are also compared with the thermal conductivity model to investigate the effect of material interface on the interfacial region of polystyrene, which has a highly morphology dependent property. The result shows that the thermal conductivity model can successfully consider the effect of material interfaces, yet the deviation remains from the experimental result. The thermal conductivity model is improved by modifying the thermal conductivity of matrix due to the confinement effect at the interfacial region, resulting in the well-matched thermal conductivity curves with the measurement result. The thermal conductivity of the interfacial region varies depending on the fraction of interfacial region and the degree of confinement in the interfacial region.

5.2. Outlook for Future Work

Polymer-based nanocomposite has been explored in various fields, as the presence of nanoparticle in the polymer matrix not only significantly improves most of the desired properties of the polymer, but also it may generate a new novel property depending on the nanoparticle used. Clearly, the observation of intrinsic properties of polymer nanocomposite, including the thermal transport mechanism, has been one of the most intriguing research. This thesis demonstrated that the substantial interfacial interaction at boundaries between filler and matrix, which induces the interfacial region confinement and interfacial phonon scattering, together with nano size of particle filler fundamentally differentiate the polymer nanocomposite from the conventional polymer and filled polymer. Further quantitative analysis on the confinement effect of the interfacial region will provide a better understanding of the molecular interaction at the material interface that is directly related to the thermal transport properties of the resultant polymer nanocomposite. A series of surface chemical modification integrated with an extensive of spectroscopy characterization such as FTIR[1], NMR[2] and Raman[1] will provide quantitative data of surface chemistry and interaction of polymer matrix with nanoparticle filler.

In addition, the main objective of polymer nanocomposite fabrication is to create maximum interfacial interaction between filler and matrix, which can be achieved by a uniformly dispersed filler throughout the polymer matrix. As the filler dispersion is determined by surface chemistry interaction between filler and matrix, the appropriate functional groups both in filler and matrix interfaces are required to produce a stable and uniform dispersion. On the other hand, the properties of the interfacial region are also affected by interfacial surface chemistry interaction. Another way to produce uniform dispersion of filler in the polymer matrix is by the preparation method of polymer nanocomposite. Among various technique of nanocomposite preparation, a controlled morphology of filler dispersion has been reported by utilizing in situ polymerization method [3], [4]. If the filler dispersion can be maintained by polymerization technique, independent control of the interfacial region by modifying the surface chemistry will provide a versatile polymer nanocomposite for a wide range of device application. Surface chemistry modification of SiNCs has been well studied for many application [5], [6], so the inclusion of SiNCs in polymer nanocomposite through polymerization method will combine the well-known novel property of SiNCs and versatility of polymer material.

Nanostructure material of SiNCs and polymer is also used in the hybrid solar cell [7]. The significant effect of interfacial region property, particularly in thermal transport properties, opens the possibility of a similar effect on optical and electronic properties of polymer utilized in the hybrid solar cell. Further investigation of optical and electronic properties of the interfacial region may provide valuable information on exciton dissociation mechanism at the material interface, which is critical in determining the performance of the hybrid solar cell.

Furthermore, the analysis of the electrical properties of the interfacial region will also provide information on electron transport at the material interface that may differ from thermal transport studied in this thesis. Integration of thermal and electron transport in polymer nanocomposite can also be utilized in the thermoelectric device, which requires low thermal conductivity yet high electronic conductivity to achieve high-performance device.

5.3. References

[1] N. Karak, “Fundamentals of Nanomaterials and Polymer Nanocomposites,” in *Nanomaterials and Polymer Nanocomposites*, Elsevier, 2019, pp. 1–45.

[2] G. Kickelbick, “Introduction to Hybrid Materials,” in *Hybrid Materials*, Weinheim, Germany: Wiley-VCH Verlag GmbH & Co. KGaA, pp. 1–48.

[3] J. Faucheu, C. Gauthier, L. Chazeau, J.-Y. Cavaillé, V. Mellon, F. Pardal, and E. B. Lami, “Properties of polymer/clay interphase in nanoparticles synthesized through in-situ polymerization processes,” *Polymer (Guildf).*, vol. 51, no. 20, pp. 4462–4471, Sep. 2010.

[4] J. Yang, T. Hasell, W. Wang, J. Li, P. D. Brown, M. Poliakoff, E. Lester, and S. M. Howdle, “Preparation of hybrid polymer nanocomposite microparticles by a nanoparticle stabilised dispersion polymerisation,” *J. Mater. Chem.*, vol. 18, no. 9, p. 998, 2008.

[5] A. Angı, “Surface Chemistry of Silicon Nanocrystals : Influence on Properties and Applications,” Technical University of Munich (TUM), 2018.

[6] J. G. C. Veinot, “Synthesis, surface functionalization, and properties of freestanding silicon nanocrystals,” 2006.

[7] Y. Ding, M. Sugaya, Q. Liu, S. Zhou, and T. Nozaki, “Oxygen passivation of silicon nanocrystals : In fl uences on trap states , electron mobility , and hybrid solar cell performance,” *Nano Energy*, vol. 10, pp. 322–328, 2014.